DISSERTATION

MADDEN-JULIAN OSCILLATION TELECONNECTIONS AND THEIR INFLUENCE ON NORTHERN HEMISPHERE WINTER BLOCKING

Submitted by

Stephanie A. Henderson

Department of Atmospheric Science

In partial fulfillment of the requirements

For the Degree of Doctor of Philosophy

Colorado State University

Fort Collins, Colorado

Spring 2017

Doctoral Committee:

Advisor: Eric D. Maloney

Elizabeth A. Barnes
David W. J. Thompson
Edwin K. P. Chong

ABSTRACT

MADDEN-JULIAN OSCILLATION TELECONNECTIONS AND THEIR INFLUENCE ON NORTHERN HEMISPHERE WINTER BLOCKING

Winter blocking events are characterized by persistent and quasi-stationary patterns that re-direct precipitation and air masses, leading to long-lasting extreme winter weather. Studies have shown that the teleconnection patterns forced by the primary mode of tropical intraseasonal variability, the Madden-Julian Oscillation (MJO), influence extratropical factors associated with blocking, such as the North Atlantic Oscillation. However, the influence of the MJO on winter blocking is not well understood. Understanding this relationship may improve the mid-range forecasting of winter blocking and the associated weather extremes.

The impact of the MJO on Northern Hemisphere winter blocking is examined using a two-dimensional blocking index. Results suggest that all MJO phases demonstrate significant changes in west and central Pacific high-latitude blocking. East Pacific and Atlantic blocking are significantly suppressed following phase 3 of the MJO, characterized by anomalous convection in the tropical East Indian Ocean and suppressed convection in the west Pacific. A significant increase in east Pacific and Atlantic blocking follows the opposite-signed MJO heating during MJO phase 7. Over Europe, blocking is suppressed following MJO phase 4 and significantly increased after MJO phase 6. Results suggest that the European blocking increase may be due to two precursors: 1) a pre-existing anomalous Atlantic anticyclone, and 2) a negative Pacific North American (PNA) pattern triggered by the MJO.

The influence of the MJO on winter blocking may be different if a change occurs to the basic state and/or MJO heating, such as during El Niño – Southern Oscillation (ENSO) events. MJO teleconnections during ENSO events are examined using composite analysis and a nonlinear baroclinic model and their influence of winter high-latitude blocking is discussed. Results demonstrate that the ENSO-altered MJO teleconnection patterns significantly influence Pacific and Atlantic blocking and the impacts depend on ENSO phase. During El Niño, Pacific and Atlantic blocking is significantly increased following MJO phase 7, with maximum Atlantic blocking frequency anomalies reaching triple the climatological winter mean blocking frequency. Results suggest that the MJO forces the initial anomalous Atlantic dipole associated with the blocking increase, and transient eddy activity aids in its persistence. During La Niña, significant changes to high-latitude blocking are mostly observed during the first half of an MJO event, with significant suppression of Pacific and Atlantic blocking following MJO phase 3.

MJO teleconnection patterns may also be altered by basic state and MJO heating biases in General Circulation Models (GCMs), important for mid-range forecasting and future climate studies of weather and climate patterns significantly altered by the MJO, such as winter blocking. Data from phase 5 of the Coupled Model Intercomparison Project (CMIP5) is used to investigate MJO teleconnection biases due to basic state and MJO biases, and a linear baroclinic model is used to interpret the results. Results indicate that poor basic state GCMs (but with a good MJO) can have equally poor skill in simulating the MJO teleconnection patterns as GCMs with a poor MJO. Large biases in MJO teleconnection patterns occur in GCMs with a zonally extended Pacific subtropical jet relative to reanalysis. In good MJO GCMs, bias in the location and horizontal structure of Indo-Pacific MJO heating is found to have modest impacts on MJO teleconnection patterns. However, East Pacific heating during MJO events can influence MJO teleconnection amplitude and the pathways over North America. Results suggest that both the MJO and the basic state must be well represented in order to properly capture the MJO teleconnection patterns.

ACKNOWLEDGEMENTS

I am extremely grateful to my advisor, Dr. Eric Maloney, for his invaluable mentoring, patience, knowledge, and support throughout my graduate school years. I am grateful to Dr. Elizabeth Barnes, Dr. David Thompson, and Dr. Edwin Chong for serving in my committee and providing invaluable feedback. I also would like to extend my gratitude to Dr. Seok-Woo Son at Seoul National University for his guidance and hospitality during and after the East Asia and Pacific Summer Institutes (EAPSI) fellowship program. I am thankful for the many conversations with CSU faculty and students whose perspectives have greatly improved my understanding of this field. I am deeply thankful for the unwavering support, understanding, and patience of my family and friends. I am especially grateful to my husband, Dave, for always believing in me. I could not have asked for a better support system. Most of all, I am thankful to God, without whom none of this would be possible.

This work was supported by the Climate and Large-Scale Dynamics Program of the National Science Foundation under grants AGS-1441916 and AGS-1025584, and by the NOAA MAPP Program under grants NA15OAR4310098, NA15OAR4310099, and NA16OAR4310064. Support was also provided by the Science and Technology Center for Multi-Scale Modeling of Atmospheric Processes, managed by CSU under Cooperative Agreement ATM-0425247. This work was also funded in part by the NSF EAPSI fellowship grant 1515489.

TABLE OF CONTENTS

CHAPTER 1: INTRODUCTION

1.1 Purpose

Boreal winter atmospheric blocking is associated with enduring extreme weather conditions due its persistent and quasi-stationary nature (e.g. Berggren et al. 1949; Hoskins and Sardeshmukh 1987; Buehler et al. 2011; Masato et al. 2012). Previous studies have shown that the primary mode of tropical intraseasonal variability, the Madden-Julian Oscillation (MJO), influences important factors associated with blocking, including the North Atlantic Oscillation (NAO; e.g. Cassou 2008; Lin et al. 2009) and Rossby wave breaking (e.g. Moore et al. 2010). These extratropical impacts are due to the large-scale Rossby waves, or teleconnection patterns, forced by MJO heating (e.g. Kiladis and Weickmann 1992; Higgins and Mo 1997; Matthews et al. 2004). Although extensive work has been done on MJO global impacts (e.g. Zhang 2005), the extent and the underlying mechanisms to which the MJO impacts winter blocking are not well understood. Understanding this relationship may lead to improvements in the mid-range forecasting of winter blocking and in turn, the long-lasting extreme weather conditions associated with blocking.

Predictability associated with MJO extratropical impacts implies predictability of the MJO Rossby wave pathways. The characteristics of stationary Rossby waves forced by the MJO are largely dictated by the background flow, or basic state, and the characteristics of the heat source (e.g. Hoskins and Karoly 1981; Sardeshmukh and Hoskins 1988; Hoskins and Ambrizzi 1993; Jin and Hoskins 1995). Changes to the basic state and evolution of MJO heating can occur due to longer-timescale variability, such as the El Niño – Southern Oscillation (ENSO; e.g.

Rasmusson and Wallace 1983). During ENSO events, MJO Rossby wave pathways are altered (e.g. Takahashi and Shirooka 2014; Roundy et al. 2010; Moon et al. 2011), suggesting that any impact the MJO has on the frequency of blocking may also be modified. Basic state and MJO heating biases are also found in General Circulation Models (GCMs) that may affect the quality of MJO teleconnections (e.g. Ahn et al. 2017; Kim et al. 2011). GCM bias may lead to bias in the MJO Rossby wave teleconnections, with possible implications for the medium range prediction of weather and climate patterns significantly altered by the MJO. Furthermore, GCMs are the primary tools used in future climate studies. Bias in the MJO teleconnections may lead to uncertainties in future weather and climate patterns influenced by the MJO.

The purpose of this study is to better understand the impact of MJO teleconnections on Northern Hemisphere winter blocking. Furthermore, this study investigates the effect of model biases on MJO teleconnections, as well as impact of ENSO-induced basic state and MJO heating changes on MJO teleconnections. This is useful for the mid-range forecasting of atmospheric blocking as well as the many weather and climate extratropical impacts of the MJO. It is also useful for future climate studies, which often employ GCMs. Provided here is a brief literature review. Further background can be found in the individual chapters.

1.2 Atmospheric blocking

The extratropical Northern Hemisphere consists of mean westerly winds with a variable eddy-driven jet. During a typical blocking event, the eddy-driven jet becomes "blocked" and transient eddies along the Pacific or Atlantic storm track are redirected. Blocks can persist for a number of weeks and are quasi-stationary, so that the deflection of the storm track can result in extreme precipitation events such as droughts and flooding. In the Pacific basin, blocks are often characterized as omega (Ω) blocks due to the Ω-symbol shape of the blocking geopotential height anomalies, where an anticyclone is joined by two smaller cyclonic anomalies on its southeastern and southwestern flanks. In the Atlantic and European regions, blocks often consist of an anomalous dipole, characterized by an anticyclonic anomaly north of an anomalous cyclone. Blocking anticyclones are associated with the persistent southward advection of cold polar air along its eastern flank, leading to long-lasting cold snaps in the winter such as the European blocking event discussed in Hoskins and Sardeshmukh (1987).

A blocking anticyclone can develop north of the eddy-driven jet, referred to as a high-latitude block. High-latitude blocks divert rather than "block" the jet (e.g. Woollings et al. 2008). In the Atlantic basin, high-latitude blocking (i.e. Greenland blocking) is associated with a southward shift of the eddy-driven jet, with characteristics similar to the negative phase of the NAO. The NAO and Greenland blocking are strongly linked (e.g. Shabbar et al. 2001), so much so that Woollings et al. (2008) suggested that the negative NAO pattern is a result of frequent Greenland blocking, and the positive NAO occurs when Greenland blocking is infrequent. Woollings et al. (2008) made a similar argument regarding the West-Pacific pattern (e.g. Wallace and Gutzler 1981) and west Pacific high-latitude blocking.

Although the NAO – Greenland blocking relationship continues to be a chicken and egg problem, with various theories on causality (e.g. Benedict et al. 2004; Franzke et al. 2004; Woollings et al. 2008), the strong link suggests an impact of the MJO on Greenland blocking given the significant influence of the MJO on the NAO pattern (e.g. Lin et al. 2009; Cassou 2008). In addition, previous studies have suggested the MJO may impact Pacific blocking by altering the frequency of Rossby wave breaking (Moore et al. 2010), as well as indirectly impacting European blocking (Cassou 2008). Furthermore, while investigating the forecasting of the MJO and blocking separately, Hamill and Kiladis (2014) noticed that certain phases of the MJO were associated with changes in the frequency of instantaneous Northern Hemisphere winter blocking based on the one-dimensional blocking index of Tibaldi and Molteni (1990), where an instantaneous block is a reversal of the meridional gradient of 500-hPa geopotential height with no persistence or quasi-stationarity criteria. The study did not discuss possible reasons for the relationship, but did suggest a link between the MJO and Northern Hemisphere winter blocking that largely motivated the research presented here. Examining the influence of the MJO on winter blocking requires understanding how a tropical system like the MJO can influence the extratropics. This will be discussed next.

1.3 The Madden-Julian Oscillation (MJO)

The MJO is a large-scale convective system in the tropics coupled to large-scale circulation anomalies that propagates eastward from the Indian Ocean to the Central Pacific (e.g. Madden and Julian 1971; 1972). MJO enhanced convection is flanked by anomalously suppressed convection, propagating at a speed of approximately 5 m/s in the Eastern Hemisphere. Near the Dateline, the MJO circulation decouples from convection and propagates faster across the Western Hemisphere with characteristics of a dry Kelvin wave. Wind signatures circumnavigate the tropics at upper-levels. The MJO is characterized by zonal wavenumbers 1 – 3 and is recognized as the primary mode of intraseasonal variability in the tropics (e.g. Salby and Hendon 1994; Zhang 2005).

MJO convective anomalies act as heat sources modifying the tropical atmosphere. The response of the tropical atmosphere to a heat source was investigated by Gill (1980). Using the shallow water equations, the study found that an Equatorial heat source is associated with a zonally asymmetric response, with low-level westerlies to the west of the heating flanked by low-level cyclones on either side of the Equator, and a Kelvin wave to the east of the heating with low-level easterly winds. The heat source is characterized by low-level convergence, ascent, and upper-level divergence (e.g. Hoskins and Karoly 1981), and is coupled to a large-scale circulation similar to the Walker Circulation. Moisture transport by the large-scale circulation also influences subsequent convective heating. In addition, large-scale tropical heating like the MJO impacts the atmosphere beyond the tropics by forcing stationary large-scale Rossby waves (e.g. Hoskins and Karoly 1981; Matthews et al. 2004; Seo and Son 2012). Stationary Rossby waves propagate into the extratropics connecting remote regions and are therefore referred to as teleconnection patterns. Teleconnection patterns significantly alter the flow and their understanding is essential in mid- to long-range forecasting (e.g. Wallace and Gutzler 1981; Mo and Higgins 1998; Hendon et al. 2000; Jones et al. 2004).

1.4 MJO Teleconnections

MJO teleconnections are known to significantly impact weather and climate patterns, including global monsoons (Lorenz and Hartmann 2006; Lau and Waliser 2012), regional temperatures and precipitation (Vecchi and Bond 2004, Jones et al. 2004; Donald et al. 2006), hurricanes (e.g. Maloney and Hartmann 2000; Slade and Maloney 2013), the Pacific North – American pattern (PNA; e.g. Mori and Watanabe 2008; Riddle et al. 2013), and the North Atlantic Oscillation (NAO; e.g. Cassou 2008; Lin et al. 2009). Forecasting these global impacts, as well as the MJO influence on extratropical blocking, requires an understanding of the pathways of MJO Rossby waves, which are largely dictated by the background flow and the characteristics of MJO heating (e.g. Hoskins and Karoly 1981; Hoskins and Ambrizzi 1993; Ting and Sardeshmukh 1993; Jin and Hoskins 1995; Matthews et al. 2004; Yasui and Watanabe 2010).

1.4.1 MJO Rossby waves

Anomalous upper-level divergence associated with tropical large-scale heating in the Indian and Pacific Ocean basins leads to absolute vorticity anomalies within the subtropical jet. These vorticity anomalies occur due to vortex stretching by the divergent flow and absolute vorticity advection and are a source for Rossby waves (Sardeshmukh and Hoskins 1988). Rossby waves of zonal wavenumbers characteristic of the MJO will propagate eastward within the jet, and can propagate away from the jet once they reach the jet exit region, with lower wavenumbers able to propagate into higher latitudes (e.g. Hoskins and Karoly 1981). MJO Rossby waves are approximately wavenumber 2 – 4 (e.g. Seo et al. 2016) and are associated with teleconnections reaching the North Pacific and extending over North America and the Atlantic (e.g. Lin et al. 2009; Cassou 2008). The pathways of MJO Rossby waves change as MJO heating propagates eastward and modifies the Rossby wave source (RWS; e.g. Seo and Son 2012; Tyrrell et al. 1996; Sardeshmukh and Hoskins 1988) and the extent of the subtropical jet (e.g. Moore et al. 2010). As a result, studies of MJO extratropical impacts often divide the MJO lifecycle into eight phases, where each phase represents a different longitudinal location of MJO heating (e.g. Cassou 2008; Lin et al. 2009; Wheeler and Hendon 2004). The teleconnections associated with each MJO phase may change, however, if the characteristics of MJO heating are altered or if there are changes to the basic state, such as during ENSO events (e.g. Matthews et al. 2004; Hendon et al. 1999; Kessler 2001). Both of these changes would alter the RWS. For example, during cold ENSO events the subtropical jet is strengthened, and a strengthened jet is associated with a higher amplitude RWS (Sardeshmukh and Hoskins 1988). Furthermore, changes to the location and amplitude of MJO heating may alter the location and strength of the RWS.

The pathway of Rossby waves is largely determined by the upper-level zonal wind and can be estimated by calculating the stationary zonal wavenumber (K_s; e.g. Karoly 1981; Hoskins and Ambrizzi 1993). In general, the highest K_s exist within the subtropical jet and the tropical westerlies, and the lowest wavenumbers at higher latitudes. Hoskins and Ambrizzi (1993) provide useful schematics of the linear behavior of Rossby waves that we will briefly summarize here:

a) Rossby waves of zonal wavenumber k tend to be refracted towards regions where $K_s > k$.

b) Rays are reflected where $K_s = k$ and the meridional wavenumber, l, is zero.

c) Rays must turn prior to regions where the meridional gradient of absolute vorticity, and hence K_s, is zero. This is often observed on the northern flank of the subtropical jet.

d) Rossby waves do not propagate into regions where the mean zonal wind is easterly. At the critical latitude where the zonal wind reaches zero, $K_S \rightarrow \infty$.

e) Rays become trapped where K_s is maximized, such as in strong westerly jets. Jets therefore act as Rossby waveguides.

The general behavior of Rossby waves as mentioned above suggests that changes to the basic state can alter the pathway of Rossby waves. For example, during warm ENSO conditions the Pacific subtropical jet is extended eastward and during cold ENSO conditions the jet is retracted relative to the mean (e.g. Matthews et al. 2004). Rossby waves forced within the Pacific subtropical jet, such as MJO Rossby waves, may propagate further eastward within the subtropical jet during warm ENSO events than during cold ENSO events before they can propagate north. This is based on points c) and e) listed above. As such, the MJO Pacific teleconnection patterns during warm ENSO events may be shifted eastward relative to those during cold ENSO events. Differences in the MJO teleconnection patterns during ENSO events also indicates that the influence of the MJO on blocking may depend on ENSO phase. Biases in models may also reflect an extended or retracted jet relative to that observed, producing resulting biases in teleconnections.

1.4.2 General Circulation Models (GCMs)

The previous discussion suggests that in order to accurately predict the extratropical influence of MJO teleconnections, models must properly simulate MJO heating as well as the basic state. GCMs are the primary tools used in future climate assessments, such as those conducted by the Intergovernmental Panel on Climate Change (IPCC). However, many state-of-the-art GCMs contain large biases in its simulation of the MJO and/or the model basic state (e.g. Ahn et al. 2017; Jiang et al. 2015; Kim et al. 2014; Hung et al. 2013; Kim et al. 2011). GCMs with such biases may not be able to properly simulate the MJO teleconnections and, in turn, extratropical MJO impacts such as blocking. This may lead to uncertainties in future projections of the weather and climate patterns that are altered by MJO teleconnections.

1.5 Study Outline

The impact of MJO teleconnections on Northern Hemisphere winter blocking is investigated in Chapter 2. The chapter utilizes a two-dimensional (2D) blocking index to calculate the frequency of blocking events relative to MJO phase in the Pacific, Atlantic, and European basins. Possible mechanisms for the observed relationships will also be discussed.

Chapter 2 is a published manuscript in the *Journal of Climate*, referred to as Henderson et al. (2016). Chapter 3 investigates changes to the MJO teleconnections during ENSO phases due to changes in the basic state and MJO heating. Utilizing the same methodology as Chapter 2, Chapter 3 examines the MJO impacts on Pacific and Atlantic high-latitude blocking during ENSO events. The results from Chapter 3 may aid in the mid-range forecasting of blocking during ENSO events, which demonstrate many differences to the results of Chapter 2. Given the dependence of MJO teleconnections on the basic state and MJO heating, Chapter 4 documents the ability of MJO teleconnections to be properly represented in GCMs, which often have biases in both MJO simulation skill and basic state. Utilizing data from GCMs in phase 5 of the Coupled Model Intercomparison Project (CMIP5), MJO teleconnection biases are discussed in association with errors in the basic state and MJO heating. Understanding MJO teleconnection errors may provide insight into biases associated with extratropical weather and climate that is significantly altered by the MJO. Chapter 4 is in press in the *Journal of Climate*, and is referred to in this dissertation as Henderson et al. (2017).

CHAPTER 2: THE INFLUENCE OF THE MADDEN-JULIAN OSCILLATION ON NORTHERN HEMISPHERE WINTER BLOCKING

2.1 Introduction

Blocking anticyclones have been studied for many decades due to their ability to significantly disrupt the mean westerly flow in the mid-latitudes (Berggren et al. 1949; Masato et al. 2012). The upper tropospheric jet in the mid-latitudes can become “blocked” for several weeks in the presence of a blocking anticyclone. During boreal winter, these persistent anticyclones redirect polar air towards the mid-latitudes, leading to extreme cold weather outbreaks (e.g. Hoskins and Sardeshmukh 1987; Buehler et al. 2011). During boreal summer, blocking anticyclones can result in heat spells and episodes of drought (e.g. Dole et al. 2011).

Given the influence of atmospheric blocks on extreme events, understanding what regulates blocking is crucial to improving the prediction and understanding of these extremes. Many studies have demonstrated that anomalous heating in the tropics can generate stationary Rossby waves (e.g., Hoskins and Karoly 1981; Hoskins and Ambrizzi 1993; Jin and Hoskins 1995; Trenberth et al. 1998) that influence blocking. One example is the heating associated with the El Niño – Southern Oscillation (ENSO); using a general circulation model, Hinton et al. (2009) demonstrated that a stationary Rossby wave response to ENSO forcing leads to a dipole pattern in geopotential height anomalies over the northeast Pacific resulting in favorable conditions for blocking during the warm phase and unfavorable conditions during the cold phase. In the Southern Hemisphere, Australian blocking and rainfall was found to be influenced by

ENSO heating and by intraseasonal convection anomalies near Indonesia (Pook et al. 2013; Marshall et al. 2014).

On intraseasonal timescales, tropical heating variability associated with the Madden-Julian Oscillation (MJO) has been demonstrated to significantly perturb the mid-latitude flow, with consequences for blocking including changes in Pacific wave breaking (Moore et al. 2010) and the North Atlantic Oscillation (NAO; Cassou 2008; Lin et al. 2009). The MJO is the dominant form of intraseasonal variability in the tropics with a period of approximately 30 – 90 days (Madden and Julian 1971, 1972). During an MJO event, coupled circulation and convection anomalies propagate eastward across the equatorial Indian and west Pacific Oceans, with flow anomalies becoming decoupled to convection at the Dateline. Anticyclonic Rossby gyres form west of the enhanced convection while cyclonic gyres develop behind areas of suppressed convection (Salby and Hendon 1994; Zhang 2005). Numerous studies have demonstrated that MJO-induced Rossby waves significantly alter the global extratropical circulation in both hemispheres (e.g., Kiladis and Weickmann 1992; Higgins and Mo 1997; Matthews et al. 2004). However, the impact of these MJO teleconnections on Northern Hemisphere blocking has received much less attention.

Some previous studies have presented links between the MJO and Northern Hemisphere blocking. In the Pacific, Moore et al. (2010) demonstrated that the subtropical jet maximum has a tendency to shift in conjunction with the eastward propagating MJO Rossby gyres, leading to variability of the location and amplitude of the jet that in-turn influences wave breaking. These changes in wave breaking coincide with changes in blocking. However, the blocking definition employed in that study allows for the propagation of anticyclones, which may produce different results if the analysis is focused on quasi-stationary blocks. Hoskins and Sardeshmukh (1987) investigated the long-lasting blocking event that was associated with the European sudden winter cold snap of 1985. The authors noticed a coincident strong intraseasonal oscillation over the equatorial Indian and Pacific Oceans and hypothesized that the phenomenon could have altered the Euro-Atlantic circulation leading to the European blocking event. In more recent work, Cassou (2008) found a significant relationship between the positive phase of the NAO, European blocking, and the MJO. This study hypothesized that the MJO acts as a trigger for the positive NAO which then transitions to a European blocking pattern, although it is still unclear whether the role of MJO heating in European blocking goes beyond triggering the NAO pattern. Additionally, Hamill and Kiladis (2014) found that certain phases of the MJO (i.e. the longitudinal location of MJO heating) coincide with active blocking periods in the Northern Hemisphere, and other phases coincide with suppressed periods. The mechanisms that bring about these relationships were not discussed, however. Furthermore, Hamill and Kiladis (2014) used a one-dimensional (1D) instantaneous blocking index (i.e. no blocking persistence criteria was used) and diagnosed blocking at the same latitude band for all longitudes, which may be a particularly poor assumption for regions such as the North Pacific (e.g. Pelly and Hoskins 2003).

In this study we utilize a two-dimensional (2D) blocking index to provide statistical relationships between the MJO and large-scale blocking events over the Pacific, Atlantic, and European regions. We will also discuss possible physical mechanisms for the relationships observed. Additionally, we propose a new mechanism for the link between the MJO and European blocking, which suggests that the importance of the MJO goes beyond the NAO mechanism hypothesized by Cassou (2008). Section 2.2 describes the development of the blocking index used as well as the compositing techniques. Sections 2.3 – 2.6 describe the MJO phase composite blocking frequencies and discusses possible physical mechanisms for the relationships observed for the West-Central Pacific, East Pacific, Atlantic, and European regions, respectively. Lastly, Section 2.7 summarizes the main findings and discusses future work.

2.2 Methodology

2.2.1 Data

Boreal winter (December – February; DJF) six-hourly global data are obtained from the ERA-Interim Reanalysis (Dee et al. 2011) and daily averages are calculated from December 1979 to February 2010, for a total of 31 winter seasons comprised of 90 days each. We use 500-hPa geopotential height, and 200-hPa zonal and meridional winds with a 1.5° x 1.5° horizontal resolution. Streamfunction is calculated from the 200-hPa wind fields. Satellite-based daily outgoing longwave radiation (OLR) with a 1° x 1° horizontal resolution was acquired from the National Oceanic and Atmospheric Administration (NOAA) National Climatic Data Center (NCDC; Lee et al. 2011).

To generate MJO phase composites, the eastward propagation of the MJO is divided into 8 phases using the Real-Time Multivariate MJO (RMM) indices of Wheeler and Hendon (2004; http://www.bom.gov.au/climate/mjo/), where each phase gives an approximate representation of the longitudinal location of MJO convection anomalies. The two RMM indices, known as RMM1 and RMM2, are the principal components of the first two combined empirical orthogonal functions of equatorially averaged 200-hPa and 850-hPa zonal wind and OLR anomalies. An MJO phase is determined by $\tan^{-1}(\frac{RMM2}{RMM1})$, where phase 1 is associated with initial MJO convection in the West Indian Ocean, and phase 8 represents MJO enhanced convection reaching the Central Pacific. Only the days with an RMM amplitude greater than 1, defined by $\sqrt{(\mathrm{RMM1}^2+\mathrm{RMM2}^2)}$, are used to assess blocking frequency in our analysis.

2.2.2 Two-dimensional blocking index

MJO anomalies are known to shift the jet from its climatological position (e.g. Moore et al. 2010). Therefore, pre-defining an average latitude at which to observe blocking may not adequately detect blocks that develop at other latitudes. This is largely resolved by utilizing a 2D blocking index. The Northern Hemisphere blocking index used here is based on Masato et al. (2013a) which detects blocking using the average difference of 500-hPa geopotential height across a latitude, ϕ_0, given by:

$$B_i = \frac{2}{\Delta\phi}\int_{\phi_0}^{\phi_0+\frac{\Delta\phi}{2}} Z_i \partial\phi - \frac{2}{\Delta\phi}\int_{\phi_0-\frac{\Delta\phi}{2}}^{\phi_0} Z_i \partial\phi \tag{2.1}$$

A longitude is defined as instantaneously blocked when the difference between the integrated 500-hPa geopotential height (Z) above ϕ_0 is greater than the integrated height below ϕ_0 so that $B_i > 0$, where ϕ_0 is varied between 40°N and 70°N. A value of 30° latitude is used for $\Delta\phi$, consistent with Masato et al. (2013a) and Pelly and Hoskins (2003). Equation (2.1) is applied separately to four sectors: the West-Central Pacific (140°E - 160°W), East Pacific (160°W - 95°W), Atlantic (90°W – 20°W), and Europe (20°W - 45°E), using the additional criteria discussed below. Local daily positive maxima of B_i are found within each sector to represent the approximate center of each block. A similar approach to Masato et al. (2013a) is then followed to track each blocking event within each sector. The first instance of a positive B_i maximum is considered the first day of a blocking event. The B_i maximum of the next day must be within 13.5° latitude and 18° longitude of the previous day's maximum. If more than one maximum is detected, the maximum with the smallest great circle distance to the previous day's maximum is used. All B_i maxima must be within the longitudinal bounds of each region as defined above, but the block, defined as the region of positive B_i values around each maximum, may extend beyond these bounds. A large-scale block is then defined if at least 15° of longitude are consecutively blocked. Only the times meeting these criterion for at least 5 days are retained.

The mean DJF blocking frequency for the Pacific, Atlantic, and European regions is shown in Figure 2.1. For brevity, the West-Central Pacific and East Pacific sectors are combined in this and all subsequent figures. Although the mean West-Central Pacific high-latitude blocking overwhelms the mean East Pacific blocking in Figure 2.1, results with the separate Pacific sectors were found to provide the same information as results combining the two sectors.

The Pacific is comprised of 2023 total blocked days (419 of these over the East Pacific sector), the Atlantic 922 blocked days, and Europe 973 blocked days (Figure 2.1). These blocking frequency climatologies are consistent with those of Masato et al. (2013a,b). Figure 2.1 demonstrates that at high latitudes over the North Pacific a geopotential height reversal is found approximately 45% of the time during DJF, a similar total as that obtained by Woollings et al. (2008). This can be partially explained by the blocking criterion, which is more easily met in the high latitudes where the meridional gradient of geopotential height is relatively weak (Masato et al. 2013b). Woollings et al. (2008) found this high-latitude blocking to be dynamically significant, although unlike classical mid-latitude blocking, high-latitude blocking does not block the jet but rather diverts its flow.

2.2.3 Composite analysis

Blocking events are composited relative to MJO phase for four different lags, where an *n* day lag represents blocking occurrence *n* days after a given MJO phase. The full record of each blocking event is analyzed, so it is possible that a continuation of the same blocking event exists across multiple lags and/or MJO phases. For each MJO phase blocking frequencies are calculated by taking the total number of blocked days during (or after, if lagged) a given MJO phase and dividing it by the total number of days within that MJO phase. This study examines blocking in DJF; hence composites that examine blocking after an MJO phase will also utilize the MJO index of late November. Blocking composites are shown in Figures 2.2, 2.7, and 2.8 for the Pacific, Atlantic, and European regions, respectively, and will be discussed in detail in the subsequent sections.

In order to assess statistical significance, a moving-blocks bootstrap is employed independently at each lag and MJO phase. The technique is similar to a traditional bootstrap in that both sample from the original dataset with replacement in order to approximate the characteristics and distribution of the data in the bootstrap samples (e.g. Marchand et al. 2006; Wilks 2011). However, unlike a traditional bootstrap, which samples individual elements from the dataset, the moving-blocks bootstrap samples blocks of consecutive elements in order to preserve the data autocorrelation in the bootstrap samples. The moving-blocks bootstrap is implemented by taking the full blocking record and dividing it into overlapping blocks of size l beginning on each day. A bootstrap sample of size N is generated by joining N/l randomly sampled blocks, where here N represents the total number of days in each MJO phase across all 31 seasons. This process is repeated 5000 times in order to obtain sufficient bootstrap samples.

In order to implement the moving-blocks bootstrap, block length l must be chosen. A block length that is too large may result in a bootstrap sample that is not sufficiently random, and a block length that is too small may not properly capture the data's persistence. Block length should also increase with increasing N (e.g. Wilks 2011). To calculate block length, the number of days in each phase is calculated for all MJO events, where days in the same phase within one MJO event may not be consecutive. The block length is then the average number of days per phase rounded to the nearest integer. This is a similar procedure as that of Marchand et al. (2006), who randomly chose a point in time and looked for the adjacent elements following the same regime to determine block length. The block lengths calculated in this way are $l = 4, 5, 6, 4, 5, 4, 6, 5$ for MJO phases 1 – 8, respectively. A block length that is too small can result in an unwarranted rejection of the null hypothesis (Marchand et al. 2006). Therefore, the largest calculated block length of $l = 6$ was tested for all MJO phases and similar results were obtained, suggesting that the results are robust to small variations in this parameter. Values of N are provided in the blocking composites above each phase panel (Figures 2.2, 2.7, and 2.8) as well as a value N_B denoting the total number of days within or after (if lagged) each MJO phase found to contain a block. A ratio $R = N_B/N$ is also provided, representing the percentage of MJO phase days at a given lag that experienced blocking within the region.

2.2.4 Wave vector analysis

Possible explanations for the relationships found in the blocking composites are supported by analyzing the composite atmospheric patterns associated with MJO events. Whereas blocking composites are calculated and shown in days, upper level anomalous streamfunction and 500-hPa geopotential height anomalies associated with MJO phases are shown as pentad means (i.e. five day averages) in Figures 2.3 – 2.6. Pentad 0 indicates the field average of days 0 – 4 following an MJO phase, pentad 1 corresponds to days 5 – 9, and so forth. Assuming a normal distribution, geopotential height anomalies found to be significantly different from zero are dotted based on a two-tailed Student's *t*-test with $N/5$ independent samples, where 5 is approximately the average number of days per phase in an MJO event (e.g. Alaka and Maloney, 2012).

In order to examine the Rossby wave pathway for each MJO phase, we calculate a horizontal wave activity flux, or **W** vectors, derived from the conservation of wave-activity psudomomentum by Takaya and Nakamura (2001) defined as:

$$\mathbf{W} = \frac{1}{2|\boldsymbol{U}|}\begin{bmatrix} U(\psi_x^2 - \psi\psi_{xx}) + V(\psi_x\psi_y - \psi\psi_{xy}) \\ U(\psi_x\psi_y - \psi\psi_{xy}) + V\left(\psi_y^2 - \psi\psi_{yy}\right) \end{bmatrix} \tag{2.2}$$

where ψ is the 200-hPa lagged perturbation pentad streamfunction, U and V are the mean DJF 200-hPa zonal and meridional winds, respectively, and the subscripts indicate partial derivatives of ψ in the corresponding x and/or y directions. **W** is approximately parallel to the group velocity of a stationary Rossby wave, thereby giving a snapshot of the direction in which wave packets travel at a given moment in time. **W** vector divergence indicates a Rossby wave is emitted (a wave source) and **W** vector convergence implies Rossby wave absorption (a wave sink).

2.3 West-Central Pacific (140°E - 160°W)

Blocking in the Central and West Pacific is predominant at high latitudes (Figure 2.1), where a geopotential height reversal corresponds to diverted rather than blocked flow (e.g. Woollings et al. 2008). Mid-latitude blocking is far less common, with a mean blocking frequency of 2-3% between 40°N - 45°N. The anomalous blocking frequency for each MJO phase at lag 0 is shown in Figure 2.2, where dotted regions indicate a blocking frequency that is outside of the 95% confidence bounds of the moving blocks-bootstrap distribution. Figure 2.2 suggests that significant changes in West-Central Pacific blocking frequency are observed during all MJO phases, with a blocking frequency increase during phases 6 – 8 and a decreased frequency during phases 1 – 5.

Phase 1 of the MJO corresponds to suppressed tropical convection over the Maritime Continent and is associated with the initialization of MJO convection in the West Indian Ocean. The enhanced convection propagates east and reaches the Maritime continent in phase 5. The propagating convection and associated Rossby gyres appear as an eastward propagation of the subtropical jet (e.g. Moore et al. 2010). During phase 1, positive MJO-induced geopotential height anomalies are observed between 30°N – 55°N over the western North Pacific with anomalously negative geopotential height to the north over eastern Russia (Figure 2.3, top row), indicative of a strengthened climatological gradient. The dipole pattern persists, moving east with the MJO Rossby gyres through phase 5, as demonstrated in Figure 2.3.

The eastward movement of the MJO-induced dipole and associated strengthened climatological gradient coincides with reduced blocking frequency (Figure 2.2) for MJO phases 1 – 5. Blocking frequency decreases of 19.2% occur in Northeast Russia in phase 1, where the frequency change is defined (here and henceforth) as the maximum difference in blocking frequency from the DJF mean in the region discussed. Phases 3 – 4 demonstrate significant decreases in blocking frequency over the central Pacific, with the greatest reduction in high-latitude blocking days occurring during phase 4, producing anomalies of almost -20%. During phase 5, the strengthened geopotential height gradient coincides with reduced blocking (-17%; Figure 2.2) in Southern Alaska and the Central Pacific.

During MJO phase 5, suppressed convection exists in the West Indian Ocean and propagates eastward behind the enhanced convection that exists to the east, with the enhanced convection reaching the Dateline in phase 8. Anomalous negative geopotential height begins to develop between 30°N – 50°N in the West Pacific during phase 5 (Figure 2.3) and strengthens as it moves east in phase 6. By phases 7 – 8, the negative geopotential height anomaly expands over much of the North Pacific with anomalously high geopotential height to the northeast, and phase 8 anomalies form a positive PNA-like pattern. These MJO-induced anomalies imply a weakened climatological gradient north of the anomalous cyclonic center.

Enhanced blocking frequency is observed where the climatological gradient is weakened (Figure 2.2; phases 6 – 8). During phase 6, a significant increase in blocking frequency occurs in the West Pacific between 45°N – 50°N, where the mean blocking frequency is relatively low (Figure 2.1). Moore et al. (2010) demonstrated that phase 6 coincides with an increase in cyclonic wave breaking. Cyclonic wave breaking in the West Pacific leads to blocking north of the jet, resulting in a northward flux of warm and moist subtropical air and thereby increased precipitation over the western North Pacific, with anomalously cold and dry conditions over China, Korea, and Japan (Masato et al. 2013b). During phase 8, the highest increase in high-latitude blocking is observed, with an anomalous blocking frequency peak near +17%. Phase 8 shows blocking anomalies of about -9% from 45°N – 50°N, coinciding with a strengthened geopotential height gradient (Figure 2.3).

One issue is determining cause and effect. It is possible that the geopotential height anomalies presented in Figure 2.3 are the result of the blocking anomalies rather than the cause.

Such a scenario was previously discussed in Woollings et al. (2008) in the context of Atlantic blocking. We attempt to address this issue by resampling (with replacement) the phase 8 dates to match the climatological ratio of blocking to no blocking dates for the North-Central Pacific (34% blocking days, 66% no blocking days) and averaging to create new geopotential height anomaly composites as in Figure 2.3. Re-sampling the phase 8 blocking and no blocking dates to match the North-Central Pacific climatology will remove any excess North-Central Pacific blocks that make up the anomalous blocking increase shown in Figure 2.2. If the phase 8 increase in blocking is responsible for the Pacific geopotential height anomalies in Figure 2.3, the new geopotential height anomaly composite with the climatological ratio would not be able to reproduce the Figure 2.3 anomalies over the North-Central Pacific. This assumes that North-Central Pacific blocks that form during phase 8 have the same structure as blocks that occur at all other times. However, the new phase 8 geopotential height composite is almost identical in structure and amplitude to that of Figure 2.3, and so it is not show here. This analysis suggests that the increased blocking over the North-Central Pacific during phase 8 is not responsible for the geopotential height anomalies in Figure 2.3. The same analysis was repeated for MJO phase 4, which has the greatest decrease in North-Central Pacific blocking, and again the new geopotential height anomalies are almost identical in structure and amplitude to that of Figure 2.3, so it is not shown here. We repeated this analysis for both MJO phases but with the maximum climatological ratio of the entire North Pacific (44% blocking days, 56% no blocking days) and the same results were obtained. Our contention is also supported by previous studies using simple models that do not resolve blocking which demonstrate similar eastward propagating geopotential height anomalies as a response to MJO forcing (e.g. Bao and Hartmann 2014; Seo and Son 2012; Matthews et al. 2004). However, we do note that the blocking frequency anomalies in Figure 2.2 may still amplify the geopotential height anomalies relative to the mean.

In contrast to our results, Moore et al. (2010) found increased mid-latitude Central Pacific blocking when MJO convection is active over and east of the Maritime continent, or approximately RMM phases 2 – 5. Their study utilizes the blocking index of Croci-Maspoli et al. (2007) that allows for blocking propagation, hence the eastward propagating anticyclone discussed for phases 1 – 5 likely corresponds to their increase in mid-latitude blocking. In contrast, our blocking index allows only minimal propagation so that the propagating anticyclone shown in Figure 2.3 is not considered a block. Moore et al. (2010) did, however, find decreased blocking between 40°N - 50°N in the Central Pacific when MJO convection is active just east of the Dateline, which approximately corresponds to RMM phases 7 – 8, in agreement with our results.

Although the relationship between blocking and the MJO are not discussed in detail in Hamill and Kiladis (2014; hereby HK14), their study calculates the change in instantaneous blocking frequency relative to MJO phase (lag 0) based on the 1D index of Tibaldi and Molteni (1990), where blocking is calculated along a constant blocking latitude near 50°N. Our results agree in some aspects with HK14, who found suppressed instantaneous blocking during MJO phases 1 – 5. The unmodified Tibaldi and Molteni (1990) index used in HK14 looks for blocking as high as 54°N; based on our results it is likely their phase 1 – 5 decrease in blocking frequency coincides with instances of high-latitude blocking. In contrast to our results, HK14 demonstrates a blocking increase west of the Dateline only during phase 5, whereas we show that mid-latitude blocking increases further during phase 6. These differences may arise from the lack of a persistence requirement in their blocking index.

2.4 East Pacific (160°W - 95°W)

We now analyze the relationship between MJO phase and East Pacific blocking frequency. Figure 2.2 suggests that significant decreases in East Pacific blocking frequency are strongest and most widespread from phases 3 – 5, and enhancement of blocking is most prominent during phases 7 and 8. Persistent significant changes in blocking frequency are observed for MJO phases 3 and 7, where a significant difference from the mean is observed out to a 15 day lag (e.g. see Figure 2.12 below). We discuss MJO phases 3 and 7 and subsequent time lags here to help explain physical mechanisms for the enhancement and suppression of blocking at different points in the MJO lifecycle.

2.4.1 MJO phase 3

During phase 3 of an MJO event enhanced convection is observed in the East Indian Ocean, and suppressed convection is located in the West Pacific (Wheeler and Hendon 2004). This heating pattern is associated with a large-scale stationary Rossby wave train that propagates north over the Pacific Ocean in a great circle route to the North Pacific Ocean, North America, and to the Atlantic (Figure 2.4), in agreement with the wave path presented by Lin et al. (2009). At pentad 0, the wave activity flux associated with the MJO teleconnection is strongest over the Pacific and North America, where the teleconnection geopotential height anomalies are significantly different from zero and remain significant through pentad 1.

Phase 3 geopotential height anomalies over the East Pacific sector demonstrate a persistent north-south dipole structure suggestive of a strengthened climatological geopotential height gradient with increased westerlies between 45°N – 65°N, a pattern especially apparent by pentad 1. The strengthened climatological gradient coincides with the decrease in blocking frequency observed for all lags following phase 3 (e.g. see Figure 2.12). During phase 3, East Pacific blocking frequency is decreased by up to 4.2% (Figure 2.2). By lag 5, blocking frequency decreases by as much as 6.1% (not shown), consistent with the amplification of negative blocking anomalies shown during phase 4 (Figure 2.2), since MJO phases average about 5 days apart. MJO phases 4 and 5 geopotential height anomaly composites (Figure 2.3) also show a similar north-south dipole structure in the East Pacific associated with reduced East Pacific blocking. Using a general circulation model, Hinton et al. (2009) demonstrated that an anomalous dipole structure (similar to Figure 2.4) coincides with faster cyclone speed along the region of increased westerlies. The increase in cyclone speed reduces the tendency of the cyclones to locally advect subtropical low potential vorticity (PV) air poleward that supports blocking onset and maintenance. This mechanism aids in the suppression of blocking, in agreement with Figure 2.2.

2.4.2 MJO phase 7

Phase 7 is characterized by opposite sign heating as phase 3, with suppressed convection in the East Indian Ocean and enhanced convection in the West Pacific. Likewise, the teleconnection pattern in the Pacific associated with phase 7 (Figure 2.6) is similar to that of phase 3 but with weakened anomalies of the opposite sign. Over the East Pacific, a significant positive geopotential height anomaly is observed to the north of 45°N for all pentads shown. The anticyclone is flanked by negative anomalies to the south and west, suggesting that the climatological geopotential height gradient is weakened with anomalously weak westerly flow between the geopotential height anomalies, which is near the climatological location of the storm track (e.g. Pelly and Hoskins 2003). The weakened gradient coincides with a significant increase in blocking frequency observed for all subsequent lags of MJO phase 7 (e.g. see Figure 2.12). At lag 0, an East Pacific blocking frequency increase of +7% is observed for phase 7 (Figure 2.2). The anomalous blocking frequency is highest for lags 10 and 15, reaching +8.6% and +9.3%, respectively (not shown). With a DJF climatological blocking frequency peaking near 7%, Figure 2.2 suggests that blocking frequency is approximately doubled during and following phase 7. Out of the 419 total East Pacific blocking days of the 31 winter seasons, approximately 15.3% (lag 0) to 17.2% (lag 15) occur during and following MJO phase 7.

In addition to a weakened geopotential height gradient, Hinton et al. (2009) demonstrated that a dipole pattern such as that observed in the East Pacific during phase 7 coincides with reduced cyclone speed along the weaker westerlies near the climatological location of the storm track, thereby increasing the tendency for weather systems to deposit low PV air from the subtropics into higher latitudes. The poleward flux of low PV air from storms in the East Pacific would aid in the formation and persistence of blocks during and following phase 7.

Our results agree in some respects with HK14. While differences are expected due to the different methods used, our East Pacific results at lag 0 agree fairly well with HK14 for MJO phases 3 – 5. However, the increase in blocking associated with phase 7 is largely absent in their study. Their blocking frequency calculation suggests that the increase in blocking during phase 7 occurs only west of 150°W. In addition to using a constant blocking latitude, the blocking index of HK14 also imposes no persistence or large-scale requirements, which may result in a different mean blocking frequency from ours.

2.5 Atlantic (90°W - 20°W)

In the Atlantic sector, a significant blocking frequency increase occurs during and/or after MJO phases 6 – 8, while a significant decrease is shown during and/or after phases 1 – 5 (e.g see Figure 2.12 below). In order to most clearly demonstrate the MJO's dynamical influence on Atlantic blocking, we have chosen to focus on MJO phases 3 and 7, each of which captures the sign of the blocking response of the other MJO phases respectively (similar to what was done by Lin et al. 2009 for the NAO pattern). The blocking frequency anomalies for lags 5, 10, and 15 are shown in Figure 2.7 for phase 3 (top row) and phase 7 (bottom row).

2.5.1 MJO phase 3

During and following MJO phase 3 (Figure 2.4, pentads 0 and 1), significant high geopotential height anomalies exist over eastern North America with negative geopotential height to the northeast, indicating a strengthened climatological geopotential height gradient. The dipole coincides with the suppressed high-latitude blocking west of Greenland observed soon after phase 3 (Figure 2.7, first panel), which peaks in magnitude at a value of -9.4%. The Rossby wave train (Figure 2.3) strengthens over the Atlantic after 1 pentad and becomes more robust after 2 pentads, with a pattern that develops reminiscent of the positive phase of the NAO (e.g. Lin et al. 2009**)**. The NAO pattern indicates that the climatological pressure gradient is strengthened, with increased westerlies between 45°N – 55°N and a more zonal flow. The positive NAO coincides with significantly decreased blocking frequency in the mid-latitudes and the high latitudes (Figure 2.7). With a DJF climatological mean blocking frequency peaking near 17%, Figure 2.7 implies that following phase 3 the probability of blocking over the North

Atlantic is more than halved, dropping to a 5 – 7% total blocking frequency ten to fifteen days after phase 3, with some regions reaching blocking probabilities near zero.

A significant decrease in high-latitude blocking frequency occurs as early as lag 5 (Figure 2.7, first panel), which is prior to the development of the positive NAO anomalies (Figure 2.4), suggesting it may not be the NAO pattern that creates unfavorable conditions for high-latitude blocking. Previous studies have suggested that the pattern associated with a positive NAO is actually a result of infrequent high-latitude blocking (Woollings et al. 2008; Davini et al. 2012), indicating that the accumulated suppression of high-latitude blocking after phase 3 (Figure 2.7) may cause the positive NAO pattern in Figure 2.4. The NAO-blocking cause and effect relationship is difficult to diagnose and is beyond the scope of this study.

The MJO has been suggested to influence the NAO pattern by directly forcing the tropospheric Rossby wave teleconnection to the Atlantic as shown in Figure 2.4 (e.g. Lin et al. 2009; Cassou 2008), as well as by a more indirect influence through the stratosphere. Garfinkel et al. (2012) proposed that MJO-induced poleward and vertically-propagating Rossby waves modify the polar vortex, which in turn impact the NAO; a mechanism previously suggested for the ENSO-NAO link (Bell et al. 2009; Ineson and Scaife 2009). The downward coupling of the stratospheric polar vortex and the tropospheric NAO pattern is a longer pathway of MJO influence with timescales up to one month, with MJO phase 3 preceding a cooling of the polar lower stratosphere and consequently a more positive NAO by 10 to 25 days after phase 3 (Garfinkel et al. 2014). Given the longer timescale of the stratospheric pathway, it is possible that North Atlantic blocking can be influenced at time scales longer than what are discussed here.

2.5.2 MJO phase 7

The teleconnection pattern associated with phase 7 (Figure 2.6) results in opposite signed anomalies compared to phase 3, with an Atlantic pattern indicative of a negative NAO. During a negative NAO, a weakened climatological pressure gradient occurs in the Atlantic with higher amplitude wave-like flow (e.g. Shabbar et al. 2001; Woollings et al. 2008). Following phase 7, the negative NAO coincides with an increase in Atlantic blocking frequency (Figure 2.7, bottom row), reaching +16.5% at lag 15, an almost doubling of the mean blocking frequency. Of the 922 total Atlantic blocked days in the 31 winter seasons, approximately 14 – 15% occur within 5 – 15 days after MJO phase 7.

MJO phase 7 has been shown to influence the negative NAO pattern via a tropospheric pathway as shown in Figure 2.6 (e.g. Lin et al. 2009), as well as through the stratosphere. Garfinkel et al. (2014) found that the MJO-induced low pressure over the North Pacific (Figure 2.6, pentad 0) corresponds to greater meridional tropospheric and stratospheric heat flux and a weakening of the polar vortex, and consequently a more negative NAO 10 to 25 days following MJO phase 7.

As a comparison to our results, the instantaneous 1D blocking index of HK14 shows a decrease in Atlantic blocked days during MJO phases 4 – 6, whereas we find a significant decrease only during phase 5, lag 0, north of 50°N (not shown), which may also be partially reflected in the lags following phase 3 (Figure 2.7). HK14 also shows an increase in blocked days during MJO phase 8, in agreement with our results (see Figure 2.12 below).

2.6 Europe (20°W - 45°E)

The greatest reduction in European blocking is shown to occur during and/or following MJO phases 3 – 5, while a significant blocking increase exists for MJO phases 6 – 8. Here we have chosen to focus on phases 4 and 6 to represent these two groups, as these phases demonstrate the greatest and most persistent changes in blocking frequency (Figure 2.8). It is worth noting that MJO phase 8 demonstrates a similar increase in blocking frequency at lag 0 (not shown) as the phase 6 composites during lags 10 and 15 (Figure 2.8, bottom row). Phase 8 coincides with the timeframe of the phase 6 lag 10 – 15 day composites and therefore a similar physical mechanism can be argued. Phase 7 also shows a significant increase in blocking frequency at lag 0, although it is confined to west of the Prime Meridian (not shown).

2.6.1 MJO phase 4

During and following MJO phase 4 (Figure 2.3, only pentad 0 shown), the Euro-Atlantic region consists of the positive NAO pattern that is initiated following phase 3. Figure 2.3 demonstrates a significant positive geopotential height anomaly over Europe with a negative anomaly to the northwest during phase 4. The dipole straddles the climatological location of the storm track (e.g. Pelly and Hoskins 2003) and indicates a strengthened climatological gradient. The dipole is associated with a significant decrease in blocking frequency, with blocking frequency anomalies of approximately -9.5% five days after phase 4 (Figure 2.8, top row). This corresponds to a frequency reduction of more than two thirds of the climatology. The decrease continues through lag 10 east of the Prime Meridian, with an anomalous blocking frequency reaching -8.5%.

In agreement, HK14 and Cassou (2008) show reduced blocking during comparable MJO phases. HK14 found a higher amplitude decrease, peaking at 15 – 20% below the DJF mean during phases 4 – 5. The higher frequency in HK14 is expected as they included all instantaneously blocked days with no large-scale requirements. A greater decrease is found by Cassou (2008), who found up to a 30% decrease in Scandinavian blocking occurrence relative to climatology following phase 4. Cassou (2008) defined each day in their study as belonging to one of the four Atlantic regimes (one of which is Scandanavian blocking) even if the flow is weakly correlated to the assigned regime, resulting in higher blocking frequencies.

2.6.2 MJO phase 6

An increase in blocking is observed following phase 6 as early as lag 5, with a significant blocking frequency increase of 8 – 9% for lags 10 – 15 (Figure 2.8, bottom row). Approximately 8.3% (lag 5) to 11.4% (lag 15) of all 973 European blocked days follow phase 6. These results are in agreement with those of HK14 who found an increase in instantaneous blocking during MJO phase 7, which can be interpreted as corresponding to a lagged phase 6. Our results also show an increase during phase 7, although weaker than phase 6 (not shown). A significant relationship between the MJO and European blocking at such early lags following phase 6 is also presented by Cassou (2008).

While phase composites of upper-level streamfunction and geopotential height demonstrate a clear wave train during other phases (e.g. phase 3), phase 6 composites (Figure 2.5) portray a confusing evolution of anomalies leading to a strong dipole over the Euro-Atlantic region resembling a negative NAO pattern. The wave activity flux vectors do not portray a clear Rossby wave pathway, suggesting two possibilities: 1) The Euro-Atlantic anomalies develop independent of the MJO and the timing is coincidental, or 2) the MJO link in the composites is more complex than in other regions and phases.

An initial examination of the phase 6 composites (Figure 2.5) suggests the first possibility, particularly since the increase in European blocking frequency is observed as early as 5 days after phase 6 (Figure 2.8). This provides only a short time for a Rossby wave induced by phase 6 MJO heating in the west Pacific to reach the Euro-Atlantic region. Cassou (2008) proposes that the increase in blocking following phase 6 demonstrates the tendency for the North Atlantic to follow a preferred set of regimes as discussed by Vautard (1990). The argument states that the increase in blocking is an indirect consequence of the positive NAO pattern previously set up by MJO phase 3. We test this by taking all phase 3 days and calculating the European blocking frequency forward in time, with the idea that if the only role of the MJO is to force the positive NAO, the high frequency of blocking observed following phase 6 should be reproducible with phase 3 data at a large lag. We generated European blocking composites every five days for phase 3 lags 10 – 40 (not shown). However, the blocking increase of Figure 2.8 could not be reproduced. This suggests that in order for increased blocking to coincide with MJO phase 6, the MJO may play a role beyond that suggested by Cassou (2008).

The connection between MJO and European blocking is further investigated by taking the 227 days that lag phase 6 by five days and separating them into two categories: European blocking (N_B = 81 days) and no European blocking (146 days). Similar results were obtained with lag 10, and hence only lag 5 is presented. Daily composites are shown in Figures 2.9 and 2.10 for the blocking and no blocking cases, respectively, with the purpose of uncovering key differences that may suggest an MJO-European blocking link. Since blocking appears soon after phase 6, we examine the days preceding MJO phase 6, where phase 6 is indicated by lag 0.

Four days prior to phase 6 in the blocking composites (Figure 2.9; lag -4) there is a Rossby wave train propagating north over the North Pacific and east over North America. The wave activity flux vectors follow the direction of the Rossby wave packets, which appear to display energy dispersion towards the Atlantic high-latitudes as well as southeast towards the anticyclonic center over the east coast of the United States. The latter resembles a negative PNA pattern, which is clearly absent in the no blocking composites (Figure 2.10). By lag 0 (Figure 2.9; lower left panel), Rossby wave energy propagates from the large minimum over North America towards the European blocking, with **W** vectors depicting the eastward Rossby pathway over Greenland. The negative PNA pattern provides a link from the Pacific to the Euro-Atlantic region prior to phase 6 and serves as a possible explanation for the increase in European blocking that follows phase 6. Previous studies have demonstrated that the MJO can act as a trigger for the PNA pattern (e.g. Mori and Watanabe 2008; Franzke et al. 2011). Given that both the blocking and no blocking composites are associated with strong MJO events, it is worth investigating the days preceding the negative PNA pattern to examine why the pattern is absent in the no blocking composites.

Figure 2.9 demonstrates that MJO enhanced convection is initially concentrated over the Bay of Bengal (lags -24 to -20 days) and is associated with a wave train that develops within the subtropical jet (plotted in red). An anticyclonic anomaly forms poleward of the jet exit region, which acts as a source of Rossby wave energy, as indicated by the divergence of **W** vectors, for the wave train that develops across the Pacific in lag -12. The anticyclone shifts east and grows north of the jet by lag -4, becoming part of the negative PNA pattern. This sequence of events is in agreement with the PNA lifecycle suggested by Mori and Watanabe (2008), who argued that PNA growth is initiated over the subtropical jet exit region triggered by MJO-induced divergence north of the Bay of Bengal. In contrast, Figure 2.10 does not follow this lifecycle. Lags -24 to -20 demonstrate weaker OLR anomalies in the tropics relative to Figure 2.9, suggesting that on average the no blocking case is preceded by weaker early MJO phase heating. Although the composite difference in OLR between the blocking and no blocking cases was not found to be statistically significant based on a difference of means test, MJO heating strength and structure in the early phases of an MJO event may still be important for the PNA life cycle and in turn, European blocking. Furthermore, a zonal wind average for the 30 days preceding phase 6 for the blocking and no blocking cases (not shown) demonstrate that the subtropical jet in the blocking case is shifted equatorward over the Central Pacific relative to the no blocking case. This difference suggests a possible change in the basic state that may influence the pathway of the MJO-induced anomalies and necessitates further investigation.

Figures 2.9 and 2.10 also demonstrate a second key difference between blocking and no blocking cases: a pre-existing anticyclone over the Euro-Atlantic region exists at all lags preceding European blocking. In fact, the composite structure of Figure 2.9 suggests that the anticyclone shifts northeast towards Europe, eventually becoming the blocking anticyclone as shown by an asterisk in each panel. The asterisks represent the maxima in Atlantic daily streamfunction (where the maximum closest to the previous day's maximum is marked), and tracing this feature demonstrates the evolution of the anomalous anticyclone. The maxima's daily trajectory is shown in Figure 2.11 from 12 days prior to 5 days after phase 6, demonstrating the transition followed by stagnation of the anticyclone. The anticyclone strength is found to be significantly different from the no blocking composites at the 90% level based on a two-tailed difference of means test prior to and after transition, although at certain lags the anticyclone is weakened and does not pass the difference of means test. This transition may be indicative of the positive NAO to blocking transition suggested by Cassou (2008). It is possible that the negative PNA pattern and the pre-existing Euro-Atlantic anticyclone are necessary precursors for the MJO-blocking link suggested by Figure 2.9.

Once blocking is established, it is also possible that MJO anomalies could project onto the negative PNA pattern, thereby enhancing or maintaining the large minimum over North America that provides a Rossby wave energy pathway for the European blocking. It would be interesting to examine the impacts of the PNA pattern on the persistence of phase 6 European blocking. Further analysis is required to better understand these mechanism and relationships.

2.7 Summary and Conclusions

Utilizing a 2D blocking index, we examined the statistical relationship between the MJO and boreal winter blocking over the Pacific, Atlantic, and European regions. Although the MJO-blocking relationship is not discussed in detail in HK14, the results presented here expand on the blocking composite shown in their study, which utilized a 1D index along a constant blocking latitude to demonstrate instantaneous blocking relative to MJO phase. Blocking composites were generated for 8 phases of the MJO as defined by Wheeler and Hendon (2004), and statistically significant relationships were found for all regions. The blocking frequency associated with each MJO phase is summarized in Figure 2.12, where the 2D blocking frequency calculated above is averaged between 40°N – 60°N to highlight the mean mid-latitude changes in blocking frequency. The DJF climatological mean mid-latitude blocking frequency is shown in each MJO phase panel in black, and the lag 0 – 15 day average blocking frequency associated with each MJO phase is portrayed from cooler to warmer colors, respectively, with statistically significant regions marked with an asterisk. The main findings of this study are summarized below.

MJO heating is associated with significant circulation anomalies throughout the North Pacific. These anomalies were found to influence blocking in the West-Central Pacific region during all phases, particularly in the high-latitudes. Our results contrast those of Moore et al. (2010), whose study demonstrated an increase in Pacific blocking frequency coinciding with the eastward propagating anticyclone during MJO phases 2 – 5. In the East Pacific, a doubling in blocking frequency follows MJO phase 7. The teleconnection results in a dipole pattern that weakens the climatological gradient and the westerly flow near the climatological location of the storm track, where cyclones slow down as they move poleward depositing low PV air. The favorable blocking conditions can be observed in the geopotential height composites of phase 7, which demonstrate a persistent anticyclone out to a 15-day lag. Approximately 15.3% of all East Pacific blocks coincide with phase 7. A stronger, opposite-signed wave train occurs following phase 3, resulting in a strengthened climatological gradient over the East Pacific and a decrease in blocking frequency.

The teleconnection patterns associated with phases 3 and 7 are also important for Atlantic blocking. In agreement with Lin et al. (2009) and Cassou (2008), 10 to 15 days after MJO phase 3 a positive NAO pattern develops over the Atlantic. We find that Atlantic blocking frequency is more than halved in association with the positive NAO pattern. In contrast, MJO phase 7 is followed by a negative NAO pattern, which coincides with a high-amplitude wave-like flow and an increase in blocking frequency. Atlantic blocking frequency is almost doubled following phase 7, reaching +16.5% relative to climatology. Approximately 14 – 15% of all DJF Atlantic blocked days follow phase 7.

In Europe, a significant blocking increase follows phase 6, with up to 11.4% of all DJF European blocked days occurring within 15 days of MJO phase 6. We identify two possible precursors to the phase 6 blocking: 1) A pre-existing anticyclone over the Atlantic, and 2) a negative PNA pattern. The first precursor was discussed by Cassou (2008), who noted the positive NAO pattern from MJO phase 3 could provide the anticyclone that later would transition into the European block. While Cassou (2008) hypothesized the phase 6 European blocking is primarily a result of phase 3 driven NAO variability, we propose a second precursor, a negative PNA pattern, as a link between the MJO and European blocking. In agreement with the daily PNA life cycle discussed by Mori and Watanabe (2008), we argue that through forcing of the negative PNA by the MJO, European blocking coincides with phase 6. The negative PNA pattern then acts as a Rossby wave energy pathway influencing the European blocking, as indicated by the **W** vectors.

Future work should focus on further understanding the mechanisms between the MJO and blocking, in addition to the PNA pattern. More work is needed to understand how changes in MJO heating and the basic state influence the relationships observed between the MJO and blocking. This is particularly true for Europe, in which MJO heating differences and the basic state may play a role in the development of the negative PNA pattern preceding phase 6 blocking. The implications for General Circulation Model (GCM) simulations of blocking should also be examined, since GCMs tend to poorly simulate both the MJO (e.g. Zhang et al. 2006) and blocking (e.g. Masato et al. 2013a). Additionally, a two-way interaction between blocking and the MJO necessitates investigation. Blocking alters the flow impacting the extratropical waveguide, and in turn, extratropical waves may influence MJO convection and therefore future MJO Rossby wave energy dispersion (e.g. Roundy 2011).

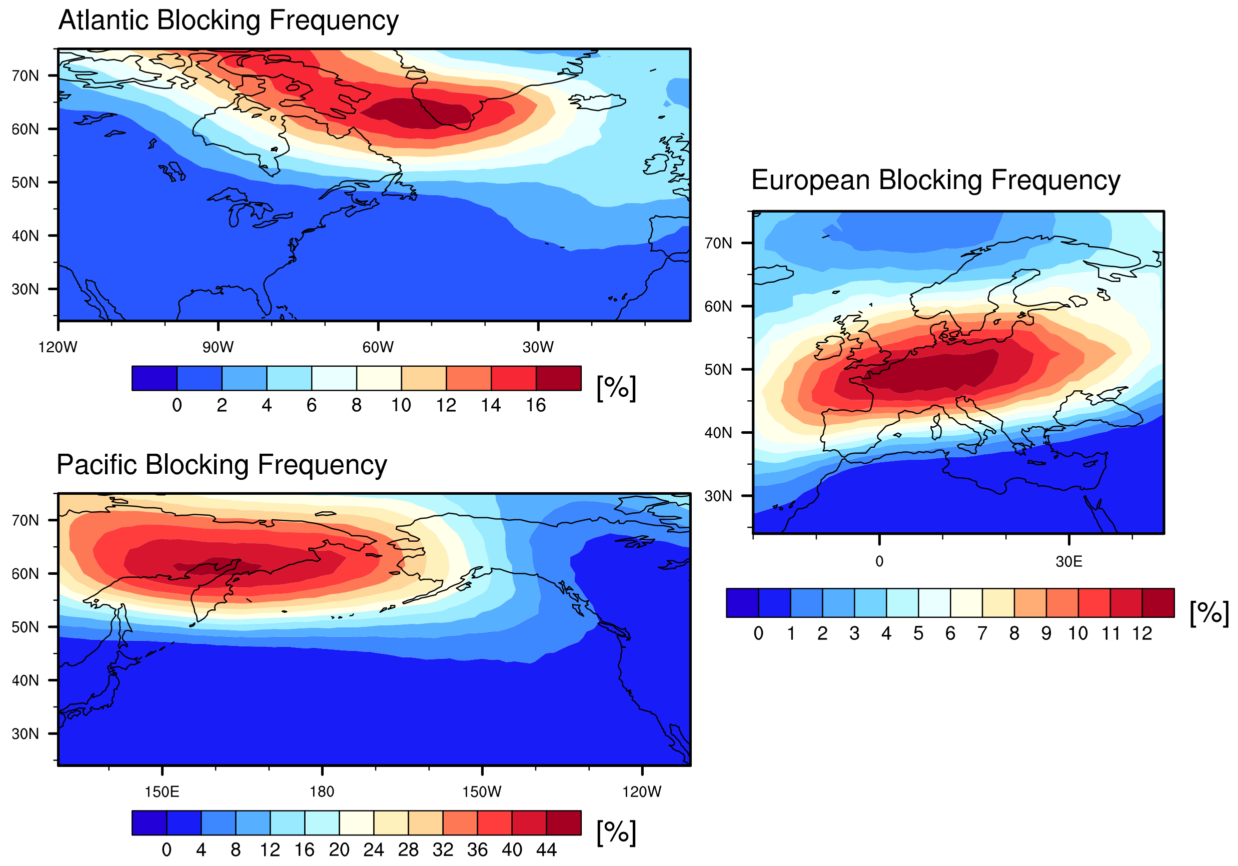

FIG. 2.1. Mean blocking frequency for the Atlantic, Pacific, and European sectors for 31 boreal winter seasons from 1979-2009. The Pacific panel includes West-Central and East Pacific blocking days.

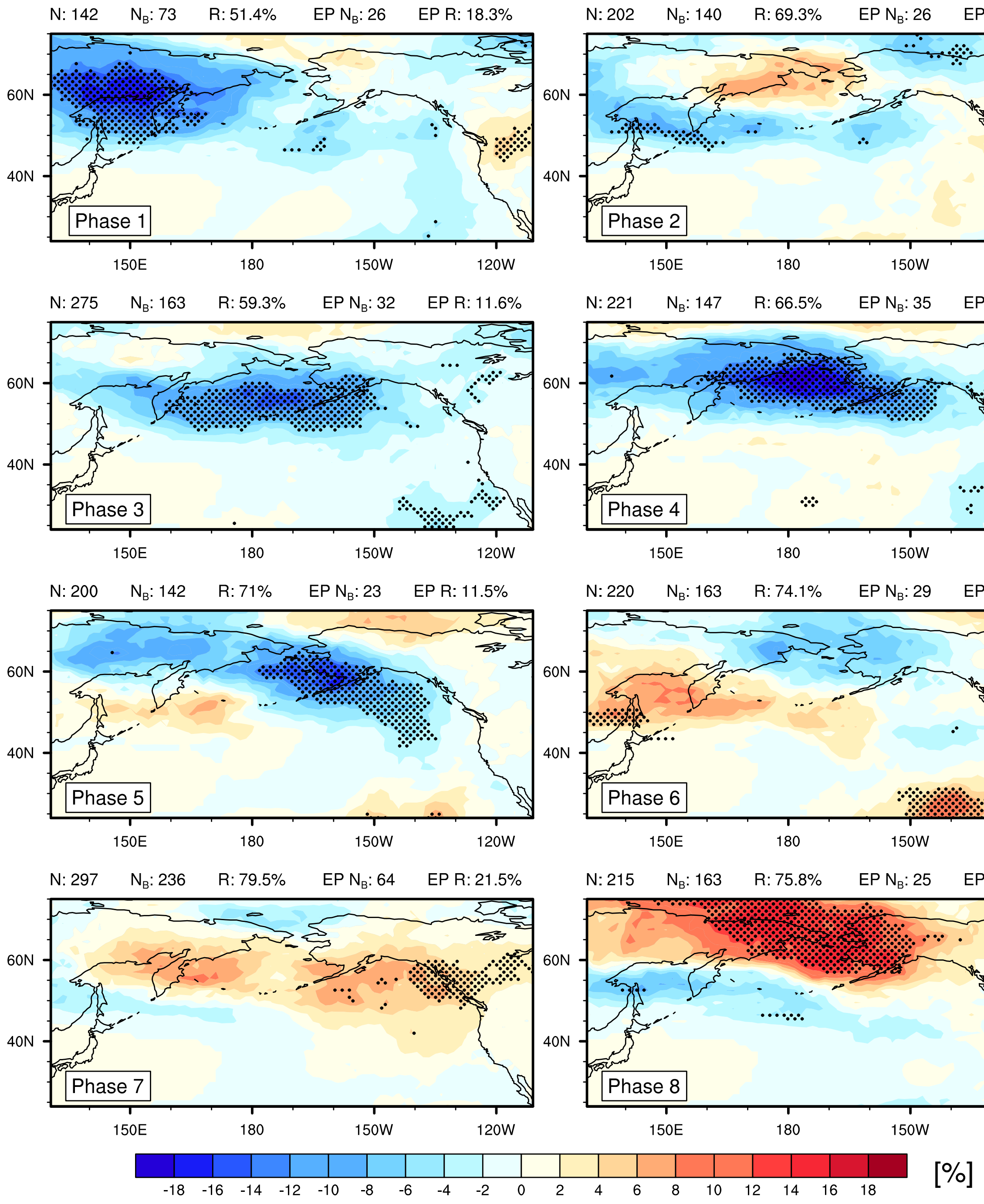

FIG. 2.2. Pacific blocking frequency anomalies at lag 0 for each phase of the MJO as determined by (2.1). Blocking frequencies are shown as a deviation from the DJF mean (Figure 2.1). Black dotting demonstrates the anomalies found to be 95% significantly different from zero. For explanation of the values above each panel, see Section 2.2.3.

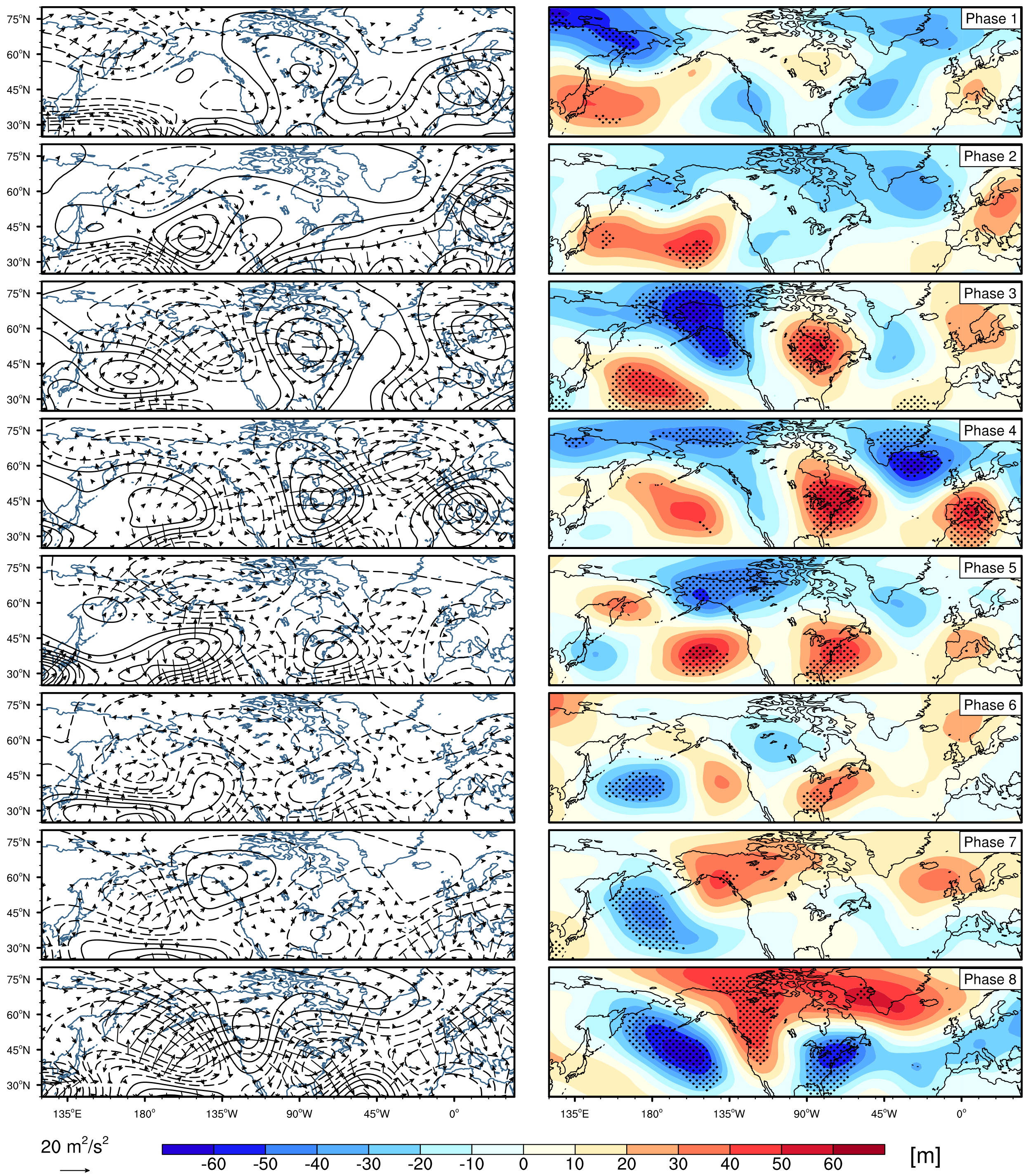

FIG. 2.3. MJO phase composites of anomalous 200-hPa streamfunction (left column) and 500-hPa geopotential height (right column) for pentad 0, where a pentad denotes a 5 day mean. Pentad 0 is the field average of days 0-4 following an MJO phase. Black dotting demonstrates the anomalies found to be 95% significantly different from zero. Overlaid in the anomalous streamfunction are the wave activity flux vectors as defined by (2.2). Vectors with a wave activity flux magnitude below 2 m^2/s^2 are omitted. The reference vector is provided below the left column. Positive (negative) streamfunction is in solid (dashed) contours with an interval of 15×10^5 m/s^2.

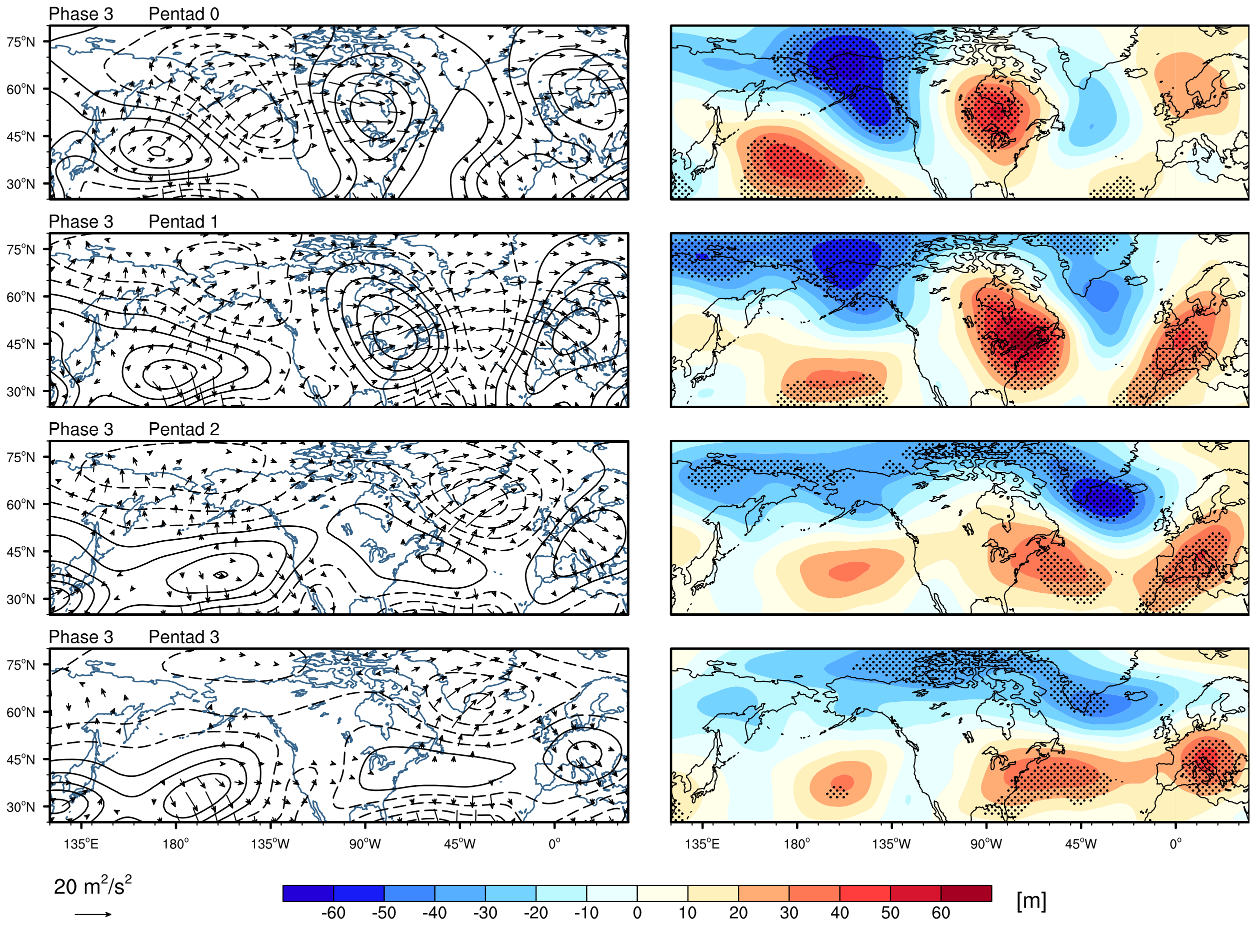

FIG. 2.4. Phase 3 composites of anomalous 200-hPa streamfunction (left column) and 500-hPa geopotential height (right column) for pentad 0 (top row) to pentad 3 (bottom row), where a pentad denotes a 5 day mean. See Figure 2.3 for explanation of all fields shown.

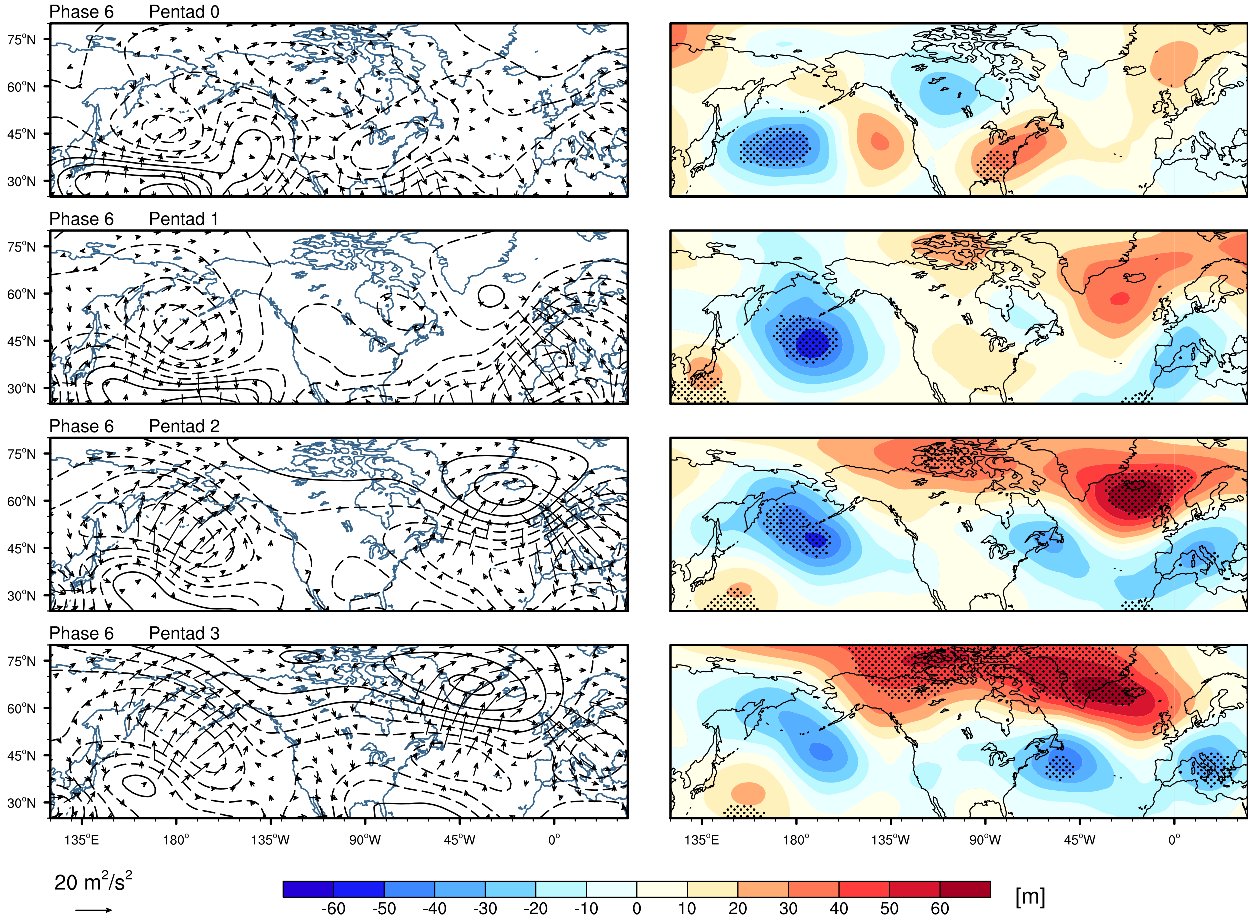

FIG. 2.5. Same as Figure 2.4, but for MJO phase 6.

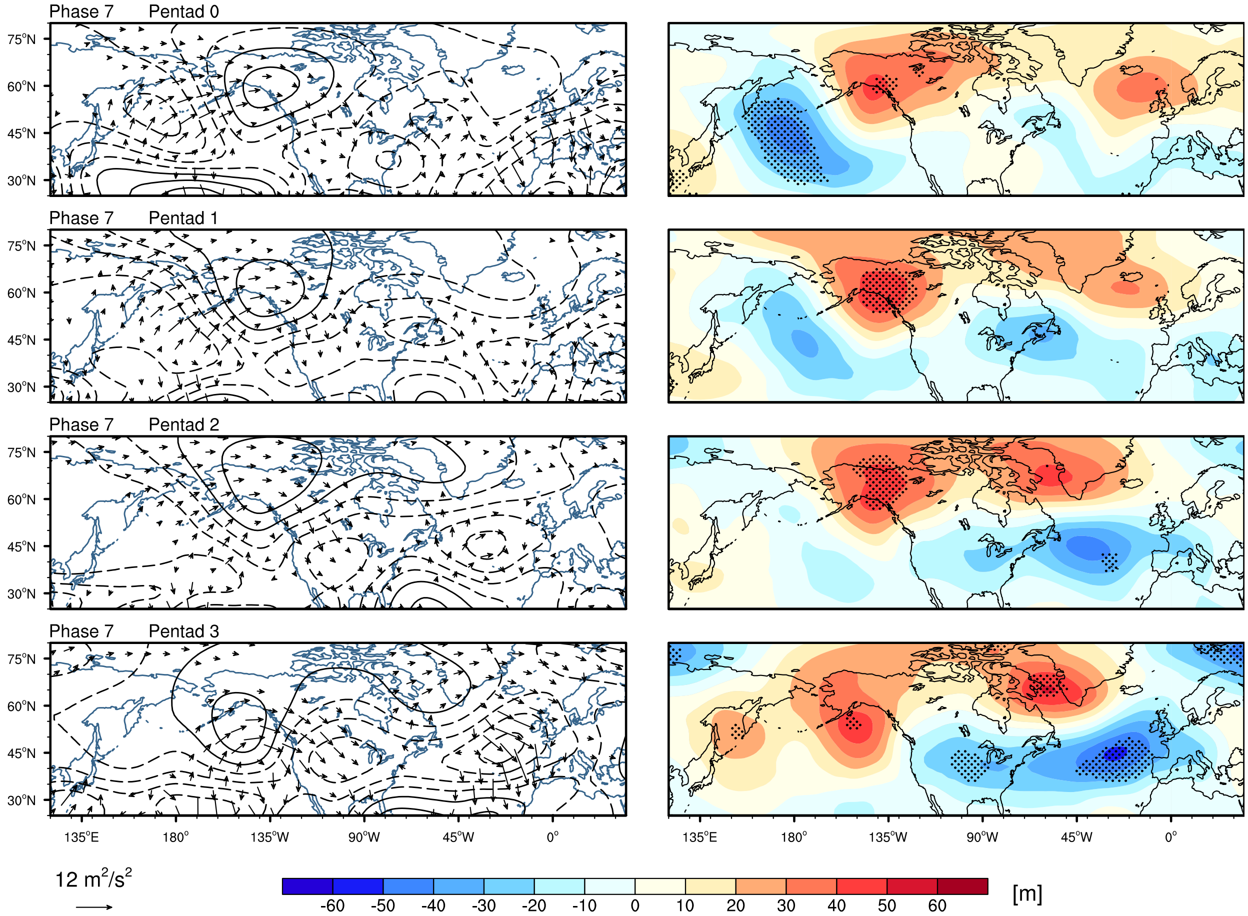

FIG. 2.6. Same as Figure 2.4, but for MJO phase 7.

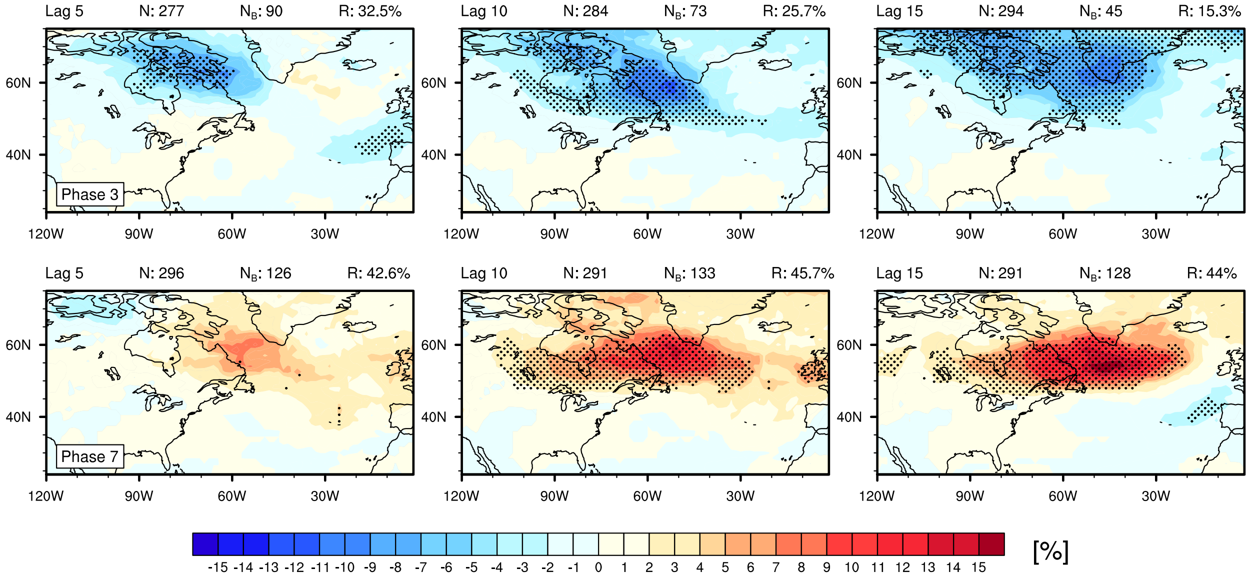

FIG. 2.7. Atlantic blocking frequency anomalies as determined by (2.1) for MJO phase 3 (top row) and phase 7 (bottom row). Shown are lag 5 (left panels), lag 10 (middle panels), and lag 15 (right panels), where a lag *n* represents the blocking frequency *n* days after the MJO phase. Blocking frequencies are shown as a deviation from the DJF mean. Black dotting demonstrates the anomalies found to be 95% significantly different from zero. For explanation of the values above each panel, see Section 2.2.3.

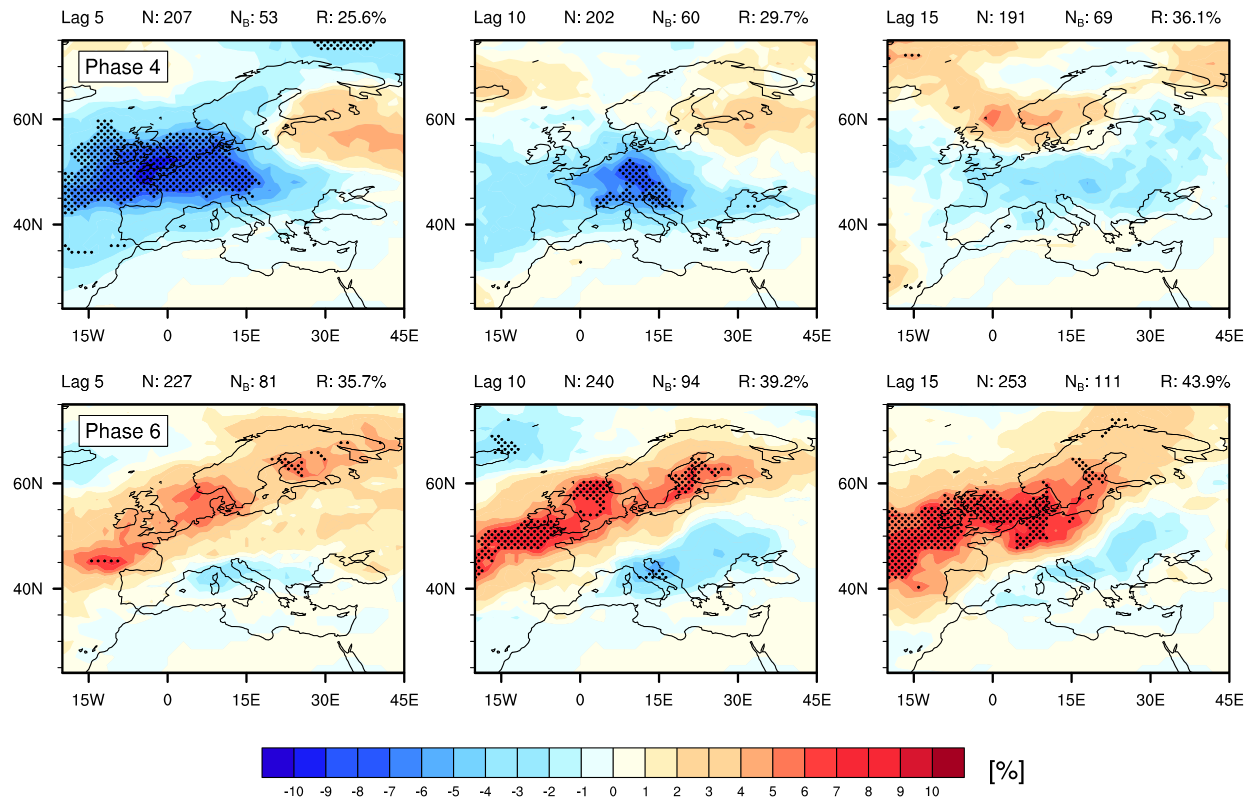

FIG. 2.8. European blocking frequency anomalies as determined by (2.1) for MJO phase 4 (top row) and phase 6 (bottom row). Shown are lag 5 (left panels), lag 10 (middle panels), and lag 15 (right panels). Blocking frequencies are shown as a deviation from the DJF mean. Black dotting demonstrates the anomalies found to be 95% significantly different from zero. For explanation of the values above each panel, see Section 2.2.3.

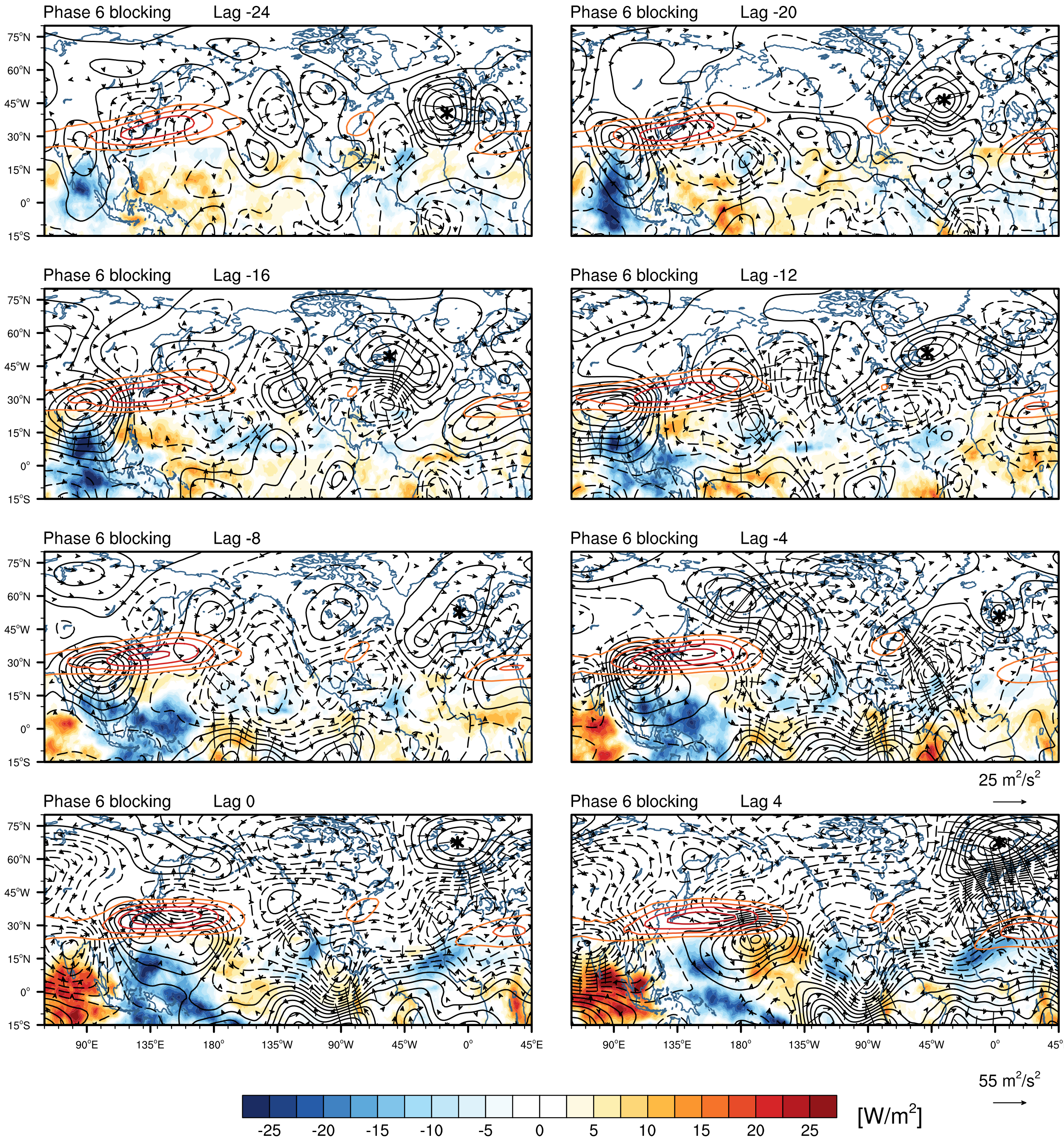

FIG. 2.9. Phase 6 composites for European blocking days associated with the bottom left panel of Figure 2.8 (lag 5). Shown are every four days from 24 days prior to four days after phase 6. Positive (negative) streamfunction is in solid (dashed) contours with an interval of 15 x 10^5 m/s^2. OLR anomalies [W/m^2] are shown south of 30°N in the shaded contours. Unshaded color contours represent 200-hPa mean zonal wind with an interval of 10 m/s beginning at 40 m/s. Also overlaid are wave activity flux vectors. For clarity, the bottom row has a reference vector of 55 m^2/s^2. All other panels have a reference vector of 25 m^2/s^2. Vectors with a wave activity flux magnitude below 2 m^2/s^2 are omitted. See text for explanation of the asterisk in each panel.

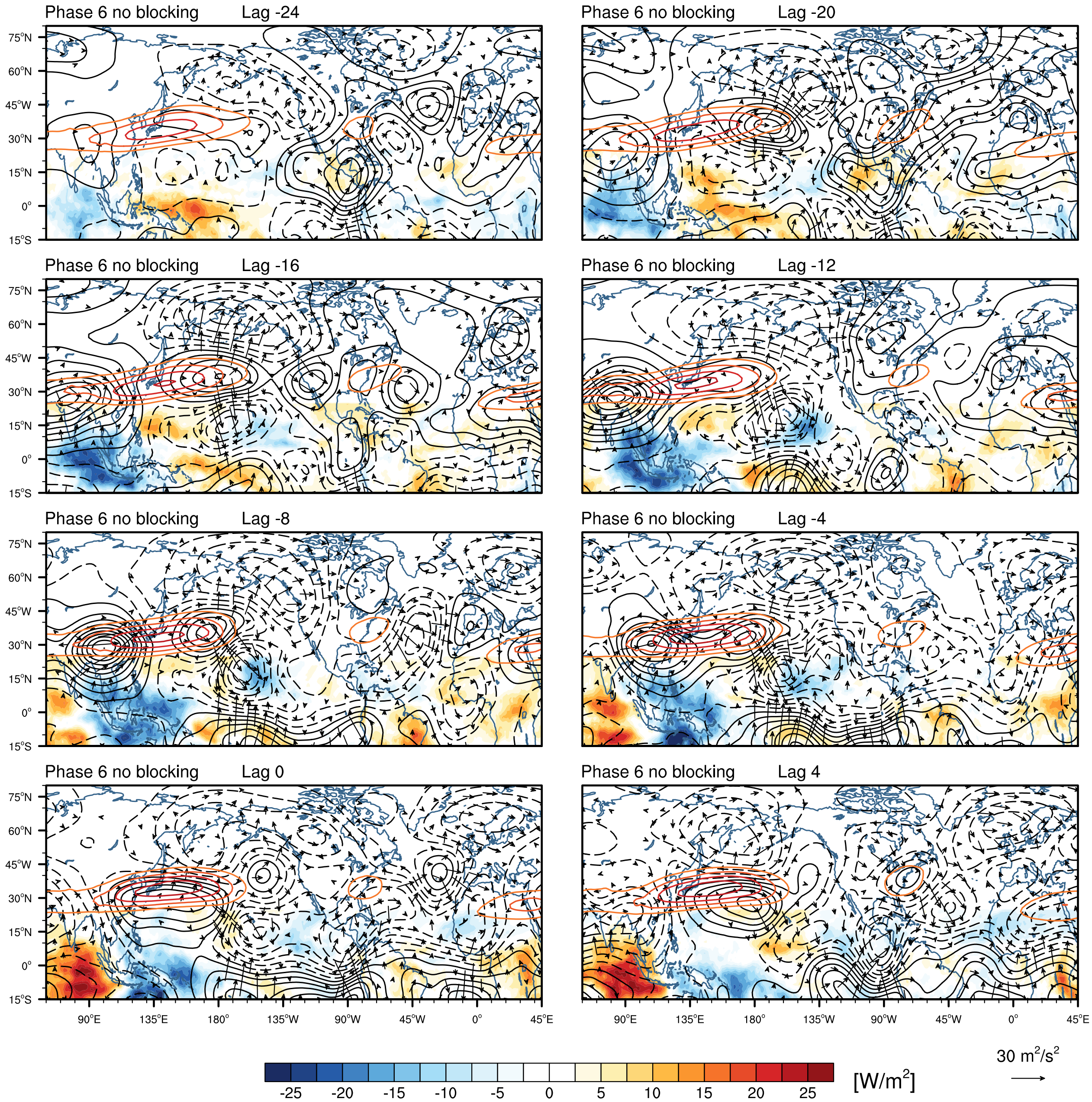

FIG. 2.10. Phase 6 composites for European non-blocking days associated with the bottom left panel of Figure 2.8 (lag 5). See Figure 2.9 for explanation of fields shown. All panels have a wave activity flux reference vector of 30 m^2/s^2, as indicated below the bottom right panel.

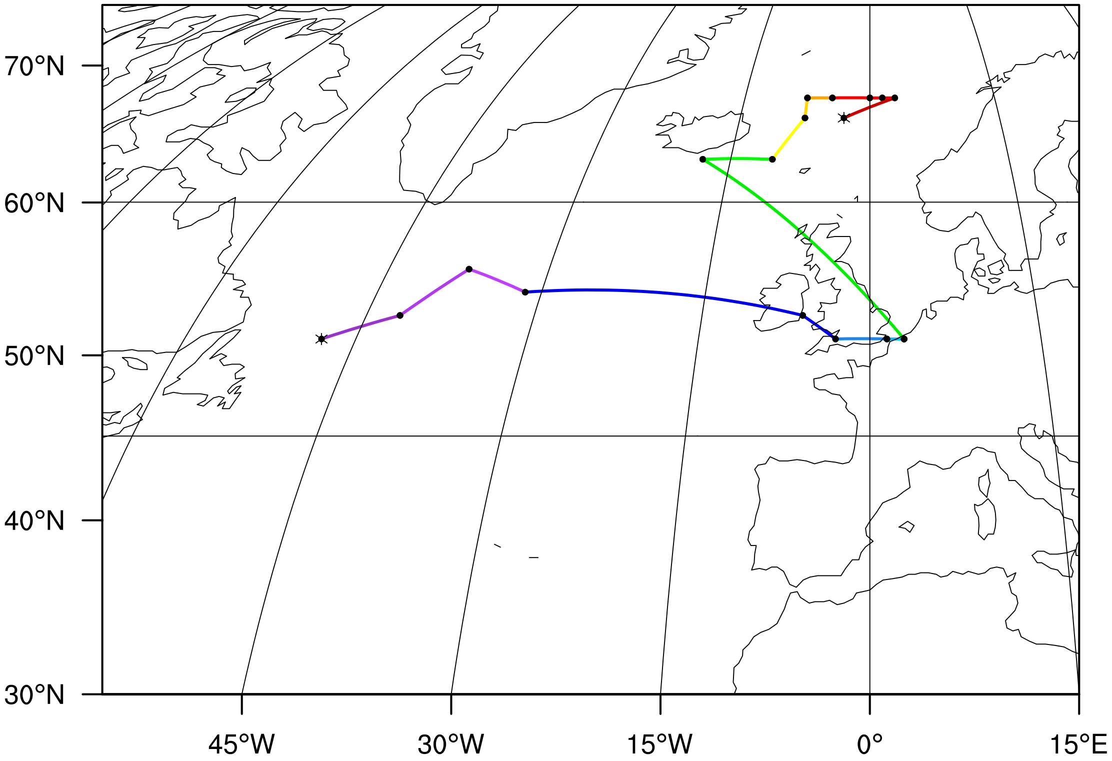

FIG. 2.11. Trajectory pathway of the pre-existing anticyclone described in the text, defined as the daily maximum anomalous streamfunction point in the Euro-Atlantic region from 12 days prior to 5 days after MJO phase 6 for days associated with phase 6 lag 5 European blocking. Trajectory ends are marked with an asterisk, where time moves from cooler to warmer colors. Black markers indicate the daily maximum point and correspond to the asterisks of Figure 2.9 at the appropriate lags. Note lags -4 and -5 have the daily maximum streamfunction at the same point, so only 17 points appear for the 18 lags.

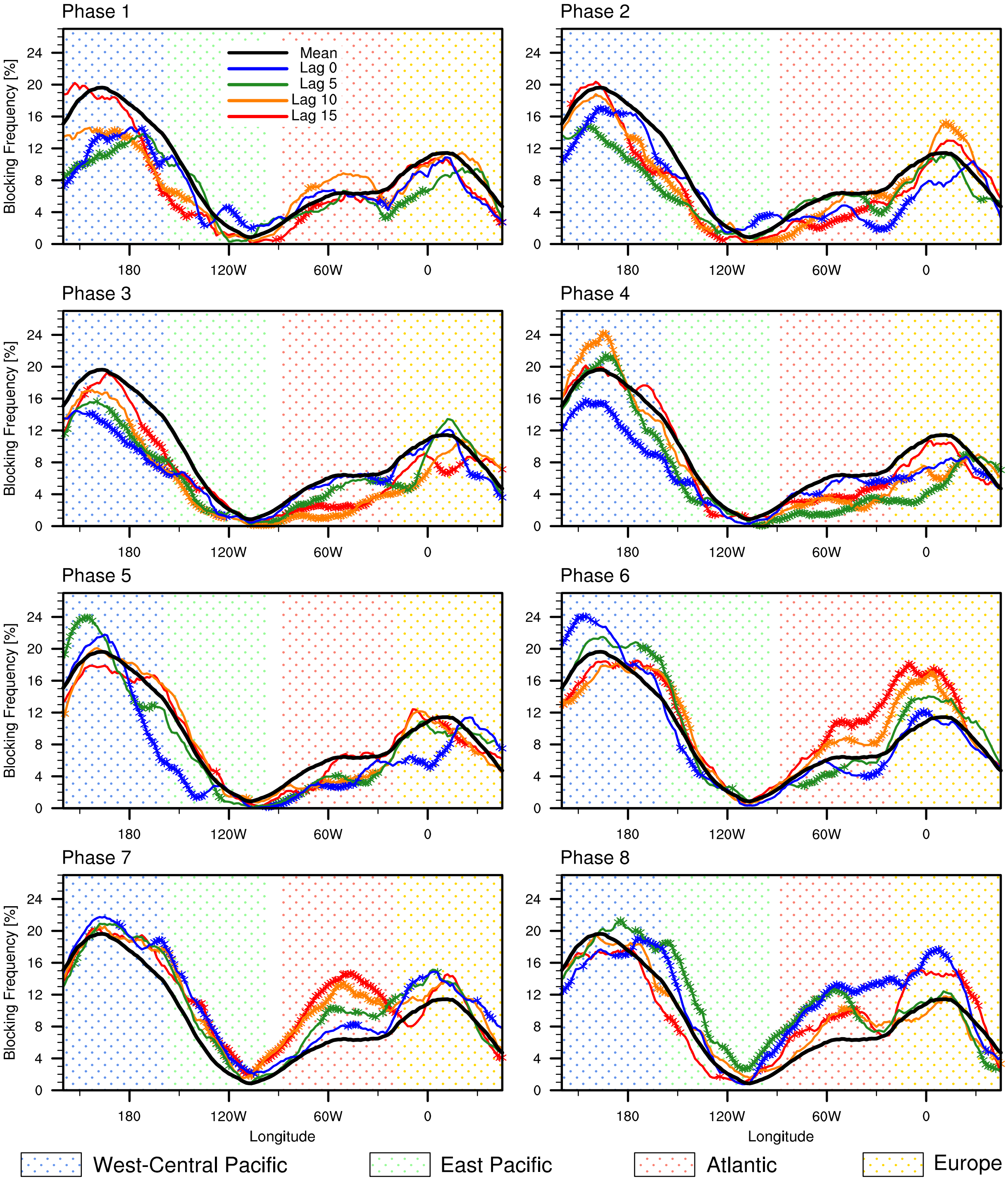

FIG. 2.12. Blocking frequency (%) averaged between 40°N - 60°N for the 8 phases of the MJO. Blocking frequencies are shown relative to MJO phase for lag 0 (blue), lag 5 (green), lag 10 (orange) and lag 15 (red), where a lag *n* represents the blocking frequency *n* days after the MJO phase. The mean DJF blocking frequency is overlaid in black in all panels for reference. Asterisks highlight those regions found to be 95% significantly different than the mean in each corresponding lag color. Each region is color dotted as defined in the legend below for reference.

CHAPTER 3: THE IMPACT OF THE MADDEN-JULIAN OSCILLATION ON HIGH-LATITUDE WINTER BLOCKING DURING EL NIÑO-SOUTHERN OSCILLATION EVENTS

3.1 Introduction

Intraseasonal variability in the tropical atmosphere is primarily governed by the Madden-Julian Oscillation (MJO; Madden and Julian 1971, 1972). The MJO is typically characterized by enhanced tropical convection flanked by suppressed convection that propagates eastward from the West Indian Ocean to the Central Pacific over a period of approximately 40 – 50 days. The convective heating anomalies can generate large-scale Rossby waves, or teleconnections, that significantly influence the extratropical circulation (e.g. Hoskins and Karoly 1981; Matthews et al. 2004; Seo and Son 2012). Recently, MJO teleconnections have been linked to significant changes in Northern Hemisphere winter blocking (Henderson et al. 2016 [hereby referred to as H16]; Hamill and Kiladis 2014; Moore et al. 2010). Atmospheric blocks are associated with extreme weather events in much of the northern hemisphere due to their persistent and quasi-stationary nature (e.g. Hoskins and Sardeshmukh 1987; Buehler et al. 2011).

During a blocking event, the mean westerly flow is “blocked” for up to several weeks, redirecting air masses and precipitation (e.g. Berggren et al. 1949; Masato et al. 2012). Classic mid-latitude blocking blocks the eddy-driven jet, whereas high-latitude blocking diverts its flow (e.g. Woollings et al. 2008). H16 demonstrated that high-latitude winter blocking over the Pacific is significantly suppressed when MJO teleconnections strengthen the 500-hPa geopotential height gradient, given that a height reversal at this level is often used to define blocking (e.g. Masato et al. 2013; Tibaldi and Molteni 1990). This typically occurs when MJO convection is enhanced over the Indian Ocean and Maritime Continent. When MJO convection is suppressed in this region and enhanced in the Pacific Ocean, MJO teleconnections weaken the height gradient and high-latitude Pacific blocking is more likely to occur. In addition, the frequency of blocking in the Atlantic is nearly doubled relative to the winter mean when MJO convection is suppressed over the Maritime Continent and enhanced in the West Pacific. When MJO convective anomalies are of the opposite sign, blocking is significantly suppressed (e.g. H16; Hamill and Kiladis 2014). These results suggest that MJO teleconnections may be an important tool in the mid-range forecasting of high-latitude blocking. However, the characteristics of MJO teleconnection patterns and the associated changes in blocking may be different when the mean large-scale circulation is altered, such as during El Niño-Southern Oscillation (ENSO) events.

ENSO is an ocean-atmosphere coupled mode in the tropical Pacific and the principal mode of global interannual variability (e.g. Rasmusson and Wallace 1983). Like the MJO, convective anomalies associated with ENSO act as heat sources that emit Rossby waves altering the extratropical circulation. The global changes associated with ENSO persist for timescales longer than the MJO, thereby affecting the basic state that the MJO feels and altering the pathways of MJO Rossby wave propagation. Takahashi and Shirooka (2014) and Moon et al. (2011) noted differences in the pathways of MJO teleconnections due to ENSO, and Roundy et al. (2010) demonstrated the nonlinearity of the combined patterns. In addition, Riddle et al. (2013) found that ENSO modulates many MJO extratropical impacts, such as the frequency of the Pacific-North American (PNA) pattern following MJO activity. ENSO events are also associated with changes in MJO convection; during El Niño, MJO activity extends further eastward (e.g. Hendon et al. 1999; Kessler 2001) and propagates faster (e.g. Pohl and Matthews 2007).

This study expands on the results of H16 by examining the altered pathways of MJO Rossby waves during ENSO events and their impact on Northern Hemisphere winter blocking frequency. Section 3.2 describes the data and indices utilized as well as the two-dimensional (2D) blocking index employed. ENSO-induced changes to the background flow and Rossby wave propagation are discussed in Section 3.3. Section 3.4 examines the teleconnection patterns associated with the MJO during ENSO phases, and Section 3.5 investigates how the MJO teleconnections alter blocking in the North Pacific and North Atlantic regions. Certain aspects of the MJO teleconnection patterns are further examined using a nonlinear baroclinic model (NLBM) in Section 3.6. Lastly, concluding remarks are provided in Section 3.7 and the main findings are summarized.

3.2 Methodology

3.2.1 Data

The primary dataset used here is the ERA-Interim Reanalysis (Dee et al. 2011) during boreal winter (December – February; DJF), provided at 1.5° x 1.5° horizontal grid spacing. The data used spans the period December 1979 to February 2016. Satellite-based outgoing longwave radiation (OLR) data is obtained from the National Oceanic and Atmospheric Administration (NOAA) National Climatic Data Center (NCDC; Lee et al. 2011) on a 1° x 1° horizontal grid and spans from 1979 to 2014.

The Real-time Multivariate MJO (RMM) indices are used to define the 8 phases of the MJO (Wheeler and Hendon 2004; http://www.bom.gov.au/climate/mjo/), as in H16. The RMM indices (RMM1 and RMM2) are the first two principal components of the combined empirical orthogonal functions of near-equatorial (15°S - 15°N) anomalous OLR, 200-hPa and 850-hPa zonal winds. The phases of the MJO are approximated by $\tan^{-1}(\frac{RMM2}{RMM1})$ and give a broad indication of the location of anomalous MJO convection. Only strong MJO events are examined here, defined when the RMM amplitude $\sqrt{(\mathrm{RMM1}^2 + \mathrm{RMM2}^2)}$ is greater than 1.

ENSO seasons are defined using the NOAA Climate Prediction Center (CPC) Oceanic Niño Index (ONI; http://www.cpc.noaa.gov/products/analysis_monitoring/ensostuff/ensoyears.shtml), which consists of a single value for each season. The index represents the three-month running mean of sea surface temperature (SST) in the Niño 3.4 region (5°N – 5°S, 90° W – 150°W). A winter season experiencing warm ENSO phase conditions occurs when the ONI exceeds 0.7°C, cold ENSO conditions when the ONI is less than -0.7°C, and neutral or normal conditions when it does not meet either threshold. Of the 37 DJF seasons examined here, 10 are characterized by warm ENSO conditions, 9 by cold ENSO conditions, and 18 by neutral conditions.

3.2.2 Two-dimensional blocking index

Following H16, the 2D blocking index defined by Masato et al. (2013) is utilized to examine the impact of the MJO on northern hemisphere blocking during ENSO phases. The blocking index is defined by:

$$B_i = \frac{2}{\Delta\phi}\int_{\phi_0}^{\phi_0+\frac{\Delta\phi}{2}} Z_i \partial\phi - \frac{2}{\Delta\phi}\int_{\phi_0-\frac{\Delta\phi}{2}}^{\phi_0} Z_i \partial\phi \tag{3.1}$$

where Z is 500-hPa geopotential height and ϕ is latitude. For a given longitude point, an instantaneous block occurs when the integrated geopotential height north of ϕ_0 is larger than the integrated height to its south, so that $B_i > 0$. Consistent with H16 and Masato et al. (2013), ϕ_0 is varied between 40°N and 70°N and $\Delta\phi = 30°$. The tracking algorithm used here is described in detail in H16. Only large-scale blocking events are examined, defined when at least 15° of longitude are blocked consecutively for at least 5 days. To calculate a blocking frequency, a dichotomous index is generated for each region where a 1 is given if all of the blocking criteria are met, and a 0 if they are not.

3.3 Rossby wave propagation during ENSO

3.3.1 ENSO changes to the basic state

The teleconnection patterns associated with the warm and cold phases of ENSO impact the basic state, or background flow, that the MJO experiences, thereby altering the propagation characteristics of the MJO-induced Rossby waves. The teleconnection patterns associated with the DJF warm and cold ENSO phases are shown in Figure 3.1. The 500-hPa geopotential height anomalies are shown since that is the field used to define blocking in (3.1), useful for the Section 3.5 discussion. During El Niño (top panel), a large-scale anomalous cyclonic anomaly persists over the Central Pacific basin, weakening the mean meridional geopotential height gradient between the Pacific high-latitudes and the mid-latitudes. Furthermore, the Pacific subtropical jet extends further eastward relative to neutral ENSO conditions (Figure 3.2 shading, middle panel). Over North America, an anomalous anticyclone exists with an anomalous cyclone to its southeast, resembling the positive phase of the PNA pattern. During La Niña, the opposite-signed teleconnection pattern exists with a negative PNA pattern (Figure 3.1, bottom panel), and is associated with a zonally contracted and stronger subtropical jet relative to El Niño conditions (Figure 3.2, bottom panel). The anticyclonic anomaly also strengthens the mean meridional geopotential height gradient between the mid- and high-latitudes.

3.3.2 Rossby wave propagation during ENSO events

The characteristics of Rossby wave propagation are largely determined by the upper-level zonal winds (e.g. Hoskins and Ambrizzi 1993). The impact of the zonal wind on the propagation of Rossby waves that may be forced by MJO heating is examined using the stationary wavenumber ($\mathrm{K_s}$) on Mercator coordinates, which provides a basic qualitative understanding of the behavior of Rossby waves. $\mathrm{K_s}$ is calculated following Karoly (1983) and Hoskins and Ambrizzi (1993):

$$\mathrm{K_s} = \left(\frac{a\beta_M}{\bar{u}_M}\right)^{\frac{1}{2}} \tag{3.2}$$

where $\bar{u}_M$ is the mean DJF 200-hPa Mercator zonal wind during El Niño and La Niña, a is Earth's radius, and β_M is the meridional gradient of absolute vorticity on a sphere, defined as:

$$\beta_\mathrm{M} = \frac{2\Omega\, cos^2\,\theta}{a} - \frac{\partial}{\partial y}\left[\frac{1}{\cos^2\theta}\frac{\partial}{\partial y}(\cos^2\theta\bar{u}_M)\right] \tag{3.3}$$

where Ω is Earth's rotational constant and θ is latitude. $\mathrm{K_s}$ is shown in Figure 3.3 for El Niño (top) and La Niña (bottom). Regions with mean easterly winds ($\bar{u}_M < 0$) are in white, and regions where the meridional gradient of absolute vorticity is reversed ($\beta_\mathrm{M} < 0$) are in black. In the subtropical jet, a vorticity anomaly forced by large-scale tropical convection can generate a wave train that propagates eastward within the jet, where $\mathrm{K_s}$ is maximized and acts as a waveguide. Rossby waves cannot propagate in regions where $\beta_\mathrm{M} < 0$, which is often observed on the northern flank of the subtropical jet. The $\beta_M < 0$ region during El Niño (Figure 3.3, top) extends approximately 40° further eastward than during La Niña (Figure 3.3, bottom). This suggests that on average, Rossby waves during El Niño cannot propagate northward until they travel further east relative to La Niña. As a result, it is expected that intraseasonal teleconnection patterns in the Pacific will be shifted eastward during El Niño events relative to La Niña events. This is in agreement with Henderson et al. (2017), who found that General Circulation Models (GCMs) exhibiting a subtropical jet that extends too far east produce an eastward shift in the Pacific teleconnection patterns forced by MJO heating.

3.3.3 MJO heating and RWS

In addition to basic state changes, previous studies have demonstrated that ENSO modifies the characteristics of MJO heating (e.g. Hendon et al. 1999). The longitudinal extent of 30 – 70 day filtered tropically-averaged OLR can be visualized in Figure 3.4 for warm (top panel) and cold (bottom panel) ENSO phases, where the y-axis is the 8 phases of the MJO. In agreement with previous studies, Figure 3.4 suggests that MJO convection extends further eastward during warm ENSO events than cold ENSO events (e.g. Hendon et al. 1999; Kessler 2001). For brevity, we will primarily focus on MJO phases 3 and 7, which are often used to represent the first and second halves of an MJO event and are associated with the strongest extratropical MJO response into the Atlantic (e.g. Lin et al. 2009; Lin et al. 2010; H16). These phases are also chosen to allow a comparison to the results of H16.

The anomalous OLR associated with MJO phase 7 during both phases of ENSO is shown in Figure 3.5a as an example of the ENSO influence on MJO heating. The warm and cold ENSO composites are composed of 83 and 88 days, respectively. In order to isolate the OLR anomalies associated with intraseasonal variability, a 30 – 70 day filter is applied prior to compositing by MJO phase. During MJO events, upper-level divergence associated with anomalous convection leads to vorticity anomalies within the subtropical jet that initiate Rossby wave trains. The initial vorticity forcing in the jet region is examined using the Rossby wave source (RWS; Sardeshmukh and Hoskins 1988), which is the sum of the advection of absolute vorticity and vortex stretching by the divergent wind:

$$\mathrm{RWS} = -\nabla \cdot (\mathbf{V}_\chi \zeta) = -\mathbf{V}_\chi \cdot \nabla \zeta - \zeta \mathrm{D} \tag{3.4}$$

where ζ is the absolute vorticity, $\mathbf{V}_\chi$ is the divergent component of the horizontal wind, and the divergence is defined by $\mathrm{D} = \nabla \cdot \mathbf{V}_\chi$. The amplitude of the RWS is strongly modulated by the strength and sharpness of the subtropical jet (Sardeshmukh and Hoskins 1988). The 200-hPa 30 – 70 day filtered RWS associated with MJO phase 7 during both ENSO phases is provided in Figure 3.5b. Also shown for reference is the $\mathrm{K_s} = 3$ contour as an estimate of the average turning latitude of MJO Rossby waves, which are typically characterized as wavenumber 2 – 4 (e.g. Seo et al. 2016; Henderson et al. 2017), and the $\beta_\mathrm{M} < 0$ region (hatched; see Figure 3.3).

During El Niño, the MJO phase 7 RWS is centered east of the La Niña RWS, likely due to the eastward extension of the positive OLR over the Maritime Continent during El Niño. This is also the case during MJO phase 3, with a RWS of the opposite sign (not shown), but it is not consistent across all MJO phases. Inconsistencies may be due to off-equatorial OLR, which in some cases has a similar eastward penetration in both ENSO phases (e.g., MJO phase 1, not shown), or due to changes in the subtropical jet vorticity gradients as the MJO propagates eastward. There are also differences between ENSO phases in the opposite-signed RWS near the exit region of the jet, which may be associated with differences in convection east of the Dateline (Figure 3.4; e.g. Henderson et al. 2017). In general, the RWS associated with most MJO phases (only phase 7 shown, Figure 3.5b) is stronger during La Niña than El Niño, which may be in part due to the stronger and sharper jet (Figure 3.2) or stronger convection (e.g. Figure 3.4). However, the number of days available for some MJO phases varies between warm and cold ENSO, which can impact the relative amplitude of a composite (e.g. Roundy et al. 2010).

3.4 MJO teleconnections during ENSO

3.4.1 MJO teleconnections

The RWS anomalies associated with MJO heating (Figure 3.5b) indicate the location of initial vorticity forcing for the MJO Rossby wave trains. MJO teleconnection patterns during ENSO events are examined using band filtered (30 – 70 days) lagged pentad 200-hPa streamfunction and 500-hPa geopotential height anomalies composited relative to MJO phases 3 and 7. This is the same compositing technique used in H16, but with the inclusion of a band pass filter to remove the circulation anomalies associated with ENSO. As in H16, the direction of Rossby wave propagation is investigated using wave activity flux vectors (**W** vectors; Takaya and Nakamura 2001):

$$\mathbf{W} = \frac{1}{2|\boldsymbol{U}|}\begin{bmatrix} U(\psi_x^2 - \psi\psi_{xx}) + V(\psi_x\psi_y - \psi\psi_{xy}) \\ U(\psi_x\psi_y - \psi\psi_{xy}) + V\left(\psi_y^2 - \psi\psi_{yy}\right) \end{bmatrix} \tag{3.5}$$

where ψ is the 200-hPa anomalous pentad streamfunction, the average DJF 200-hPa zonal and meridional winds are U and V, respectively, and the subscripts represent partial derivatives of ψ in the x and/or y directions. **W** vectors are parallel to the Rossby wave group velocity, providing a snapshot in time of Rossby wave packet propagation. The MJO phase 3 and 7 teleconnection pattern composites are shown in Figures 3.6 – 3.9 for warm and cold ENSO events. Pentad 200-hPa streamfunction anomalies and the associated **W** vectors are shown on the left column of each figure. Anomalous 500-hPa geopotential height is also provided (right column) since it is the field used to define blocking in (3.1). As in H16, dotted regions indicate geopotential height anomalies that are significantly different from zero at the 95% confidence level using a Student's *t*-test. The number of samples is estimated by dividing the number of days in each MJO phase by the average duration of an MJO phase across all MJO phases, which is found to be 5 (e.g. H16; Alaka and Maloney 2012). This average value is found to be the same during both El Niño and La Niña events, although the duration of an individual MJO phase varies depending on MJO and ENSO phase.

During MJO phase 3, an anticyclonic anomaly develops at the exit region of the subtropical jet during both ENSO phases (Figures 3.6 and 3.7, top panels). The anticyclonic anomaly extends further east during El Niño (Figure 3.6) than La Niña (Figure 3.7), likely due to the large difference in the zonal extent of the subtropical jet (Figure 3.2; e.g. Henderson et al. 2017), in agreement with the discussion of Figure 3.3. This behavior becomes even more apparent during Pentad 1, with the cyclonic anomaly over Northwest North America also demonstrating a similar shift. Rossby waves propagate northeast from the anticyclonic anomaly forming a wave train over North America, as shown by the **W** vectors (Figures 3.6 – 3.7; top panel). These Pacific Rossby wave patterns are in agreement with those in Takahashi and Shirooka (2014; their Figure 11). During El Niño, Rossby waves in pentad 1 (Figure 3.6; second panel) propagate northeast from the anomalous anticyclone over northeast North America (anticyclone also shown in pentad 0; top panel), forming a pattern in the Atlantic that resembles the positive phase of the NAO by pentad 2. During La Niña (Figure 3.7), the anticyclonic anomaly over northeast North America strengthens by pentad 1 (second panel); however, a NAO-like pattern is not apparent. The relationship between the MJO and the NAO during

ENSO phases will be discussed further in Section 3.5, which considers the combined influence of the MJO and ENSO.

The MJO phase 7 teleconnection patterns during El Niño and La Niña are shown in Figures 3.8 and 3.9, respectively. For both ENSO phases, **W** vectors suggest northeast Rossby wave packet propagation from the cyclonic anomaly near the jet exit region to the anticyclonic anomaly over northwest North America (Figures 3.8 – 3.9; pentads 0 and 1). However, the cyclonic anomaly during La Niña extends further west relative to that of El Niño in the mid-latitudes, a difference likely due to the lesser eastward extent of the jet during La Niña (Figures 3.2 – 3.3). In addition, the teleconnection pattern during La Niña is of higher amplitude than that during El Niño. This difference in amplitude may be due to the stronger RWS during La Niña (Figure 3.5), given that MJO phase 7 has a similar number of days during both ENSO phases. During El Niño, MJO Rossby wave packets propagate from the Pacific over North America during pentads 0 and 1 (Figure 3.8; left column). The Rossby waves lead to a dipole structure over northeast North America and Greenland (Figure 3.8), which is not observed during La Niña (Figure 3.9). The dipole structure persists through pentad 3, or approximately 15 – 19 days after MJO phase 7 (Figure 3.8). The Atlantic pattern is similar to cluster 4 in Riddle et al. (2013; their Figure 3), which they compare to a negative Arctic Oscillation (AO) – like pattern. In agreement with our results, the study noticed the increased occurrence of this pattern following MJO phase 7 during El Niño, and note that further work is needed to understand why the increased frequency of the pattern exists.

3.5 MJO impacts on blocking during ENSO

The influence of the MJO on Pacific and Atlantic high-latitude blocking is examined following the same compositing technique and significance testing as in H16. The dichotomous blocking indices of the Pacific and Atlantic, which indicate the presence of a large-scale persistent block, are first composited relative to ENSO phase to determine the mean DJF blocking frequency (Figure 3.10; middle and bottom left panels). The blocking frequency maximum over the West-Central Pacific is largely influenced by the meridional gradient of geopotential height, which is climatologically weak in that region (e.g. Woollings et al. 2008). During El Niño, this blocking frequency maximum has slightly higher amplitude than the DJF climatological mean (Figure 3.10; top left panel) and neutral ENSO conditions (not shown). During La Niña, however, the frequency of high-latitude Pacific blocking is largely reduced. As previously discussed, the high-latitude meridional gradient of geopotential height is strengthened by the anomalous anticyclonic anomaly response to La Niña tropical heating. Blocking as defined by (3.1) specifically seeks a reversal in the geopotential height gradient, which is harder to achieve during La Niña. During El Niño, the cyclonic anomaly (Figure 3.1) acts to weaken the meridional gradient where it is already relatively weak, so that the impact is not as great.

Blocking frequency anomalies composited relative to MJO and ENSO phase are shown in Figures 3.11 and 3.13 for the Pacific and Atlantic, respectively, and are calculated by subtracting the DJF mean (Figure 3.10; top panels) from each composite. The blocking frequencies are lagged relative to MJO phase, as indicated on the top left of each panel, where an *m* day lag is the blocking frequency *m* days after that MJO phase. Dotted regions indicate that the blocking frequency anomalies are significantly different from zero at the 95% significance level using a moving-blocks bootstrap test, also used in H16. The moving-blocks bootstrap is calculated independently for each lag, MJO and ENSO phase. Similar to a traditional bootstrap, the test approximates the data characteristics by sampling the data randomly, with replacement; however, the samples are taken in overlapping blocks of length l in order to preserve the data autocorrelation (e.g. Wilks 2011).

The sampled blocks of length l are joined together to create bootstrap samples of size N, and the process is repeated 5000 times. Values of N are provided above each panel in Figures 3.11 and 3.13, where N is the total number of days in that MJO and ENSO phase. Block length l is the estimated duration of each MJO phase, as in H16, calculated for each ENSO phase. During El Niño, the block lengths are found to be $l = 4, 5, 7, 6, 4, 5, 6, 6$ for MJO phases 1 – 8, respectively. During La Niña, $l = 4, 6, 5, 5, 6, 5, 6, 5$ for phases 1 – 8, respectively. For a more detailed description of the moving-blocks bootstrap and block length calculation, see H16. Also shown in Figures 3.11 and 3.13 is the number of days in that MJO and ENSO phase that observed large-scale persistent blocking (N_B), and a ratio $R = N_B/N$, indicating the percent of days that experienced blocking m days after that MJO phase during an ENSO event.

3.5.1 Pacific blocking

Based on the findings of H16, MJO phases 1 – 5 are associated with significant suppression in Pacific high-latitude blocking due to a strengthening of the meridional geopotential height by the MJO teleconnection patterns. This suppression in blocking shifts eastward with MJO phase as the MJO-induced geopotential height anomalies move eastward. This suppression is evident during ENSO neutral years (not shown); however, there are some key differences during cold and warm ENSO events. Pacific blocking anomalies during and following MJO phase 3 during warm and cold DJF seasons are shown in Figure 3.11a and 3.11b (top rows), respectively. The neutral (not shown) and cold (Figure 3.11b, top row) ENSO phases demonstrate a significant suppression in Central Pacific blocking, whereas anomalies are not significant for warm ENSO events (Figure 3.11a, top row). In all lags investigated here, significant blocking anomalies during warm ENSO are primarily observed in the latter half of the MJO cycle, whereas during La Niña significant blocking anomalies primarily occurs in the first half of the MJO cycle. To understand why these differences exist, the combined impact of ENSO and MJO teleconnections is examined.

The unfiltered 500-hPa geopotential height anomalies for MJO phase 3 pentad 1 is shown in Figure 3.12 for warm (top left) and cold (bottom left) ENSO phases. These unfiltered patterns are calculated by removing the long-term daily mean and the first three harmonics of the seasonal cycle, and demonstrate the combined impact of ENSO and the MJO 5 – 9 days after MJO phase 3. During El Niño, the combined impact of ENSO and MJO phase 3 is relatively weak. This is because the negative Pacific geopotential height anomaly associated with El Niño (Figure 3.1, top) is partially cancelled out by the significant positive geopotential height anomaly in the same region that follows MJO phase 3 (Figure 3.6, second panel). These teleconnection patterns in the Pacific act destructively, and no significant changes in blocking occur. During La Niña, however, there is a strong anticyclonic anomaly over the East Pacific between 30°N – 60°N (Figure 3.1), while MJO phase 3 pentad 1 is associated with a cyclonic anomaly north of approximately 50°N (Figure 3.7, second panel). Combined, a strong dipole exists over the eastern half of the North Pacific basin (Figure 3.12, bottom left). This dipole acts to strengthen the geopotential height gradient and blocking is significantly suppressed along the southern and western flanks of the cyclonic anomaly. For similar reasons, significant suppression of Pacific blocking is observed following MJO phases 1 – 5 during La Niña (only phase 3 shown).

The latter half of the MJO life cycle (MJO phases 6 – 8) is associated with the eastward propagation of a negative geopotential height anomaly near the Pacific subtropical jet and a positive geopotential height anomaly to its northeast (e.g. H16). This pattern is evident following MJO phase 7 for both ENSO phases (Figure 3.8 – 3.9), however the blocking impacts greatly differ between warm and cold ENSO conditions (Figure 3.11; second and fourth row). During El Niño, a significant persistent increase in blocking occurs across the north Pacific basin, lasting from approximately 5 to 15 days after MJO phase 7 (Figure 3.11a, bottom row). The persistent increase is reflected in other MJO phases, with a significant increase in blocking frequency following MJO phases 6 – 8 (only phase 7 shown). This significant increase in blocking frequency does not appear in the cold ENSO composites (Figure 3.11b, bottom row).

These differences can be better understood by examining the combined influence of ENSO and the MJO on the large-scale circulation. The unfiltered geopotential height anomalies following MJO phase 7 are shown in Figure 3.12 (right column). Both El Niño (Figure 3.1, top) and MJO phase 7, pentad 1, (Figure 3.8, second row) are associated with anomalously negative geopotential height in the Central Pacific, suggesting that the Rossby waves associated with both forms of variability will act constructively to amplify the anomaly in that region of the Pacific. The individual teleconnections (Figures 3.1 and 3.8) suggest that the Pacific basin anomalies are only destructive in the Gulf of Alaska, as observed by the reduced southward extent of the positive geopotential height anomaly over northwest North America in Figure 3.12 relative to Figure 3.8. The negative Central Pacific geopotential height anomaly is flanked by positive height anomalies to its north (Figure 3.12, top right), indicating that there is a weakening of the mean meridional geopotential height gradient throughout the North Pacific basin so that a reversal, and hence a block as defined by (3.1), is easier to achieve.

During cold ENSO conditions, Figure 3.12 (bottom right) suggests that the anomalies west of the Dateline are relatively weak. Furthermore, the Pacific anticyclonic anomaly associated with La Niña (Figure 3.1, bottom) acts to extend the anticyclonic anomaly that follows MJO phase 7 (Figure 3.9) southward, reaching approximately 30°N. The anticyclonic anomaly coincides with an increase in blocking frequency along western North America (not shown), suggesting a possible impact on East Pacific mid-latitude blocking.

3.5.2 Atlantic blocking

In the Atlantic basin, blocking is significantly suppressed following MJO phase 3 when considering all DJF seasons (e.g. H16; Hamill and Kiladis 2014) and coincides with a positive NAO pattern (e.g. Lin et al. 2009; Cassou 2008); a relationship also observed during ENSO neutral years (not shown). Figure 3.13b (top row) indicates that Atlantic high-latitude blocking is suppressed following MJO phase 3 during cold ENSO conditions, although only significant at the highest amplitudes. During El Niño, suppressed regions that meet the significance criteria are less consistent between lags, suggesting a weaker relationship between the MJO and blocking (Figure 3.13a, top row). In addition, suppressed regions are of weaker amplitude during El Niño; however, there is a large difference in sample size that can impact the relative amplitude of the anomalies (see N values above each panel). Filtered MJO teleconnection patterns demonstrate that a positive NAO-like pattern follows MJO phase 3 during El Niño (Figure 3.6) but not during La Niña events (Figure 3.7). However, when considering both ENSO and the MJO, an NAO-like pattern emerges during La Niña at pentad 1 (Figure 3.12, bottom left) that is not as apparent during El Niño (top left). The NAO-like pattern during La Niña persists through pentads 2 and 3 following MJO phase 3 (not shown). A weaker NAO-like pattern does appear during El Niño at pentad 2 (not shown), weakening further by pentad 3. This may be in agreement with Roundy et al. (2010) who noted that the relationship between the MJO and the NAO appears amplified relative to certain MJO phases during La Niña. While the presence and persistence of an NAO pattern does not provide an explanation for blocking occurrence (e.g. Woollings et al. 2008; Davini et al. 2012), it suggests that following MJO phase 3, blocking may occur less often during La Niña than during El Niño.

During El Niño, a significant increase in Atlantic blocking frequency is observed during and following MJO phase 7 (Figure 3.13a, bottom row; lag 0 not shown), with maximum anomalies tripling that of the DJF mean (Figure 3.10) at later lags. A significant increase in Atlantic blocking was also observed in H16 when considering all DJF seasons; however, the increase in blocking following phase 7 is not significantly different from zero when considering only ENSO neutral years (not shown), and only significant in a small region at later lags during La Niña (Figure 3.13b, bottom row). This suggests that the inclusion of El Niño years was largely driving the significant Atlantic blocking increase discussed in H16. The intraseasonal teleconnection patterns during and following MJO phase 7 (Figures 3.8 and 3.9) show a large difference in the Atlantic basin between the two ENSO phases. The persistent dipole pattern in Figure 3.8 is likely in part due to the increase in blocking, given the quasi-stationarity of the anomalies and the large percentage of blocking days that follows phase 7 during El Niño (R=~73% of days at lags 5 and 11; Figure 3.13a, bottom row). One possibility is that the MJO initially provides the dipole anomaly and transient eddies act to reinforce and maintain the blocking pattern. The role of MJO heating on the development of the dipole anomaly will be investigated using the NBLM in Section 3.6, and the role of transient eddies will be discussed next.

3.5.3 The role of eddies in Atlantic blocking

The persistence and quasi-stationarity of blocking patterns cannot be fully explained by MJO stationary waves since the MJO may evolve into the next phase with a timescale much shorter than the longevity of a block. Green (1977) found that eddies traveling along the storm track helped maintain the blocking pattern examined in their study by transporting low potential vorticity (PV), or anticyclonic vorticity, into the block. In order to better understand the role of eddies in relation to the MJO, the horizontal **E**-vector is used as formulated by Trenberth (1986):

$$\mathbf{E} = \left[\frac{1}{2}\left(\overline{\mathrm{v}'^2} - \overline{\mathrm{u}'^2}\right), -\overline{\mathrm{u}'\mathrm{v}'}\right] \cos\theta \tag{3.6}$$

where u and v are the 300-hPa zonal and meridional winds, respectively, and θ is latitude. The primes indicate a 2 – 6 day band-pass filter and the overbar a time mean. The **E**-vector as defined by (3.6) examines the transport of angular momentum by transient eddies, where its convergence indicates the eddy activity acts to decelerate the local mean westerly wind, thereby reinforcing the block (Trenberth 1986). Here we examine the **E**-vectors associated with MJO phase 7 during El Niño, which is associated with enhanced and persistent blocking (Figure 3.13).

Atlantic **E**-vectors for MJO phase 7 during El Niño are shown in Figure 3.14 (top row), as well as the corresponding **E**-vector divergence (color shading). Also overlaid is the associated composite mean 300-hPa transient eddy kinetic energy $\left[\mathrm{TEKE} = \frac{1}{2}(\mathrm{u}' + \mathrm{v}')^2\right]$, which estimates the location of the storm track (e.g. Pelly and Hoskins 2003). The **E**-vector fields are smoothed by lowering the wind data resolution to a 2.5° grid prior to the **E**-vector calculation. The anomalous Atlantic pattern is observed during (Figure 3.8, pentad 0) and following MJO phase 7 (pentads 1 – 3). We therefore examine eddy activity during MJO phase 7 (Figure 3.14, left panel) and 10 days after phase 7 (right panel), in which approximately 73% of days contain a large-scale block largely concentrated south of Greenland and over the Labrador Sea (Figure 3.13a, bottom row).

During MJO phase 7, **E**-vector convergence south of Greenland indicates that eddy activity is acting to decelerate the westerly flow near the center of and in the northern portion of the storm track (Figure 3.14). The deceleration of the flow coincides with the initial increase in Greenland blocking frequency (Fig. 3.13a, lag 0 not shown). **E**-vector convergence is also observed along the northern flank of the storm track at lag 10 (Fig. 3.14, right panel). In the presence of an anticyclone, the deceleration of the flow suggests eddy activity acts to reinforce blocking activity by depositing low PV air into the anticyclone. During and following MJO phase 7, eddy activity accelerates the westerly flow along the southern flank of the storm track, indicated by **E**-vector divergence. This suggests that eddy activity acts to shift the storm track southward (see TEKE contours, lag 10), a characteristic commonly associated with Greenland blocking (e.g. Woollings et al. 2008).

E-vector analysis provides some understanding into the maintenance and persistence of the blocking pattern shown in Figures 3.8 and 3.13a. While **W** vectors suggest MJO Rossby wave propagation is involved in the development of the dipole anomaly (Figure 3.8), a cause and effect argument is difficult because composite analysis does not distinguish between the geopotential height anomalies generated by the significant increase in blocking and the anomalies generated by the MJO Rossby waves. To better understand the role of the MJO on the dipole anomaly, a simple nonlinear model is employed.

3.6 Nonlinear Baroclinic Model (NLBM) experiments

The impact of the MJO on the atmospheric circulation during ENSO events is investigated using the nonlinear dry baroclinic model introduced by Yasui and Watanabe (2010). A nonlinear model is used since Atlantic basin variability, such as the NAO pattern, requires nonlinear processes to adequately represent it (e.g. Feldstein 2003). The NLBM is a simplified dry atmospheric general circulation model derived from primitive equations on a sphere, and has been used by various studies to examine the nonlinear response to anomalous forcing (e.g. Nakamura et al. 2015; Kosaka et al. 2012). The NLBM is first used to examine the differences between the MJO phase 3 teleconnection patterns for different ENSO phases, and help determine if these changes are primarily explained by the ENSO-induced differences in basic state and MJO heating rather than an effect of the blocking anomalies themselves. Specifically, the NLBM will help determine if the cold ENSO phase 3 Pacific teleconnection pattern is primarily explained by the ENSO-induced differences in basic state and MJO heating or due to the significant blocking anomalies (Figure 3.11b; top row). In addition, the model is used to examine the role of the MJO on the phase 7 Atlantic blocking pattern discussed in the previous section.

3.6.1 NLBM description and setup

The NLBM calculates the nonlinear response to a prescribed forcing given a user-specified basic state. The model has a T42 horizontal resolution and 20 vertical levels on σ-surfaces. It employs biharmonic diffusion with an e-folding timescale of 1 day for the largest wavenumbers. The prescribed basic state is maintained by nudging the temperature back towards the basic state every 10 days using Newtonian cooling (e.g. Nakamura et al. 2015). The experiments are composed of two control runs and the MJO-forcing runs. The two control runs are initialized with the DJF El Niño and La Niña basic state, respectively, calculated from ERA-interim 1979 – 2016 data. The MJO-forcing runs are prescribed an ENSO basic state and initialized using a propagating MJO heat source, discussed below. The anomalous response to MJO heating is then the difference between the MJO-forced run and the control run of the same ENSO basic state.

The apparent heat source (Q_1; Yanai et al. 1973) anomaly associated with the MJO during a given ENSO phase is used to force the NLBM. Q_1 is calculated as a residual of the dry static energy (s) budget, given by:

$$Q_1 = \frac{\partial s}{\partial \mathrm{t}} + \nabla \cdot (s\mathbf{V}) + \frac{\partial (s\omega)}{\partial \mathrm{p}} \tag{3.7}$$

where $s = \mathrm{c_p T + gz}$, in which $\mathrm{c_p}$ is the specific heat capacity of air at constant pressure, T is temperature, g is the gravitational constant, and z is height. In (3.7), ω is the pressure velocity and **V** is the horizontal wind vector. Anomalies in apparent heating (Q_1') are calculated by applying a 30 – 70 day band-filter to remove diabatic heating anomalies associated with ENSO and other types of variability, and compositing by MJO and ENSO phase. For each ENSO phase, a 48-day propagating heat source is derived by using the eight MJO Q_1' phase composites and linearly interpolating, under the assumption that each MJO phase spans approximately 6 days. The idealized 48-day MJO cycle was also used in Henderson et al. (2017), which used a propagating heat source to force the linear version of the model used here (LBM; Watanabe and Kimoto 2000).

For each MJO forcing run, it is important to consider what MJO phase will begin each 48-day cycle. It is possible that the teleconnection patterns during a given MJO phase are influenced by many MJO phases before it, although the evolution of MJO events are often more episodic than continuous. The average MJO evolution during ENSO events is examined using the two-dimensional RMM phase-space (Figure 3.15), where the x and y axes are RMM1 and RMM2, respectively. A typical strong MJO event is characterized by counter-clockwise motion in the RMM phase-space and an amplitude greater than 1, indicated by the unit circle in the figure. Average MJO persistence is calculated in a similar way as in Rashid et al. (2011) and Henderson et al. (2017), which computed the average phase-space trajectory and decay timescale (i.e. the moment in which the trajectory falls below the unit circle) of strong MJO events beginning at each phase-space quadrant. However, we calculate these trajectories backwards in time (i.e. clockwise motion in phase-space) since we are interested in determining which MJO phase in which to begin each 48-day Q_1' forcing.

The initial point of each trajectory, marked by a large filled circle in Figure 3.15, is the average RMM value during a strong MJO phase quadrant during El Niño (red) and La Niña (blue). For reference, trajectories during neutral years are also provided in black. The backwards trajectories are initialized in MJO phases 2 – 3 (Figure 3.14; bottom quadrant), 4 – 5 (right quadrant), 6 – 7 (top quadrant), and 8 – 1 (left quadrant). Here we focus on the backward trajectories initialized in MJO phases 2 – 3 and phases 6 – 7 since we are interested in the MJO phase 3 and 7 teleconnection patterns. The MJO phase in which the trajectories fall below the unit circle is then the average phase that an MJO event begins with that leads to a strong MJO phase 2 – 3 or 6 – 7. Figure 3.15 suggests that MJO events persist very differently depending on ENSO and MJO phase. For example, a strong MJO phase 2 – 3 during La Niña is preceded on average by relatively persistent MJO activity beginning in the previous MJO cycle. During El Niño and neutral conditions, however, the trajectory does not extend beyond one MJO phase. MJO persistence also varies by ENSO phase for the MJO phase 6 – 7 trajectories. During El

Niño, more persistent MJO activity precedes a strong MJO phase 6 – 7 than during La Niña, with an initial phase 4 during El Niño. Figure 3.15 provides a useful guide on what preceding MJO phase to initiate the propagating heat source in the NLBM experiments in order to determine heating anomalies during a target phase.

3.6.2 NLBM experiments: Phase 3 Pacific teleconnection patterns

This section will use the NLBM to examine the MJO phase 3 differences as a function of ENSO phase. The propagating Q_1' for the El Niño run is initiated using MJO phase 2, whereas the La Niña run is initiated using MJO phase 8. These initialization phases provided the results most comparable to Figures 3.6 – 3.7. Figure 3.16 (top panel) shows the El Niño 500-hPa geopotential height NLBM response to MJO heating averaged from 21 to 26 days after initialization of the run, or 14 to 19 days after MJO phase 3 begins. Figure 3.16 (bottom panel) is the response to MJO heating using a La Niña basic state, and is shown as the average from days 25 – 30 after initialization of the run, or approximately 7 to 12 days after MJO phase 3 begins. This earlier timeframe is shown since the significant anomalies that follow MJO phase 3 during La Niña are largely confined to the earlier MJO lagged pentads (Figure 3.7).

The NLBM response using the El Niño basic state and MJO heating (Figure 3.16; top) shows many similarities to the composites following MJO phase 3, particularly pentads 1 – 2 (Figure 3.6; second and third rows). In agreement with Figure 3.6, the NLBM response has an anticyclonic anomaly over the East Pacific and a meridionally elongated cyclonic anomaly over western North America. In the NLBM run, these anomalies develop in the location shown. Relative to the La Niña NLBM run (Figure 3.16; bottom), the El Niño Pacific anomalies are shifted east in agreement with our previous discussion. In the La Niña NLBM run, the anticyclonic anomaly forms and maintains west of 150°W with the cyclonic anomaly over the East Pacific, in agreement with Figure 3.7, pentads 0 – 1 (first two rows). The shift demonstrated here is similar to the LBM results of Henderson et al. (2017), who found an eastward shift in the Pacific MJO teleconnection patterns in GCMs with a zonally extended subtropical jet such as that observed during El Niño (e.g. Figure 3.2). In addition, the La Niña NLBM run suggests that the Pacific geopotential height anomalies (Figure 3.7) are not caused by the significant suppression of blocking (Figure 3.11b, top row) since blocking is not simulated in this simple model. However, it is possible that the blocking anomalies amplify the geopotential height anomalies.

Over northeast North America, both NLBM runs develop an anticyclonic anomaly, in agreement with Figures 3.6 – 3.7. In the El Niño run (Figure 3.16, top panel), a cyclonic anomaly develops over the Atlantic and an anticyclonic anomaly over Europe, a pattern also observed in the pentads following MJO phase 3 (Figure 3.6). Unlike the El Niño run, the La Niña MJO wave train pathway is towards the southeast (Figure 3.15, bottom panel). This pattern is also evident in the early pentads following MJO phase 3 (Figure 3.7). However, the NLBM strengthens the Atlantic cyclonic anomaly (Figure 3.16, bottom) whereas the composite does not (Figure 3.7). It is possible that the cyclonic anomaly is suppressed by internal variability or an external forcing outside of the MJO, which would not be captured by the NLBM. The role of the MJO on the suppression of Atlantic blocking that follows phase 3 during La Niña is not clear based on the NLBM. As previously discussed, the NAO pattern associated with the La Niña phase 3 suppression of blocking is only observed when considering the combined impact of the MJO and ENSO (Figure 3.12), suggesting that a more complex model that allows both forms of variability to evolve and interact is likely necessary to understand the Atlantic blocking signal.

3.6.3 NLBM experiments: Phase 7 El Niño pattern

The role of MJO Rossby waves in producing the MJO phase 7 El Niño Atlantic dipole (Figure 3.8) is examined using a propagating heat source beginning with MJO phase 4 in conjunction with the El Niño basic state. Since the significant Atlantic cyclonic anomaly is observed during MJO phase 7, pentad 0 (Figure 3.8; top row), we show the NLBM response prior to (Figure 3.17, top panel), during (middle panel), and following (bottom panel) MJO phase 7. The cyclonic anomaly over northeast North America develops prior to MJO phase 7 (top panel) and grows during MJO phase 7 with an anticyclonic anomaly to its north (middle panel). Whereas Figure 3.7 demonstrates that the dipole anomaly persists, the dipole does not persist in the NLBM. It is not surprising that a persistent anomaly pattern characteristic of a block does not develop since the NLBM does not resolve eddy-mean flow interactions. In the NLBM, the cyclonic anomaly propagates eastward (bottom panel) and the anticyclonic anomaly dissipates. Figure 3.17 suggests that MJO Rossby waves can develop an Atlantic dipole anomaly such as that observed in Figure 3.8 that can act as the initial impetus for blocking anomalies. However, without eddy-mean flow interactions the dipole is not maintained.

The NLBM is able to capture many of the basic features of interest in this section. However, a caveat is that the NLBM is sensitive to the initial MJO phase of the propagating heat source used in the experiments. While some of this sensitivity is likely due to the large-scale impact of previous MJO phases (e.g. Figure 3.15), some of this sensitivity may be due to the simplicity of the NLBM. It would be interesting to conduct similar experiments using a more complex model, although this will be left for future research.

3.7 Summary and Discussion

The influence of MJO teleconnections during ENSO events on high-latitude blocking is examined, expanding on the results discussed in H16. Results demonstrate that during El Niño, MJO Pacific teleconnection patterns are shifted east relative to La Niña. During MJO phase 3, the Pacific teleconnection patterns associated with the MJO and El Niño are largely destructive, producing little impact on high-latitude blocking. Conversely, during La Niña the MJO phase 3 Pacific teleconnection pattern anomalies are largely constructive, and blocking is significantly suppressed throughout the North Pacific. Experiments using the NLBM demonstrate that the phase 3 La Niña teleconnection pattern is largely explained by MJO heating and the La Niña basic state, suggesting that the geopotential height anomalies during phase 3 are not a result of the significant suppression of blocking but rather Rossby wave teleconnections caused by the MJO. However, the blocking anomalies may amplify the geopotential height anomalies. Unlike the phase 7 La Niña teleconnection patterns, the MJO phase 7 Pacific teleconnections during El Niño add constructively to the El Niño teleconnection pattern and is associated with a significant and persistent increase in high-latitude blocking. During La Niña, the phase 7 Pacific teleconnection pattern does not destructively interfere with the La Niña teleconnection pattern, but it produces a pattern not favorable for Pacific high-latitude blocking.

The El Niño MJO phase 7 teleconnection pattern is associated with a significant and persistent increase in Atlantic blocking, with local blocking frequencies reaching triple that of the DJF El Niño mean. Atlantic phase 7 blocking frequency anomalies are not significant during neutral ENSO, suggesting that the significant increase during El Niño largely accounts for the near doubling in blocking frequency discussed in H16. Results using an NLBM indicate that

MJO Rossby waves provide the initial dipole anomaly observed during MJO phase 7. The blocking pattern is then likely maintained by transient eddy activity.

The investigations in this study are limited by the sample sizes of each MJO and ENSO phase, which is taken into account using significance testing and by the use of the NLBM. However, caution is necessary when comparing the amplitude of the composites due to differences in MJO phase sample size between ENSO phases. Future work includes examining the results discussed here using long-term GCM simulations, which diminish the impact of sample size limitations. In addition to the impact of ENSO on MJO teleconnections, which is the primary focus here, the MJO can influence ENSO teleconnections. For example, Hoell et al. (2014) found that MJO activity can amplify or weaken the magnitude of the ENSO teleconnection patterns by altering ENSO precipitation. This, in turn, can impact atmospheric blocking frequency and compels further investigation. In addition, MJO teleconnections during ENSO events may influence mid-latitude blocking over the East Pacific and Europe. These regions have a lower frequency of blocking in the mean relative to the high-latitudes (e.g. H16), and are not discussed here due to sample size limitations. However, these regions could be examined using a GCM.

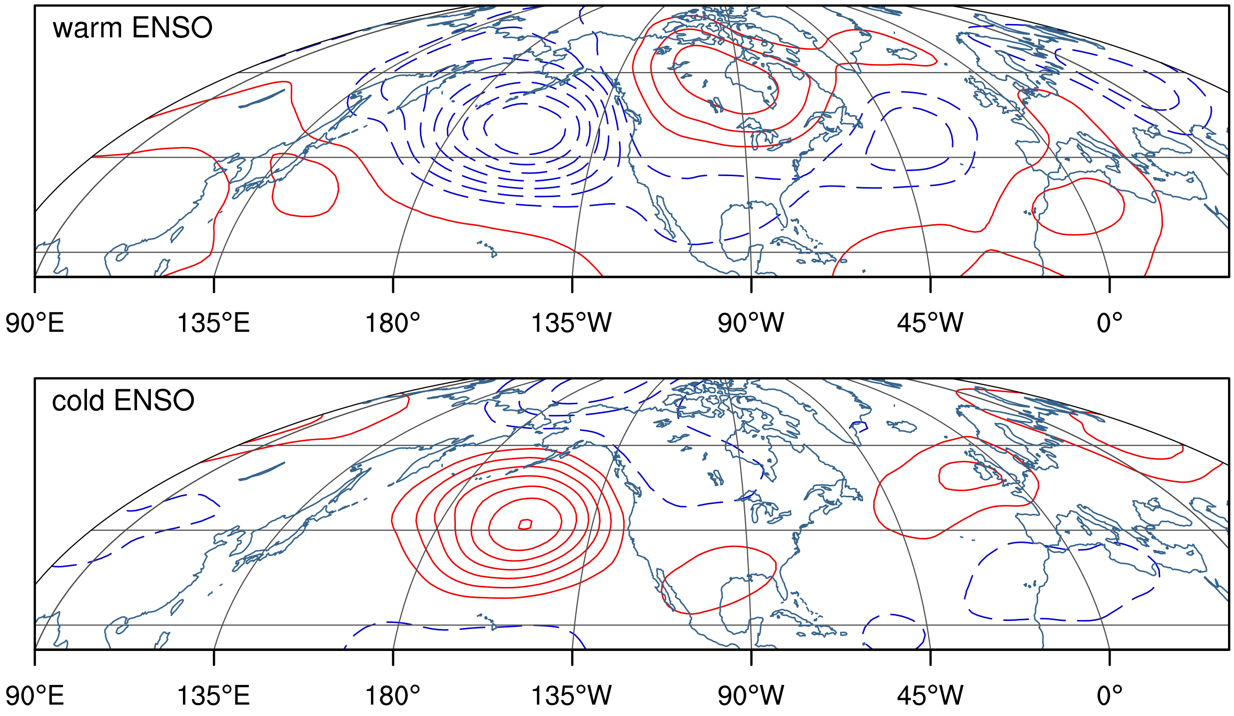

FIG. 3.1. DJF 500-hPa geopotential height anomalies for warm (top) and cold (bottom) ENSO. Positive values are in solid red contours; negative contours are blue and dashed. Contours are every 10 m, and the zero contour is omitted. Anomalies are computed by removing the first three harmonics of the seasonal cycle. Latitude grid lines are every 20° for all figures unless specifically mentioned.

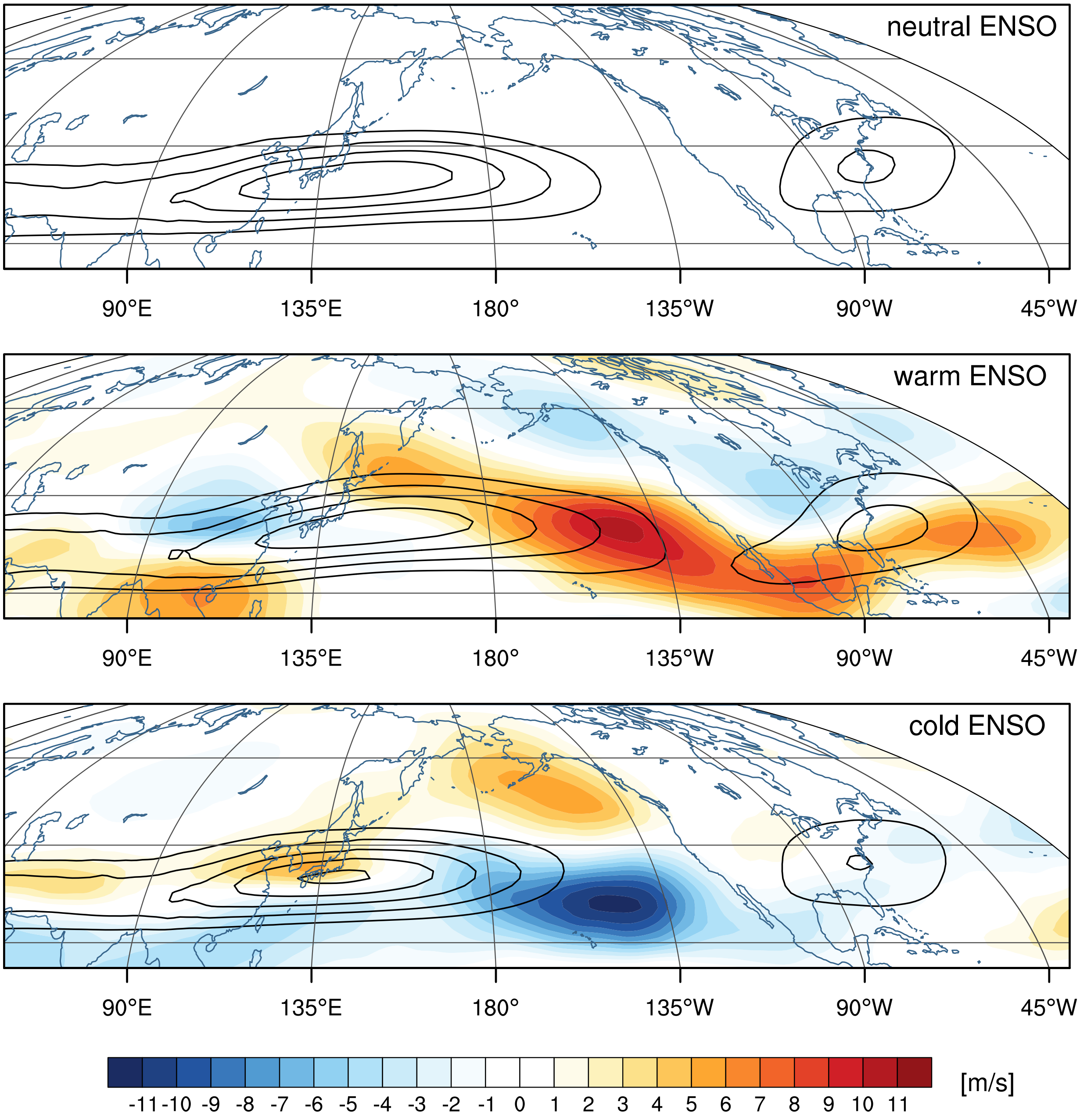

FIG. 3.2. Mean DJF 200-hPa zonal wind (contours) for neutral (top), warm (middle), and cold (bottom) ENSO conditions. Contours are every 10 m/s beginning at 35 m/s. Color shading is the mean zonal wind difference between the corresponding ENSO phase and the neutral ENSO phase.

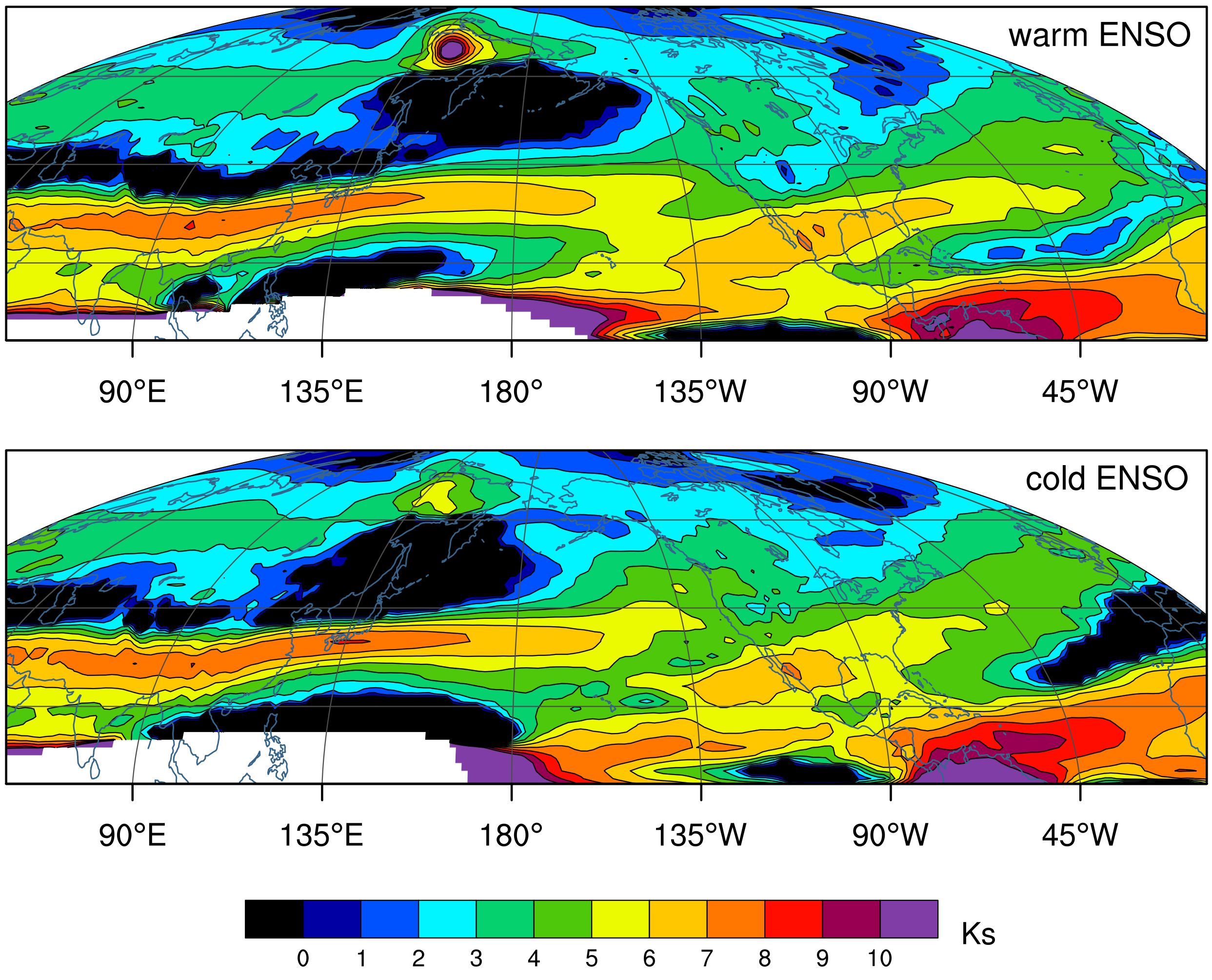

FIG. 3.3. Stationary zonal wavenumber (K_s) derived from the DJF 200-hPa Mercator zonal wind for warm (top) and cold (bottom) ENSO conditions. Regions of easterly winds ($\bar{u}_M < 0$) are in white, and areas where $\beta_M < 0$ are in black.

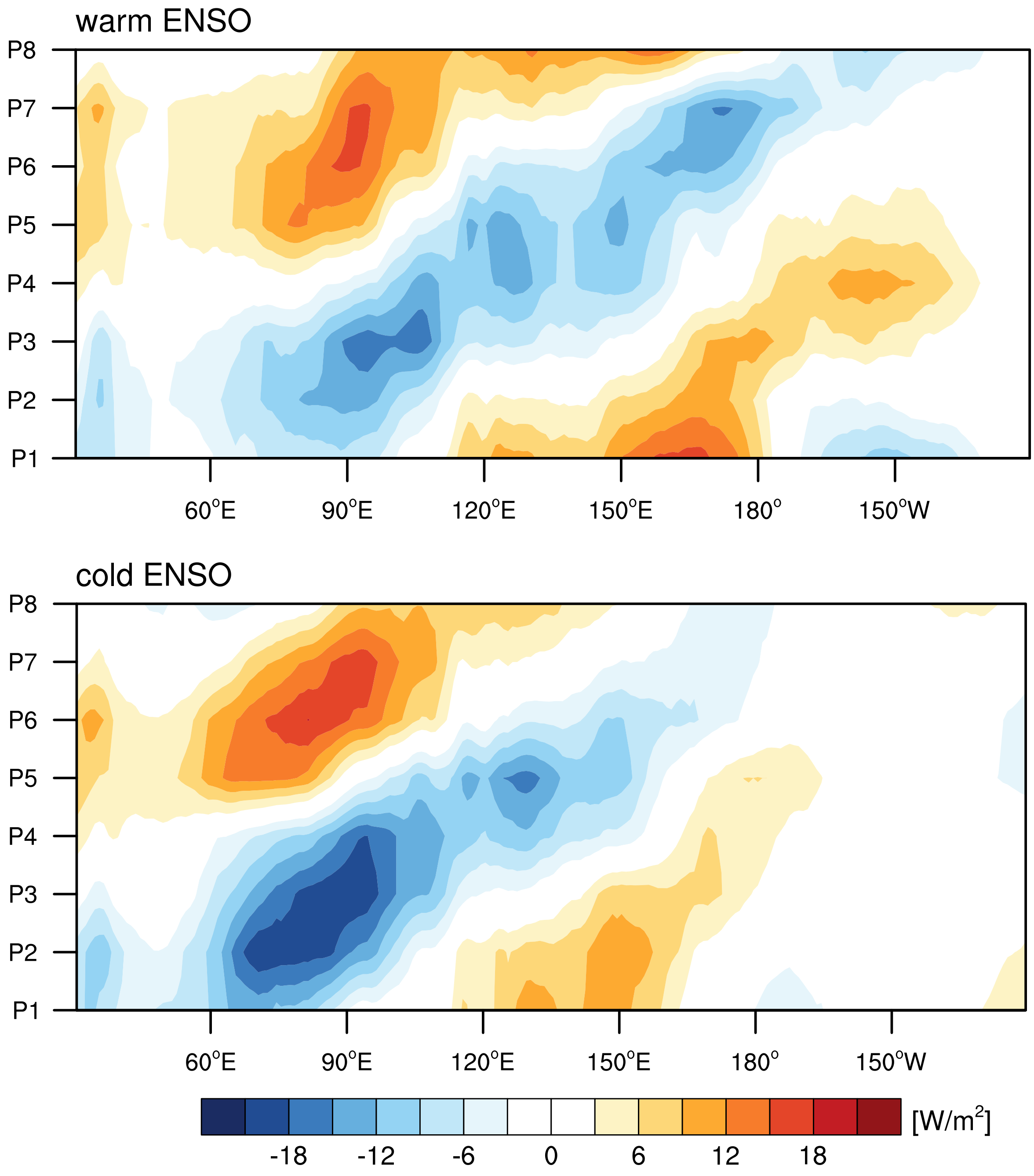

FIG. 3.4. MJO phase – longitude diagram of 30 – 70 day band filtered OLR averaged from 10°S – 10°N during warm (top panel) and cold (bottom panel) ENSO phases. MJO phase is along the y-axis, where P1 indicates MJO phase 1 and so on.

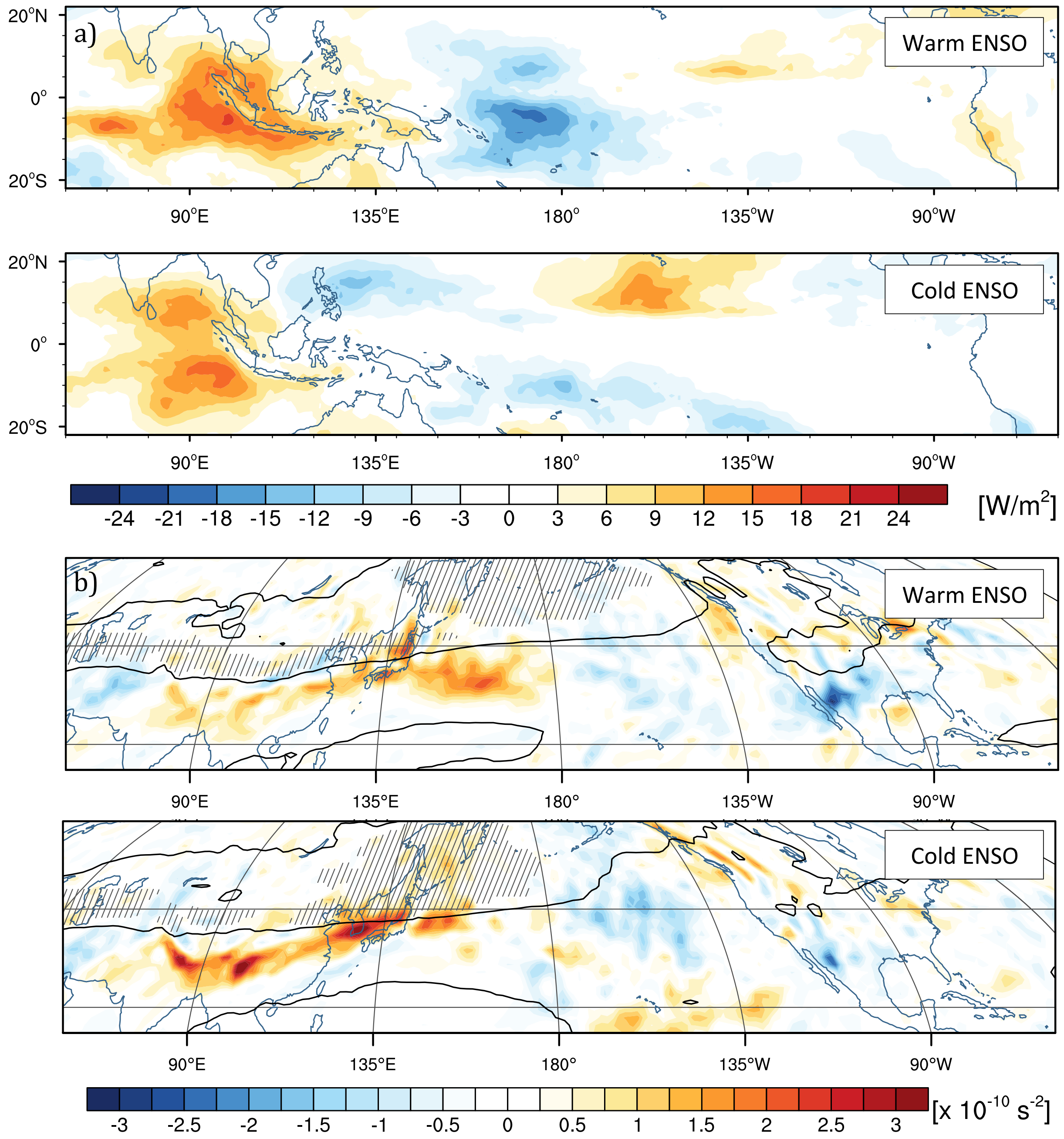

FIG. 3.5. MJO phase 7 pentad composites of 30 – 70 day filtered a) OLR during warm (top) and cold (bottom) ENSO, and b) Rossby wave source (RWS; color shading) during warm (top) and cold (bottom) ENSO. In b), the $K_s = 3$ contour line from Figure 3.3 is overlaid and the $\beta_M < 0$ regions are hatched north of 25°N.

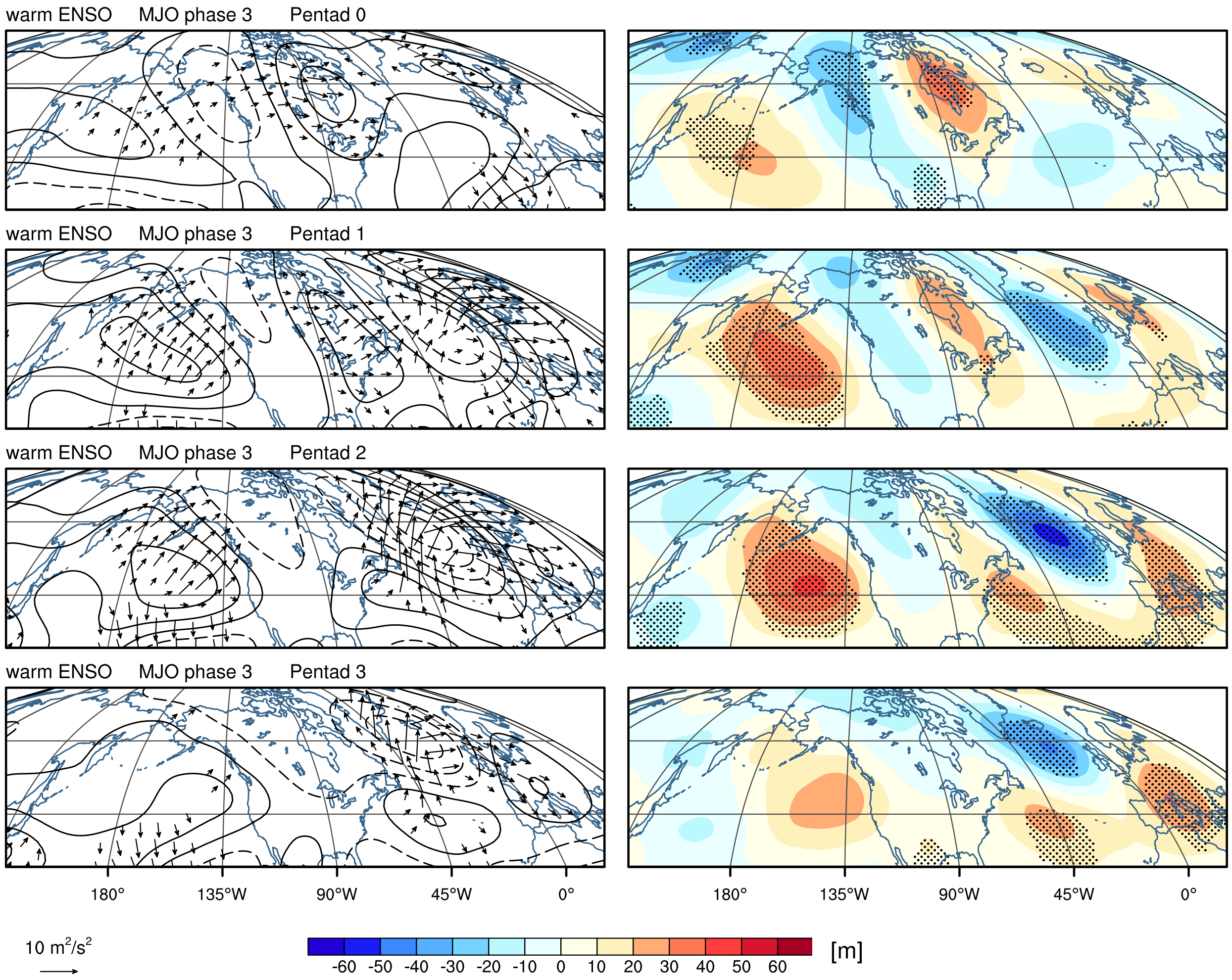

Fig. 3.6. Warm ENSO MJO Phase 3 composites of 30 – 70 day filtered 200-hPa streamfunction (left column) and 500-hPa geopotential height (right column) for pentad 0 (top row) to pentad 3 (bottom row), where a pentad is a 5-day mean. Black dotting demonstrates the anomalies found to be 95% significantly different from zero. Positive (negative) streamfunction is in solid (dashed) contours with an interval of 15×10^5 m/s^2, and the zero contour is omitted. Overlaid on streamfunction are wave activity flux vectors. Vectors with a magnitude below 2 m^2/s^2 are omitted. The reference vector is provided below the left column.

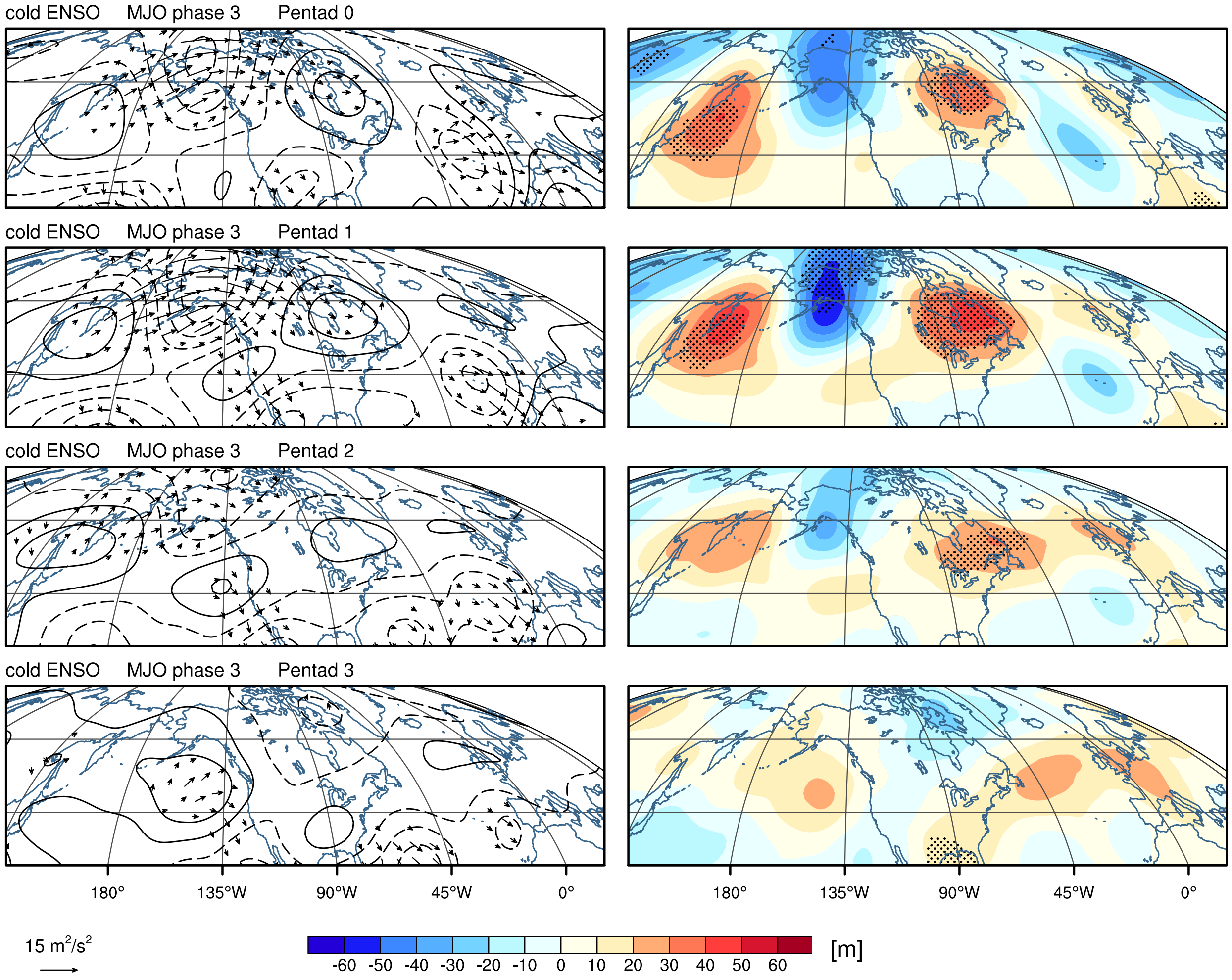

FIG. 3.7. Same as Figure 3.6, but for cold ENSO conditions.

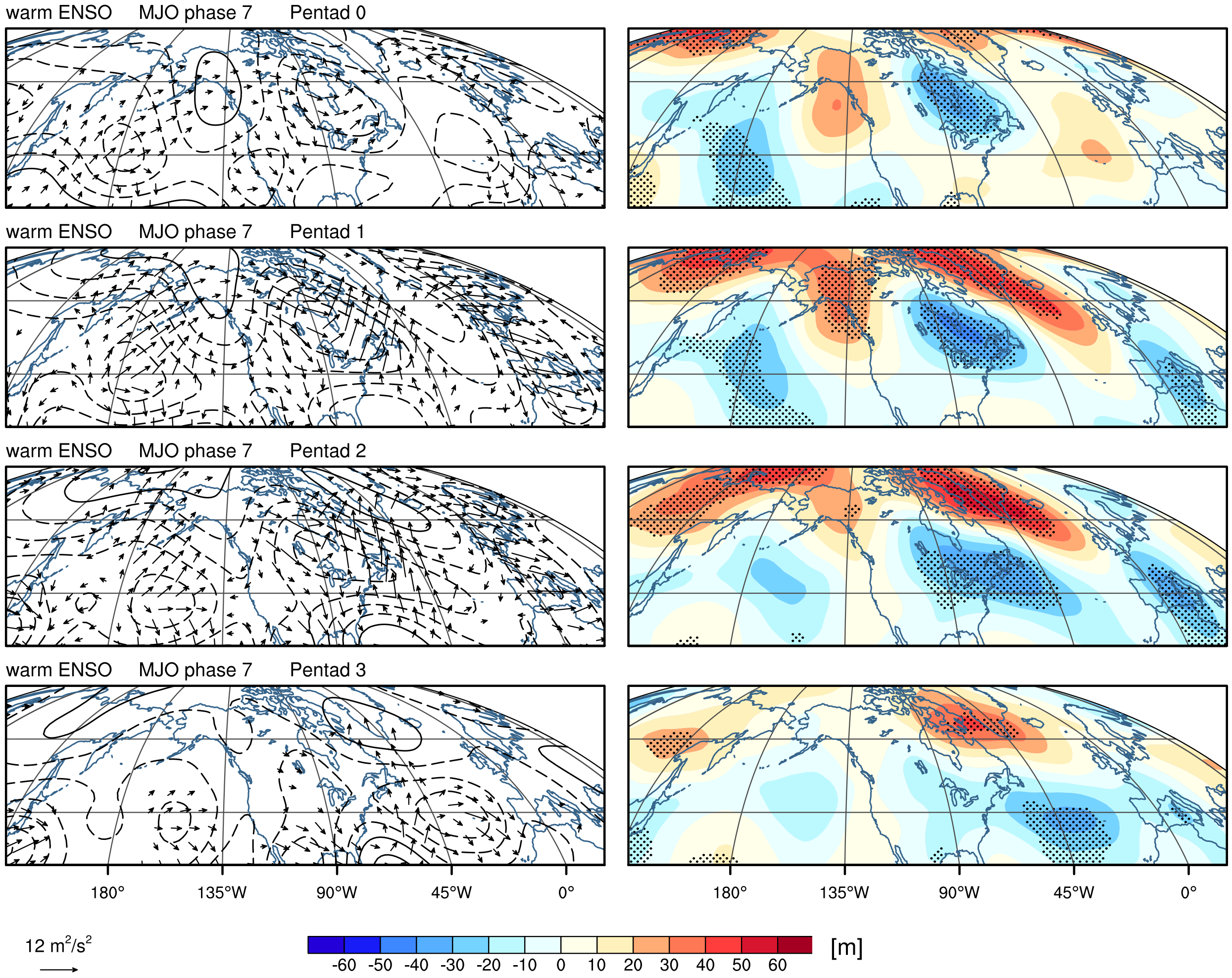

FIG. 3.8. Same as Figure 3.6, but for MJO phase 7.

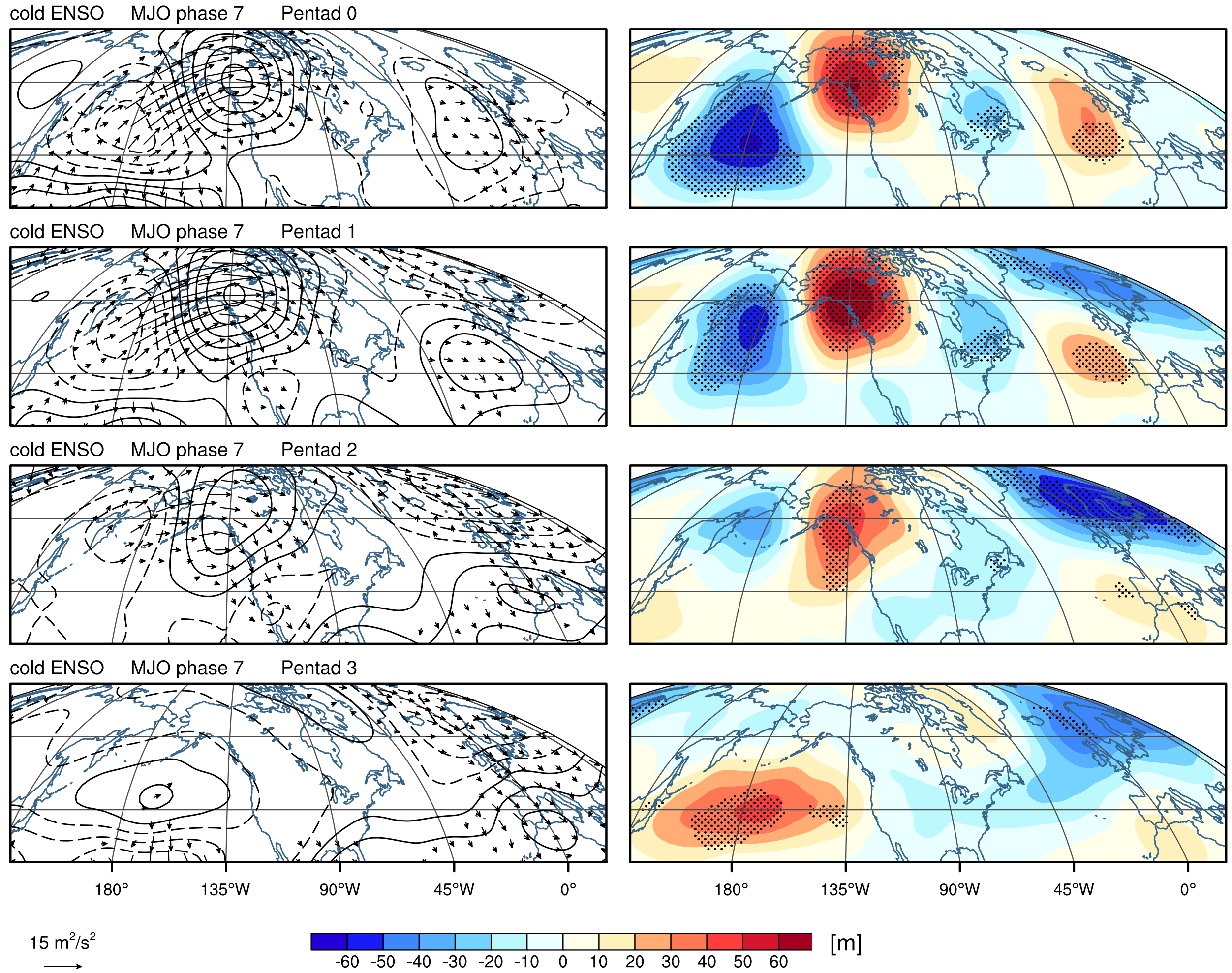

FIG. 3.9. Same as Figure 3.6, but for MJO phase 7 during cold ENSO conditions.

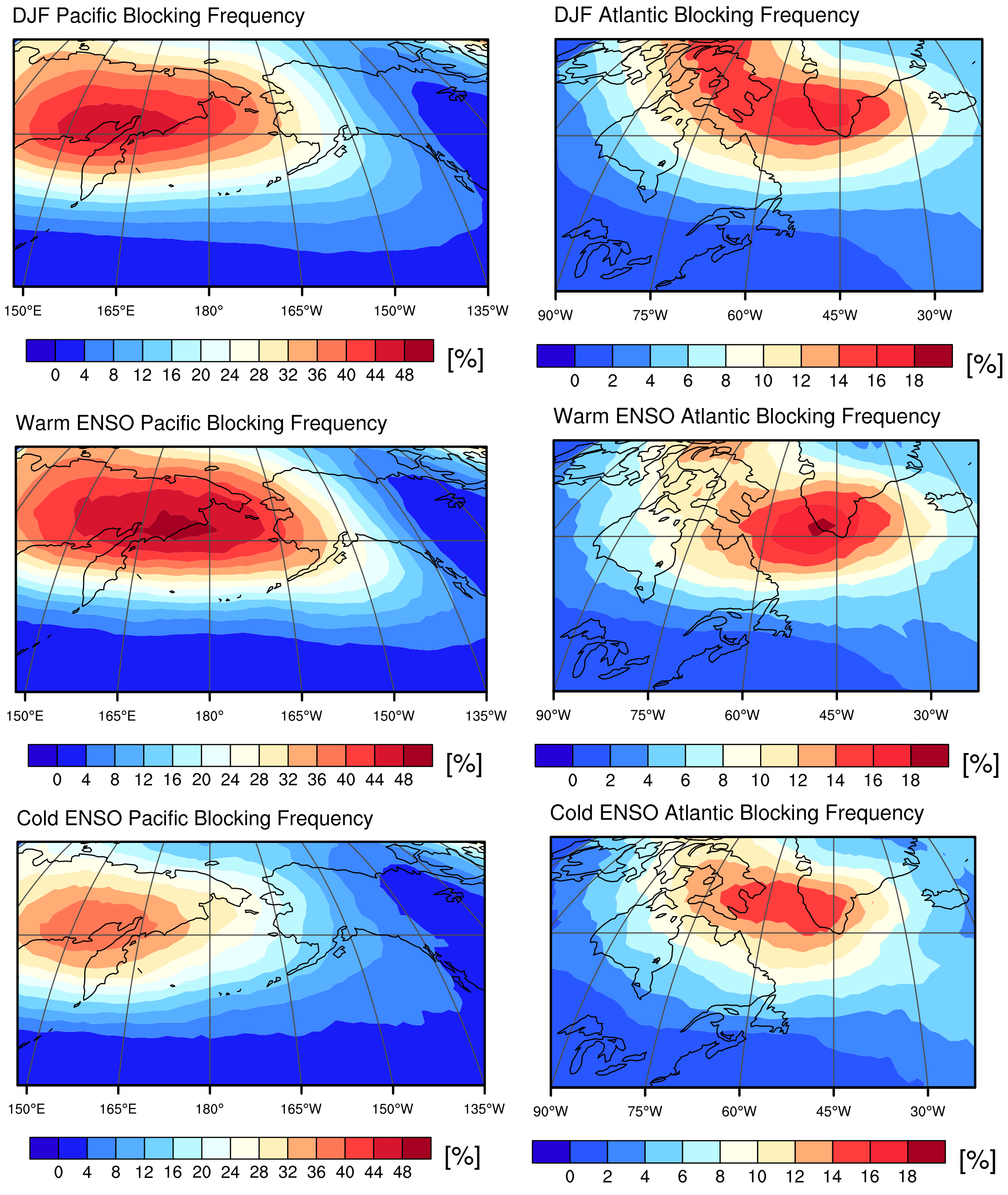

DJF Pacific Blocking Frequency

DJF Atlantic Blocking Frequency

Warm ENSO Pacific Blocking Frequency

Warm ENSO Atlantic Blocking Frequency

Cold ENSO Pacific Blocking Frequency

Cold ENSO Atlantic Blocking Frequency

FIG. 3.10. Mean blocking frequency for the Pacific (left column) and Atlantic (right column) regions based on all DJF seasons (top row), warm ENSO DJF seasons (middle row) and cold ENSO DJF seasons (bottom row).

a) Warm ENSO

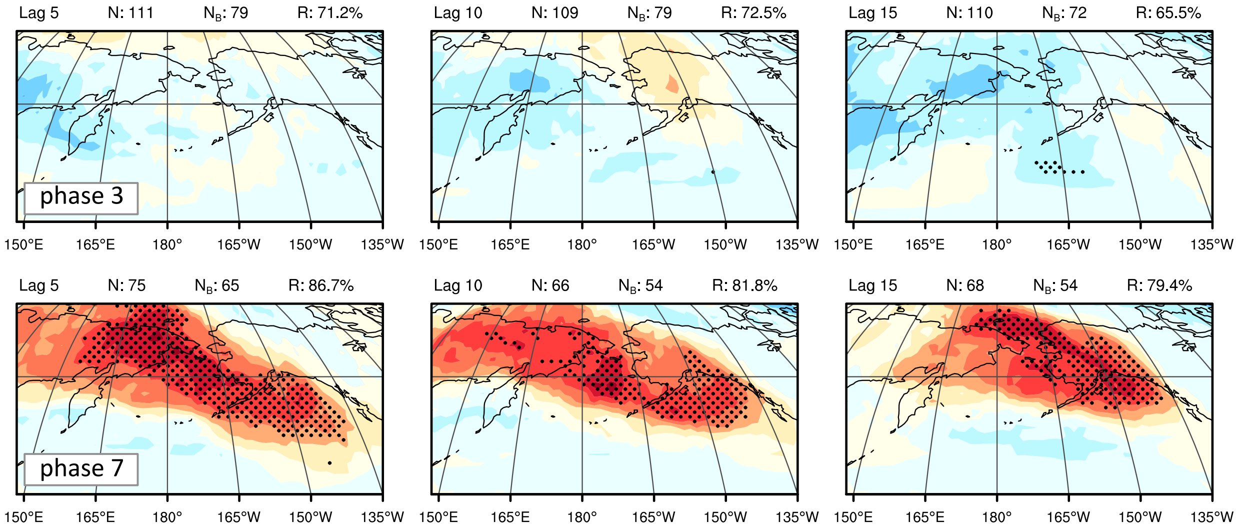

b) Cold ENSO

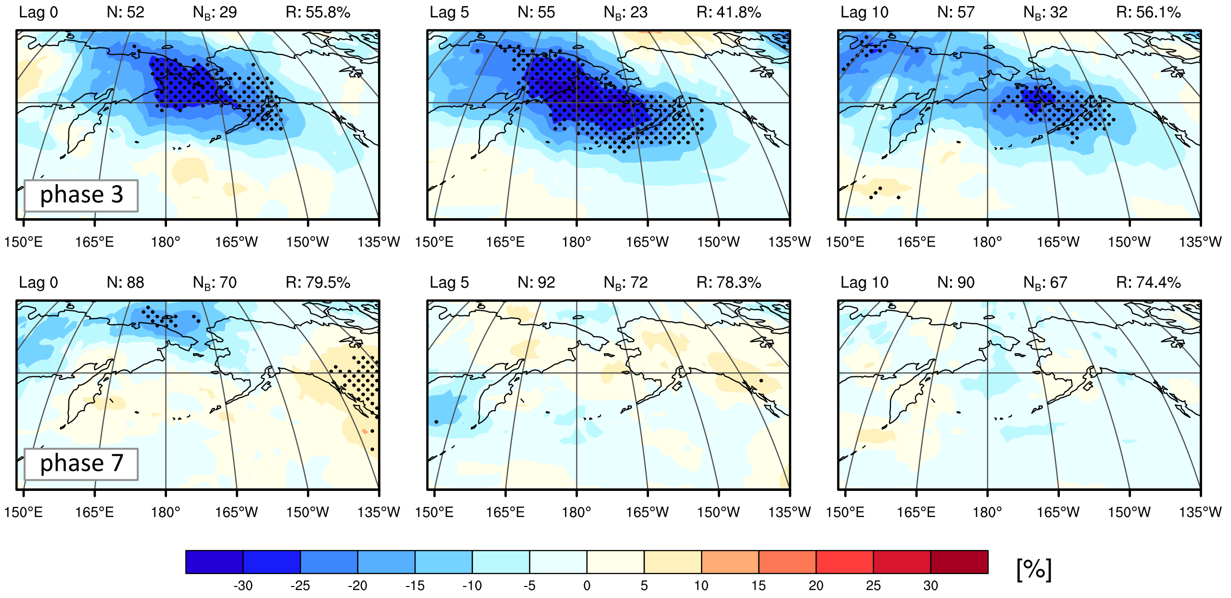

FIG. 3.11. Pacific blocking frequency anomalies during a) warm and b) cold ENSO conditions. Panel a) shows frequency anomalies 5 (left column), 10 (middle column), and 15 (right column) days after MJO phase 3 (top row) and phase 7 (bottom row). Panel b) shows anomalies at lags 0, 5, and 10 relative to the MJO phase 3 (top row) and 7 (bottom row). Anomalies are a deviation from the DJF mean (Figure 3.10; top row). Black dotting indicates anomalies found to be 95% significantly different from zero. For explanation of the values above each panel, see Section 3.5.

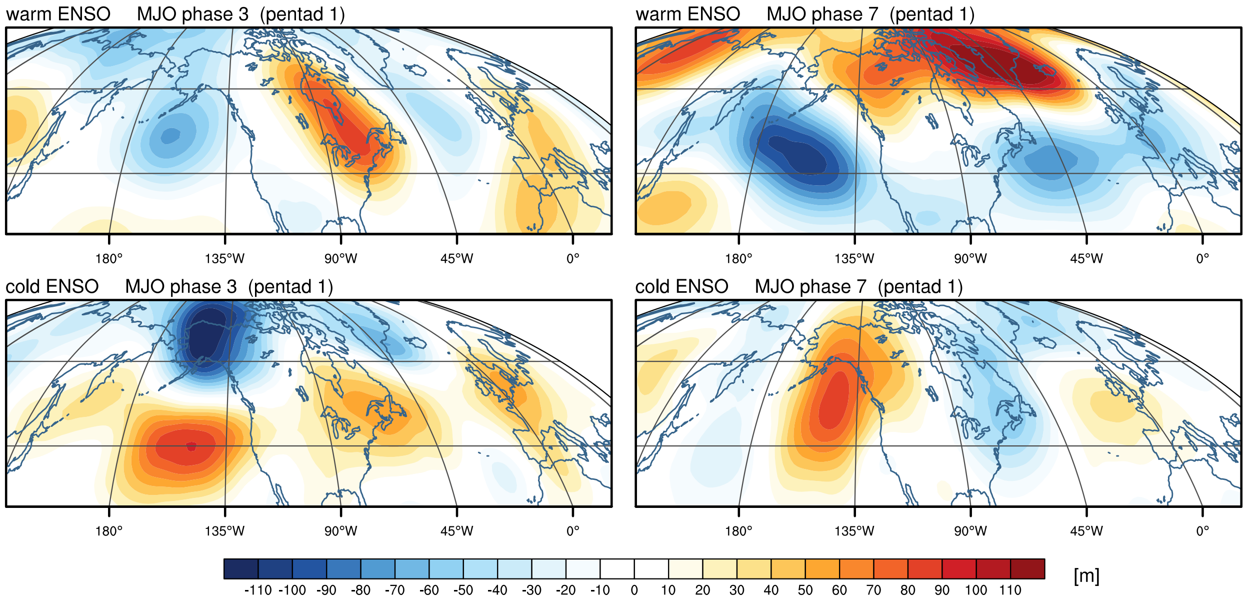

FIG. 3.12. MJO Phase 3 (left column) and phase 7 (right column) pentad 1 composites of unfiltered 500-hPa geopotential height anomalies during warm (top row) and cold (bottom row) ENSO conditions.

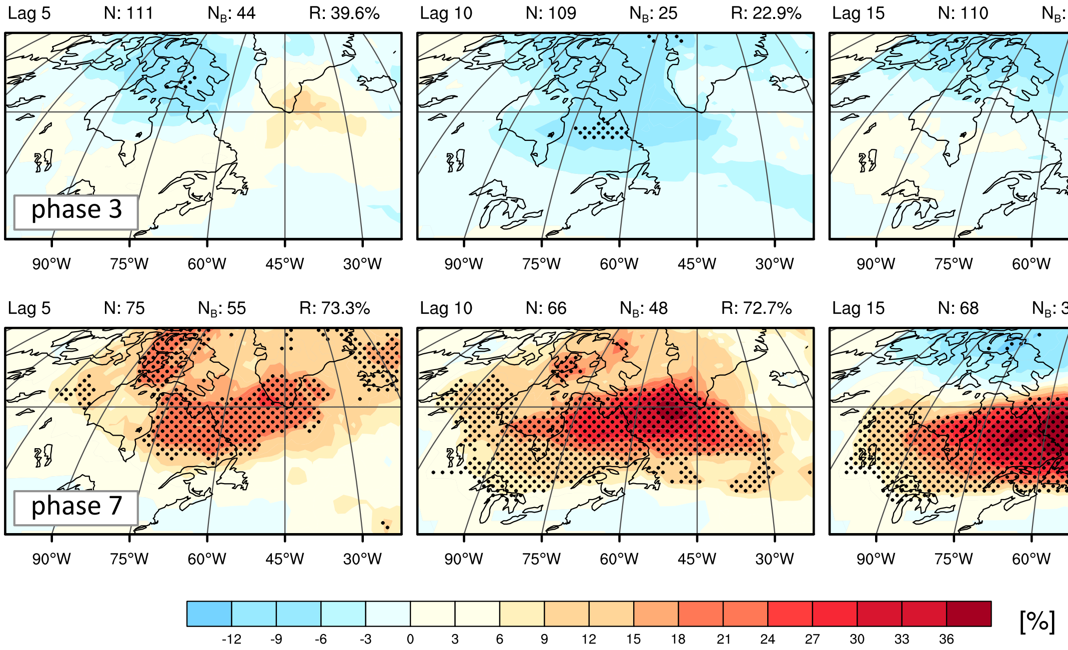

a) Warm ENSO

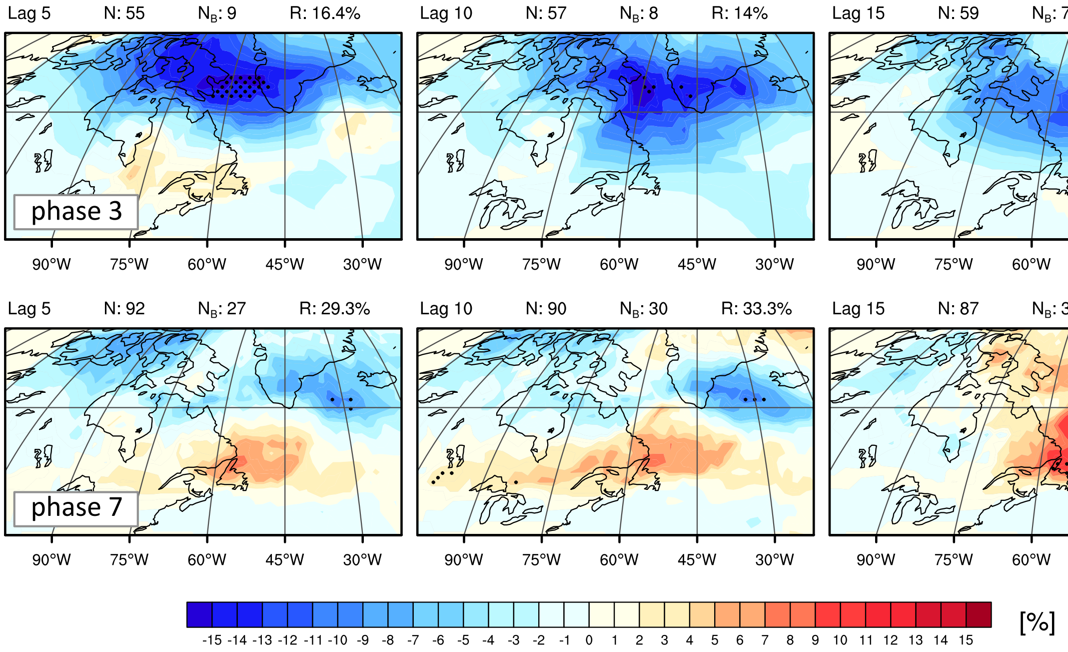

b) Cold ENSO

FIG. 3.13. Atlantic blocking frequency anomalies relative to the DJF mean during a) warm and b) cold ENSO conditions 5 (left), 10 (middle), and 15 (right) days after MJO phase 3 (top row) and phase 7 (bottom row). Black dotting indicates anomalies found to be 95% significantly different from zero. For explanation of the values above each panel, see Section 3.5.

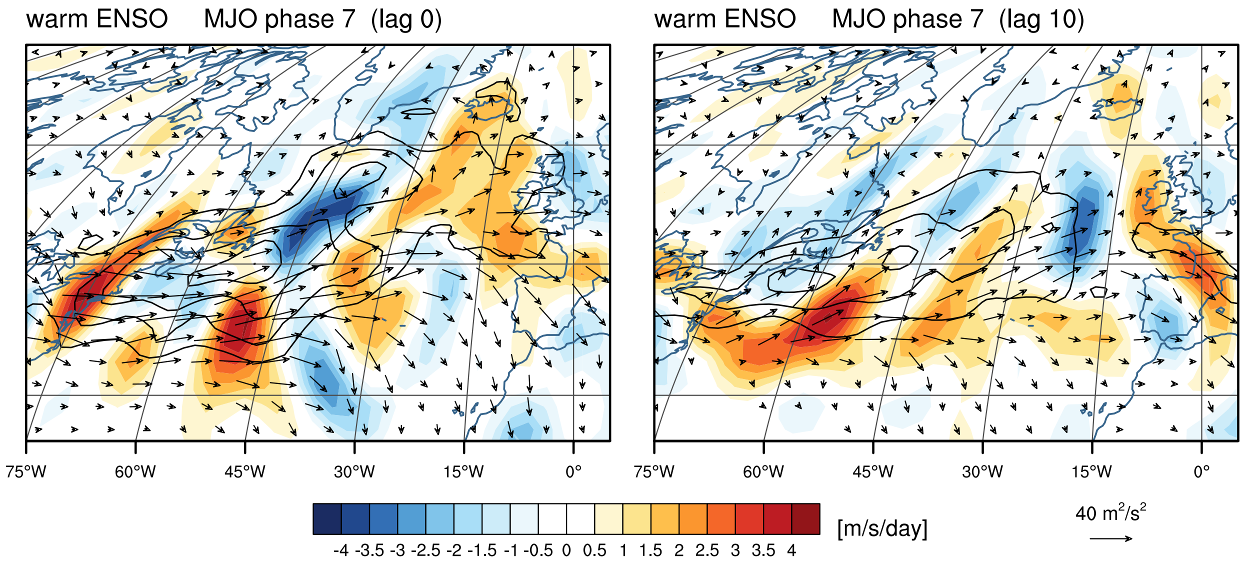

FIG. 3.14. Warm ENSO composites of 300-hPa mean transient eddy kinetic energy (TEKE; contours), **E**-vectors, and **E**-vector divergence (color shading) during (left panel; lag 0) and 10 days (right panel) after MJO phase 7. TEKE contour interval is 20 m^2/s^2 beginning at 90 m^2/s^2. **E**-vectors of magnitude less than 5 m^2/s^2 are omitted. Latitude grid lines are every 15°.

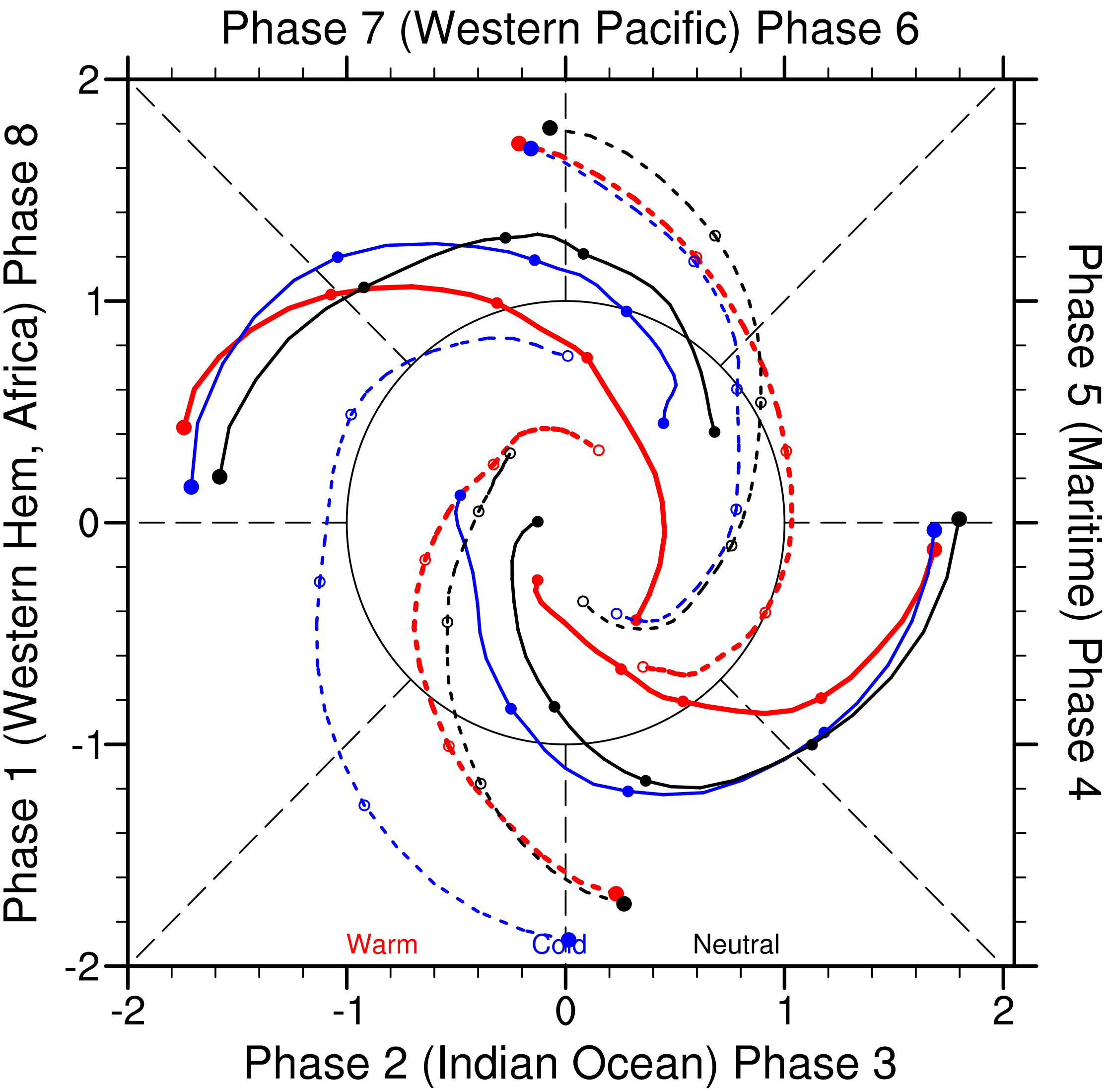

FIG. 3.15. RMM index amplitude backward trajectories in phase-space during the warm (red line), cold (blue line) and neutral (black line) ENSO phases. Trajectories initiate in each quadrant when the ENSO phase RMM index indicates a strong amplitude MJO event (> 1.3) in phases 2 – 3 (bottom), phases 4 – 5 (right), phases 6 – 7 (top), and phases 8 or 1 (left). Each trajectory is shown for 26 days (25 days prior to initiation). Circles mark every five days. The composite indices are smoothed using a 5-point running mean prior to plotting (e.g. Rashid et al. 2011).

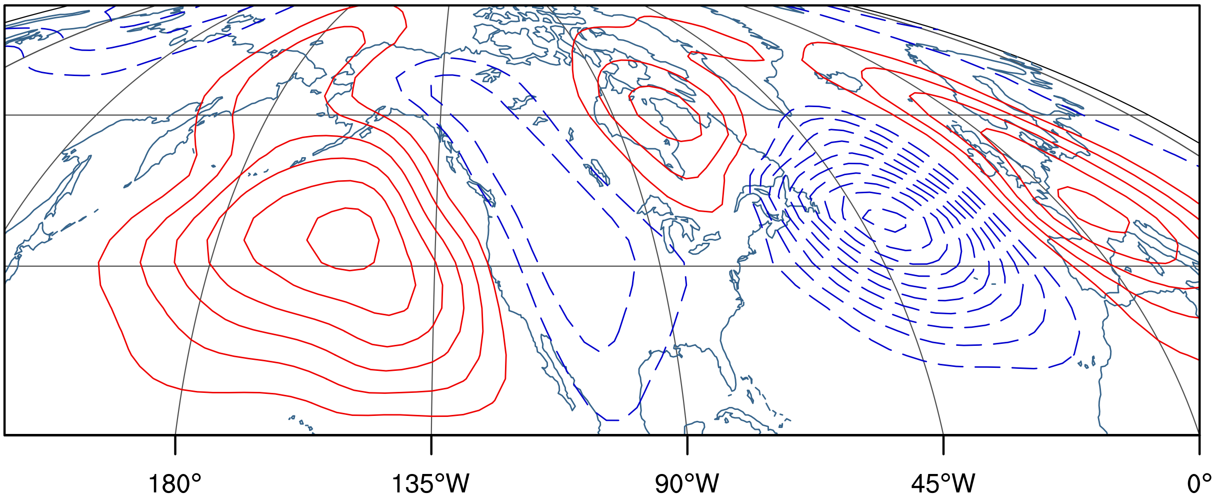
warm ENSO MJO response at days 21 to 26

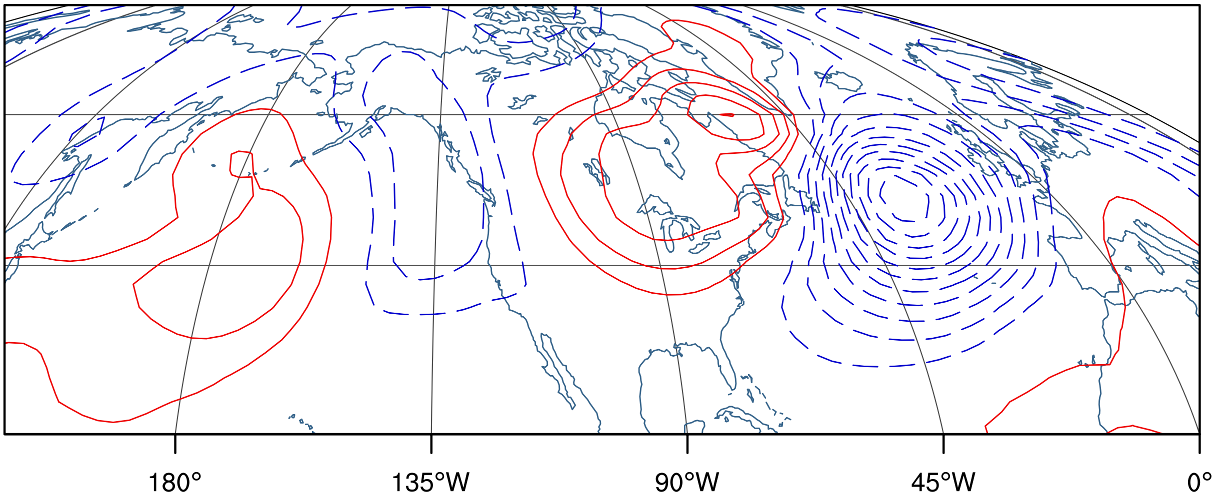
cold ENSO MJO response at days 25 to 30

FIG. 3.16. NLBM 500-hPa geopotential height anomaly response against the warm (top) and cold (bottom) ENSO basic state. The warm ENSO run (top) is the average 21 – 26 day response to a propagating heat source initiated with MJO phase 2 heating, and corresponds to 14 – 19 days after MJO phase 3 begins. The cold ENSO run (bottom) is the average 25 – 30 day response to a propagating heat source initiated with MJO phase 8 heating and corresponds to 7 – 12 days after MJO phase 3 begins. See text for further details regarding the propagating heat source used. Contours are every 5 m and the zero contour is omitted.

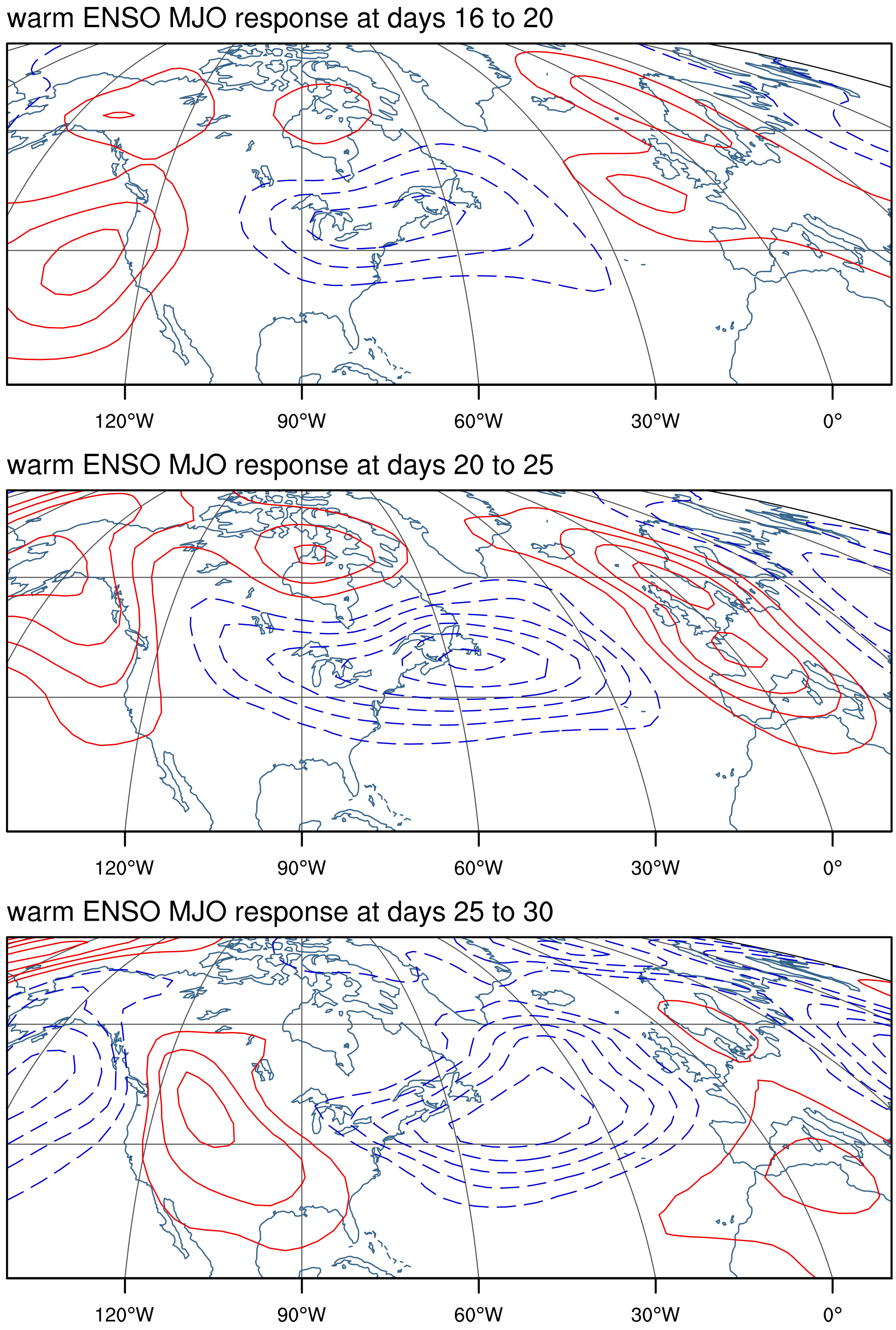

FIG. 3.17. NLBM 500-hPa geopotential height anomaly response against the warm ENSO basic state. Shown is the average 16 – 20 (top), 20 – 25 (middle), and 25 – 30 (bottom) day response to a propagating heat source initiated with MJO phase 4. The averages approximately coincide with the days prior to (top), during (middle), and after (bottom) MJO phase 7, where phase 7 of the propagating heat source begins on day 22. See text for further details regarding the propagating heat source used. Contours are every 5 m and the zero contour is omitted.

CHAPTER 4: MADDEN – JULIAN OSCILLATION PACIFIC TELECONNECTIONS: THE IMPACT OF THE BASIC STATE AND MJO REPRESENTATION IN GENERAL CIRCULATION MODELS

4.1 Introduction

The importance of the Madden-Julian Oscillation (MJO) to the global circulation has been widely investigated since its first detection in the early 1970s (Madden and Julian, 1971, 1972). The MJO is an intraseasonal tropical convectively coupled disturbance that propagates eastward from the West Indian Ocean to the Central Pacific Ocean over a period of approximately 30 – 90 days. During an MJO event, anomalous convection acts as a tropical heat source emitting stationary Rossby waves that propagate into the extratropics and significantly modulate the extratropical circulation (e.g. Matthews et al. 2004; Seo and Son 2012). The MJO modulates various aspects of weather and climate including regional temperatures (e.g. Vecchi and Bond 2004), precipitation (e.g. Jones et al. 2004; Donald et al. 2006), atmospheric blocking (e.g. Henderson et al. 2016), hurricanes (e.g. Maloney and Hartmann 2000; Liebmann et al. 1994), and global monsoons (Lorenz and Hartmann, 2006; Lau and Waliser 2012), as well as important modes of climate variability such as the North Atlantic Oscillation (NAO; e.g. Cassou 2008; Lin et al. 2009) and the Pacific-North American pattern (PNA; e.g. Mori and Watanabe 2008; Riddle et al. 2013). The widespread influence of the MJO implies that accurate prediction of global circulation patterns and weather events require consideration of MJO activity and its accurate simulation in climate and weather forecasting models.

Although its global influence is substantial, the MJO has been difficult to properly simulate in General Circulation Models (GCMs; e.g. Kim et al. 2009; 2011; Hung et al. 2013). The overall representation of the MJO in GCMs has been improved since phase 3 of the Coupled Model Intercomparison Project (CMIP3), the international collaboration of GCMs that played a key role in the Fourth Assessment Report (AR4) of the Intergovernmental Panel on Climate Change (IPCC). In particular, model improvements for the 5th phase of the CMIP project (CMIP5) have led to improved MJO spectral characteristics in equatorial precipitation and zonal wind, and increased MJO variance. However, many state-of-the-art GCMs still exhibit severe deficiencies in simulating the MJO, including unrealistically short MJO persistence and poor or non-existent eastward propagation of MJO convection (e.g. Ahn et al. 2017; Jiang et al. 2015; Kim et al. 2014; Hung et al. 2013).

Errors in MJO simulations can introduce systematic errors in extratropical circulations. Previous studies have shown that tropical thermal forcing, such as that associated with anomalous MJO convection, is balanced by ascending motion and divergent winds aloft. This upper tropospheric divergent flow generates upper-level anticyclonic anomalies that can produce stationary Rossby waves that extend into higher latitudes (e.g. Hoskins and Karoly 1981). The location and amplitude of the Rossby waves is dependent on the location, amplitude, and structure of the heat source (e.g. Hoskins and Karoly 1981; Jin and Hoskins 1995; Yasui and Watanabe 2010). This suggests that errors in MJO simulations can influence the nature of Rossby waves emitted by MJO heating and the associated circulation anomalies that impact the extratropics. Model MJO teleconnections are further complicated by the accuracy of the model basic state. The background flow determines the direction and propagation characteristics of MJO-induced Rossby waves (e.g. Hoskins and Ambrizzi 1993; Ting and Sardeshmukh 1993).

However, a key issue is that improvements in the representation of the MJO in GCMs often negatively impact the basic state (Kim et al. 2011). All else being equal, modelers may prefer a realistic basic state rather than a more realistic MJO when deciding on the suite of parameterizations to use in their climate models. This problem may explain why little focus has been given to MJO teleconnections in GCMs, which require an accurate representation of both the mean state and MJO.

Recent studies have demonstrated that the ability of GCMs to reproduce teleconnection patterns associated with tropical variability depends on both the model basic state (e.g. Dawson et al. 2011) and the quality of the heating (e.g. Yoo et al. 2015). For example, improvements to the basic state due to increased resolution have been shown to improve the accuracy of the teleconnection patterns associated with the El Niño-Southern Oscillation (ENSO) in the HiGEM1.2 model (Dawson et al. 2011). Weare (2013) noted that the teleconnection patterns associated with ENSO warm events are influenced by the quality of upper tropospheric flow anomalies associated with ENSO heating and the length and frequency of ENSO events. By examining the influence of convection schemes on the model MJO and associated Rossby wave pathways in the Community Atmosphere Model version 5 (CAM5), Yoo et al. (2015) found that using a unified convection scheme rather than the default deep and shallow convection schemes resulted in improved MJO characteristics and more realistic MJO teleconnection patterns. Furthermore, the study noted that little is known about the behavior of MJO teleconnections in GCMs.

Given the significant impact of the MJO on the extratropical circulation, it is important to quantify how model MJO and basic state errors impact the MJO teleconnection patterns in GCMs. This exercise may provide insight into possible causes of simulation errors in extratropical weather and climate that are known to be significantly modulated by the MJO. In climate change studies, MJO teleconnection errors may introduce uncertainties in future projections of extreme weather events and climate patterns that are significantly modulated by the MJO. Hence, it is important that modelers and climate scientists are aware of these errors and the reasons for them.

This study examines the MJO teleconnection patterns of 10 CMIP5 models with a focus on the role of the model MJO and basic state quality on MJO teleconnection patterns. The CMIP5 models and reference datasets are described in Section 4.2, as well as a description of the general methodology of the study. Section 4.3 investigates the ability of the CMIP5 models to correctly simulate the MJO, basic state, and the MJO teleconnection patterns. In Section 4.4, a linear baroclinic model (LBM) is employed to analyze the individual impacts of the model MJO and basic state performance on the quality of MJO teleconnection patterns. Lastly, summary and conclusions are provided in Section 4.5.

4.2 Methodology

4.2.1 Model and Observational Data

The 10 CMIP5 models examined are listed in Table 4.1. The GCMs selected for this study have varying degrees of MJO quality and basic state performance, useful for the purposes of this study. As a side note, additional CMIP5 model data were unavailable at the time of our investigations due to problems with the CMIP5 website. The analysis performed here was therefore not extended beyond the 10 models initially chosen for this study. Model output is taken from the first ensemble member of the CMIP5 historical runs, which use the observed evolution of forcing for the 20th Century (e.g. Taylor et al. 2012; Weare 2013). Unless otherwise stated, boreal winter (December – February; DJF) monthly and daily model output is analyzed for December 1950 – February 2005, for a total of 54 boreal winter seasons, with the exception of GFDL-CM3, which only spans to 2004. The reference dataset used here is the ERA-Interim Reanalysis (Dee et al. 2011). This dataset is provided on a 1.5° x 1.5° grid and spans from December 1979 to February 2014, for a total of 34 winter seasons. Furthermore, daily winter precipitation observations from the Global Precipitation Climatology Project (GPCP; Adler et al. 2003) are used. The GPCP dataset spans from 1996 – 2015 and has a 1° grid spacing.

3.2.2 MJO indices

The eastward evolution of the MJO is represented using the Real-time Multivariate MJO (RMM) indices of Wheeler and Hendon (2004; http://www.bom.gov.au/climate/mjo/). The RMM indices (RMM1 and RMM2) are the first two principal components (PCs) of the combined empirical orthogonal functions (EOFs) of near-equatorial averaged (15°S - 15°N) anomalous outgoing longwave radiation (OLR), 200-hPa and 850-hPa zonal winds. The OLR data used to calculate the RMM indices is derived from NOAA satellite data and the winds from the NCEP/NCAR reanalysis (Wheeler and Hendon 2004). This definition of the MJO has been used in previous studies to examine the MJO teleconnection patterns and their associated extratropical impacts (e.g. Cassou 2008; Lin et al. 2009; Henderson et al. 2016).

In order to examine the model MJO teleconnections during the MJO lifecycle, RMM indices are computed for each model by projecting the model equatorial averaged (15°S to 15°N) OLR, 250-hPa and 850-hPa zonal winds onto the reanalysis EOFs, which were made available by Matthew Wheeler (http://poama.bom.gov.au/project/maproom/RMM/index.htm). Projection onto the reanalysis EOFs allows for a consistent framework for comparison among the different model MJOs, including cases in which a model is not able to properly replicate the MJO EOFs but does contain some MJO-like variability (Waliser et al. 2009). More specifically, the model MJO indices are generated as follows: First, the mean of the previous 120 days is removed from the data to reduce the influence of interannual variability, and the first three harmonics of the seasonal cycle are removed. The three variables are then normalized by the reanalysis tropical standard deviation (based on all longitudes) of each corresponding field, provided by Matthew Wheeler, and projected onto the reanalysis EOFs. The RMM indices for each model are the resulting standardized PCs.

For all datasets, the time evolution of the MJO is represented by 8 phases, where each phase is determined by $\tan^{-1}(\frac{RMM2}{RMM1})$, and provides an approximate longitudinal location of MJO convection. In this definition, MJO phase 1 indicates enhanced MJO convection in the West Indian Ocean, and MJO phase 8 is characterized by enhanced convection in the Central Pacific. Composites relative to MJO phase are only generated when the MJO amplitude, $\sqrt{(\mathrm{RMM1}^2+\mathrm{RMM2}^2)}$, is greater than 1.

4.3 MJO Teleconnections

The amplitude and direction of the stationary Rossby waves generated by tropical heating are dependent on two primary factors: 1) The location, amplitude, and structure of the thermal forcing, and 2) the background flow into which the Rossby waves propagate (e.g. Hoskins and Karoly 1981; Jin and Hoskins 1995). The importance of these factors for producing realistic MJO teleconnections is assessed in this section. First, each model's ability to simulate the eastward propagation and persistence of MJO heating is discussed. Based on three skill metrics, good MJO models are determined. Second, the differences in basic state from model to model and the resulting influence on Rossby wave propagation are examined. Lastly, the joint influence of model MJO quality and basic state quality on the ability to simulate MJO teleconnections is discussed.

4.3.1 Model MJO representation

Three diagnostics are used to determine which of the 10 models have a “good” MJO. The propagation characteristics of the model MJO are quantified by employing a diagnostic developed by the US CLIVAR MJO Working Group (MJOWG; Waliser et al. 2009). Lagged correlations of the extended winter (April – November) intraseasonal (20 – 100 day) tropical (10°S - 10°N) precipitation are used to create lag-longitude hovmöller diagrams. Following Jiang et al. (2015), the lagged correlations are calculated relative to intraseasonal precipitation in the Indian Ocean (IO; 5°S - 5°N, 75°E - 85°E) and the West Pacific (WP; 5°S - 5°N, 130°E - 150°E) for lags of -20 to 20 days (see Fig. 4 of Ahn et al. [2017] for similar lag-longitude hovmöller diagrams for all of the models used here). The pattern correlations between the observed and GCM hovmöller diagrams are then used to provide one metric for MJO skill (Jiang et al. 2015). The skill score, which we will refer to as the J15 skill score, is determined by taking the average of the pattern correlations derived for WP and IO reference points, with the “good” MJO models exceeding a 0.8 correlation with observations. The correlation values for WP and IO reference points and their average are provided in Table 4.2. Based on this skill score, CNRM-CM5, GFDL-CM3, MIROC5, MRI-CGCM3, and NorESM1-M have a relatively good MJO.

Another commonly used skill metric developed by the MJOWG utilizes the extended winter wavenumber-frequency power spectrum of precipitation to assess the eastward and westward propagating components of the MJO (e.g. Waliser et al. 2009; Ahn et al. 2017). Precipitation output from GPCP and each GCM is averaged between 10°S - 10°N to calculate the power spectra in wavenumber-frequency space (not shown; see Fig. 1 of Ahn et al. 2017 for the precipitation power spectrum of all the models examined here). The ratio of eastward to westward propagation power (E/W ratio) in the region containing zonal wavenumbers 1 – 3 and 30 – 60 day periods is then derived. The observed E/W ratio is 2.82, which is higher than most of the "good" MJO models (Table 4.2). Although BCC-CSM1.1 fell just short of the 0.8 J15 skill score threshold, it has a higher E/W ratio than some of the good MJO models, and is therefore classified as a good MJO model here.

The ability for a model to maintain a high amplitude MJO event once it is established is also considered. Following Rashid et al. (2011), MJO persistence is evaluated by using the two-dimensional phase-space created by the RMMs (Figure 4.1), where a strong MJO event is characterized by the counter-clockwise evolution of the RMM indices with an amplitude greater than 1 (i.e. outside of the unit circle shown). The initial point of each trajectory, indicated by a large filled circle outside of the unit circle, represents the average RMM1 and RMM2 values for each quadrant in the RMM phase-space for each model and reanalysis. The average MJO evolution beginning in each quadrant is shown for 16 days with the exception of CNRM-CM5 (light blue), which is shown for 51 days due to its strong persistence of high amplitude behavior. MJO events in phases 1 and 2 (bottom left quadrant) decay after an average of 14 days in ERA-Interim, where decay is defined as the last day the MJO amplitude remains above 1. This quadrant is associated with MJO initiation in the western Indian Ocean, indicating that on average observed MJO events do not persist for the full MJO life cycle of approximately 30 – 60 days, in agreement with Rashid et al. (2011). Model MJO evolution that decays within the same quadrant as its initial point indicates an inability of the model to maintain strong MJO amplitude (e.g. CanESM2, IPSL-CM5A-MR, GFDL-ESM2M, and GFDL-ESM2G). The average MJO event in these models are short-lived and likely developed within the same phase in which they decay. This behavior might also reflect non-MJO variability temporarily projecting onto observed RMM structures. In general, the MJO in the poor MJO models decays faster than that in the good MJO models for all MJO phase quadrants. The three MJO skill diagnostics examined here generally agree on six of the 10 models having a good MJO (indicated in bold in Table 4.1), and these models will be referenced as such for the remainder of this study.

4.3.2 Model basic state

The characteristics of Rossby wave propagation are strongly influenced by the basic state. The dispersion of Rossby waves, as described in Hoskins and Ambrizzi (1993) and others, is largely determined by the mean upper-tropospheric zonal wind. The DJF-mean 250-hPa zonal winds for the good MJO models are shown in Figure 4.2 (black contours), where the difference between each model and reanalysis is represented by the shaded color contours. Large errors in the strength, extent, and location of the mean Pacific subtropical jet are apparent in most of models shown. The subtropical jet in MRI-CGCM3, GFDL-CM3, and MIROC5 extends too far east relative to reanalysis. Furthermore, a southward shift of the jet is apparent in MIROC5. NorESM1-M has the smallest mean zonal wind errors in the Pacific out of the models shown.

The large differences in the model upper-level zonal winds introduce significant biases in Rossby wave propagation. Their possible impacts are discussed by utilizing the stationary wavenumber ($\mathrm{K_s}$) on Mercator coordinates following Karoly (1983) and Hoskins and Ambrizzi (1993):

$$\mathrm{K_s} = \left(\frac{a\beta_M}{\bar{u}_M}\right)^{\frac{1}{2}} \tag{4.1}$$

where the Mercator zonal wind, $\bar{u}_M$, is the mean 250-hPa zonal wind divided by the cosine of latitude, and a is the radius of the earth. β_M is the meridional gradient of absolute vorticity on a sphere, defined by:

$$\mathrm{\beta_M} = \frac{2\Omega\cos^2\theta}{a} - \frac{\partial}{\partial y}\left[\frac{1}{\cos^2\theta}\frac{\partial}{\partial y}(\cos^2\theta\bar{u}_M)\right] \tag{4.2}$$

where θ is latitude and Ω is Earth's rotational constant. Although the DJF mean zonal wind does not truly characterize the flow on any given day, it is still a qualitatively useful diagnostic to understand and to compare the anticipated behavior of stationary Rossby waves in the GCMs. In linear dynamics, Rossby waves of stationary wavenumber k are anticipated to be reflected at or decay beyond the turning latitude in which $\mathrm{K_s} = k$. Furthermore, Rossby waves are refracted towards values where $\mathrm{K_s} > k$, so that regions where $\mathrm{K_s}$ is maximized, such as the westerly jets, act as waveguides (Hoskins and Ambrizzi 1993). Such general behaviors suggested by Rossby wave theory are useful indicators of how the basic state in the GCMs impacts Rossby wave propagation.

Figure 4.3 shows $\mathrm{K_s}$ as calculated by (4.1) for the six good MJO GCMs and ERA-Interim. Regions where the mean zonal wind is easterly ($\bar{u}_M < 0$) are in white. Based on Rossby wave theory, these are regions where Rossby waves cannot propagate. Areas where $\mathrm{\beta_M} < 0$ are shaded in black. These regions indicate that the meridional gradient of absolute vorticity is reversed, and stationary Rossby waves must turn before these latitudes (e.g. Hoskins and Ambrizzi 1993). A reversal of the absolute vorticity gradient is often observed on the poleward flank of the subtropical jet, so that Rossby waves emitted by Indian Ocean or West Pacific heating must travel east before they can propagate north. In instances that the jet extends too far east (e.g. MRI-CGCM3 and GFDL-CM3; Figure 4.2), the region in which $\beta_M < 0$ also extends further east (Figure 4.3). Based on this simple quantity it is expected that in the models with an extended jet the MJO Rossby waves would travel further east in the Pacific relative to reanalysis, leading to inaccuracies in the teleconnection patterns downstream.

MJO Rossby waves in the extratropics are generally characterized by stationary zonal wavenumber 2 – 4 (e.g. Seo et al. 2016). Since Rossby waves do not propagate beyond their corresponding turning latitude, an approximate boundary for MJO Rossby waves is the $K_s = 3$ contour. In ERA-Interim, BCC-CSM1.1, CNRM-CM5, and NorESM1-M, a $K_s = 2 - 4$ Rossby wave initiated by a Rossby wave source in the Pacific subtropical jet will propagate east in the subtropical jet waveguide and may travel northeast over North America, following a waveguide bounded by the $K_s = 3$ contour. The GCMs with this northeast waveguide do not have a zonally extended subtropical jet. Similar Rossby waves may behave differently in GDFL-CM3, MIROC5, and MRI-CGCM3, due to the eastward extension of the $\beta_M < 0$ region. Figure 4.3 suggests that Rossby waves in these GCMs may propagate in a more zonally-oriented pathway over the North Pacific.

4.3.3 MJO teleconnections

With a basic understanding of model MJO quality and the differences in the background flow, this section examines the MJO teleconnection patterns in the GCMs. The composite pentad 250-hPa geopotential height anomaly and anomalous tropical precipitation is examined for all 10 GCMs for each MJO phase. We define a pentad as the average from lag 0 to lag 4 of an MJO phase, where lag 0 is the full unlagged MJO phase composite, lag 1 is the phase composite shifted by one day, and so on. In this definition, lag 0 is the composite of all DJF days in a given MJO phase where the RMM amplitude is greater than 1, including days in the same MJO event as well as all other strong events. The lagged pentad contains the average during that phase as well as out to four days after that MJO phase so that much of the Pacific teleconnection pattern associated with an MJO phase can be represented in one figure. A two-tailed Student's t-test is used to determine the geopotential height anomalies found to be significantly different from zero using N/d_M independent samples, where N represents the number of days per MJO phase and d_M is the average length of an MJO phase ($d_M = 5$ for reanalysis, e.g. Henderson et al. 2016; Alaka and Maloney, 2012). Values of N are provided in Table 4.3 in parenthesis for each good MJO model and the model d_M values vary from 4 – 6.

The teleconnection patterns associated with MJO phase 3 (Figure 4.4) and phase 7 (Figure 4.5) are provided for the good MJO models as examples, along with composite MJO precipitation anomalies. These MJO phases, characterized by opposite signed precipitation anomalies to each other, are chosen since their teleconnection patterns are associated with significant changes in much of the extratropical atmosphere (e.g. Lin et al. 2010), including robust changes in the NAO pattern and east Pacific and Atlantic blocking (e.g. Cassou 2008; Lin et al. 2009; Henderson et al. 2016). While all of the GCMs shown in Figures 4.4 and 4.5 have a relatively good MJO, it is clear that the MJO teleconnection patterns have many differences from reanalysis (top left) in most cases. This is not surprising considering the large differences between the model basic states previously discussed. In agreement with the discussion of Figure 4.3, for example, the GCMs with an extended jet demonstrate an eastward shift in the MJO teleconnection patterns (e.g. MRI-CGCM3, GFDL-CM3). The MRI-CGCM3 and GFDL-CM3 geopotential height anomalies east of the Dateline are significantly different from reanalysis at the 95% level based on a two-tailed difference of means test (not shown). Furthermore, the MIROC5 teleconnection patterns hint of a zonally-oriented pathway over the Pacific and North America, although the impact of such a pathway is unclear. A difference of means test suggests that regional East Pacific anomalies of the opposite sign as reanalysis in MIROC5 (Figure 4.4) are significantly different from reanalysis at the 95% level (not shown). In addition to the basic state, the teleconnection patterns may be influenced by errors in the amplitude and structure of MJO precipitation anomalies (color shading). In the bad MJO models (not shown), the teleconnection patterns tend to either show no resemblance to reanalysis or be very weak.

To better quantify the differences in the teleconnection patterns between the models and reanalysis, pattern correlations of 250-hPa geopotential height anomalies between reanalysis and each model are calculated for all MJO phases over the Pacific and North American region (15°N - 80°N, 130°E - 60°W). These values are provided for each MJO phase of the good MJO models in Table 4.3. The teleconnection pattern correlations are then averaged over all MJO phases for each model and represented in Figure 4.6 (y-axis in both panels). CNRM-CM5 has the highest average teleconnection pattern correlation and GFDL-ESM2G the lowest. Not surprisingly, the poor MJO models have relatively low average pattern correlations. Some of the good MJO models, however, tend to produce as poor of teleconnection patterns as the poor MJO models, such as GFDL-CM3, NorESM1-M, and MRI-CGCM3. To begin to understand why this may be the case, the teleconnection pattern correlations are first compared to the E/W ratio MJO skill metric previously calculated (Figure 4.6a, x-axis). Comparison to the E/W ratio shows that the models with a relatively good MJO tend to have better MJO teleconnection patterns, with a correlation of 0.61 between the axes (excluding the ERA-Interim reference correlation), which is significant at the 90% confidence bounds based on a two-tail test. However, a good MJO does not necessarily mean accurate representation of the MJO teleconnection patterns. For example, MRI-CGCM3 has an average teleconnection pattern correlation of only 0.43, despite having the closest MJO E/W ratio to observations. This suggests that to better understand the skill of the MJO teleconnection patterns, it is important to examine the basic state as well as the structure of anomalous MJO convection.

The teleconnection pattern correlations are compared to two basic state skill metrics derived from the DJF mean 250-hPa zonal wind (U_{250}). The first basic state skill metric for the good MJO models is the root mean squared (RMS) error of U_{250} over the Pacific domain (15°N – 60°N, 110°E – 120°W; Figure 4.6b, plus symbols). The highest U_{250} RMS errors are observed in MRI-CGCM3 and MIROC5. The former has the largest eastward extension of the jet out of all the models, whereas the latter exhibits the southward shift of the Pacific jet (Figure 4.2). However, MIROC5 has the second highest average teleconnection pattern correlation, indicating that teleconnection pattern error is not likely related with overall error in zonal wind. In fact, the U_{250} error for the full Pacific domain is poorly correlated with MJO teleconnection skill (r = -0.31).

The second U_{250} skill metric specifically focuses on the longitudinal errors of the subtropical jet. This metric is calculated by finding the latitude of the maximum winds in the subtropical jet for both models and reanalysis, isolating latitudes 5° to the north and to the south of this maximum, and then calculating the RMS error between the model and ERA-Interim DJF mean U_{250} within the region defined by these latitudes and longitudes 110°E – 120°W. This ensures that the RMS error is based on the longitudinal error of the jet, and not any latitudinal shifts. The longitudinal RMS error skill metric (Figure 4.6b, filled circles) has a correlation of -

0.64 with the teleconnection pattern correlations (y-axis). In general, the models with an eastward-extended jet tend to have lower average teleconnection pattern skill among the good MJO models. The exception is NorESM1-M, which has a similar zonal wind RMS error as CNRM-CM5. Although its pattern correlation during phase 3 is relatively good (r = 0.66; Table 4.3), its lower average teleconnection pattern correlation may be due to the structure of the model MJO precipitation anomalies, which tends to be zonally elongated (e.g. Figures 4.4 and 4.5) during most MJO phases.

The combined impact of the basic state subtropical jet and MJO quality on the MJO teleconnection patterns, as well as some differences in teleconnection skill during different MJO phases, can be better understood by examining the Rossby wave source (RWS) associated with each MJO phase. Following Sardeshmukh and Hoskins (1988), the RWS can be defined as:

$$\mathrm{RWS} = -\nabla \cdot (\mathbf{V}_\chi \zeta) = -\mathbf{V}_\chi \cdot \nabla\zeta - \zeta \mathrm{D} \tag{4.3}$$

where ζ is the absolute vorticity, $\mathbf{V}_\chi$ is the irrotational (divergent) component of the horizontal wind vector, and $\mathrm{D} = \nabla \cdot \mathbf{V}_\chi$. The right hand side of (4.3) demonstrates that the RWS can be described as the sum of the advection of absolute vorticity and vortex stretching by the divergent wind. The sign of RWS anomalies are relative to the background absolute vorticity, with positive RWS in regions of divergence (convergence) in down-gradient (up-gradient) mean absolute vorticity (e.g. Hsu 1996). The anomalous RWS at 250-hPa composited relative to MJO phase 3 is shown in Figure 4.7 for the good MJO models. For reference, the $\mathrm{K_s} = 3$ contour is overlaid and the $\beta_\mathrm{M} < 0$ region is hatched (see Fig. 4.3). Although only phase 3 is shown as an example, anomalous RWS characteristics are very similar for all MJO phases for most models.

Examining the two terms of (4.3) independently (not shown) indicates that for most of the models, the RWS anomalies during most MJO phases (including phase 3) are largely due to vortex stretching by the divergent wind. The anomalous divergence field associated with MJO convection leads to anomalous convergence generally on the southern flank of the subtropical Pacific jet that generates anomalous vorticity and triggers Rossby waves such as those shown in Figures 4.4 and 4.5. This process is the primary component of the RWS in all models during MJO phase 3 except in MRI-CGCM3, which has a stronger contribution from the advection of absolute vorticity that is overestimated relative to reanalysis. As a result, MRI-CGCM3 has a strong anomalous RWS east of the strongest RWS anomaly in ERA-Interim (Figure 4.7).

For MJO phases 2 – 3 (only phase 3 shown; Figure 4.7), BCC-CSM1.1 and NorESM2-M produce weaker anomalous RWS than reanalysis and typically the weakest RWS relative to all of the good MJO models examined here. However, both models demonstrate a stronger RWS anomaly during MJO phases 6 – 7 (not shown) that are more comparable to reanalysis. This difference in RWS strength may partially explain the weaker MJO teleconnection patterns during MJO phase 3 (Figure 4.4) relative to phase 7 (Figure 4.5) in the two models.

Of particular interest is the anomalous RWS of the opposite sign east of the Dateline that is prominent in some models and ERA-Interim, although the longitudinal position of this anomaly varies (Figure 4.7). For example, there is a strong positive RWS anomaly near 135°W that extends over the west coast of North America in MRI-CGCM3 and GFDL-CM3, whereas the positive RWS is near 150°W in ERA-Interim. The positive anomalous RWS, caused by anomalous convergence, coincides with the exit region of the jet, as evident when comparing the RWS anomaly to the extent of the jet (compare Figures 4.2 and 4.7), and likely affects the teleconnection patterns across the Pacific and North America. In other words, the erroneous eastward shift of the positive RWS anomaly may partially account for some of the differences observed in the MRI-CGCM3 and GFDL-CM3 teleconnection patterns relative to other models and ERA-Interim (Figures 4.4 and 4.5).

4.4 Linear Baroclinic Model (LBM) Experiments

One issue with the composite analysis above is that it is not easy to separate the impact of model MJO convection from the influence of the model basic state for determining the quality of the teleconnection pattern. We therefore employ a LBM in this section to examine the impact of the model MJO and basic state independently in order to better understand the differences in the teleconnection patterns.

4.4.1 LBM description and setup

In the LBM, the hydrostatic primitive equations on a sphere are linearized about a basic state and the linear response to a prescribed forcing is calculated (Watanabe and Kimoto 2000). The resolution is set to T42 with 20 sigma levels in the vertical. For the numerical damping, horizontal diffusion with an e-folding timescale of 2 hours for the largest wavenumbers is set. The model also employs Newtonian damping with a time scale of 20 day^{-1} for most vertical levels and a timescale of 0.5 day^{-1} for the lowest and highest levels. These parameters are set to be the same for all experiments to ensure that the differences in the LBM results are due to differences in MJO heating and the basic state, not due to changes in the LBM parameters. For more specific details on the LBM beyond that described here, please refer to Watanabe and Kimoto (2000).

The anomalous MJO apparent heat source (Q_1) of each GCM is used to force the LBM. Formulated by Yanai et al. (1973), Q_1 includes heating associated with radiation, latent heat release due to phase changes of water, and the vertical eddy transport of sensible heat. The three-dimensional Q_1 is derived as a residual from the dry static energy (s) budget, where $s = \mathrm{c_p T} + \mathrm{gz}$, T is temperature, $\mathrm{c_p}$ is the specific heat capacity of air at a constant pressure, g is the gravitational constant, and z is height. Q_1 is represented by:

$$Q_1 = \frac{\partial s}{\partial \mathrm{t}} + \nabla \cdot (s\mathbf{V}) + \frac{\partial (s\omega)}{\partial \mathrm{p}} \tag{4.4}$$

where $\mathbf{V}$ is the horizontal wind vector and omega (ω) represents the pressure velocity. The anomalous heat source is calculated as follows: First, Q_1 anomalies (Q_1') are computed by removing the long-term daily mean and first three harmonics of the seasonal cycle from Q_1 (Eq. 4.4). Second, Q_1' is composited relative to MJO phase for ERA-Interim and each GCM, resulting in eight MJO phase latitude-longitude Q_1' composite maps. Third, in order to capture the eastward propagation of the MJO, Q_1' is linearly interpolated in time between adjacent MJO phases. Each MJO phase is assumed to last 6 days. This length is idealized since the length of an MJO phase will vary from model to model as well as from phase to phase within a model (e.g. Figure 4.1). The average length of MJO phases 3 and 7 between all of the good MJO models and reanalysis is calculated to be 6 days, so this value is chosen. The final propagating heat source for each dataset is then a series of Q_1' composite maps over the course of a 48-day idealized MJO cycle beginning at MJO phase 1.

In the experiments described below, the model is forced with the propagating Q_1' as described above, and the model response is shown as the average 250-hPa geopotential height anomaly from days 8 – 18, which corresponds to the latter half of phase 2 and all of phase 3. Similar results were obtained with a stationary phase 2 forcing used to spin-up the LBM for 3 to 5 days prior to propagating the MJO heat source eastward (not shown). A propagating MJO heat source (e.g. Matthews et al. 2004) is used here instead of a steady single-phase heat source (e.g.

Seo and Son 2012) because MJO phase 2 also likely plays an important role in the teleconnection patterns shown in Figure 4.4. This is a reasonable assumption given the decay timescales of MJO phases (e.g. Figure 4.1), which for the good MJO models tend to persist the MJO for more than one phase. The time it takes Rossby wave propagation to reach the North Pacific and North America from the tropical warm pool also typically exceeds one MJO phase (e.g. Lin et al. 2009). Due to the use of a propagating heat source, the LBM does not reach steady state. We note that the time period of the response is chosen to highlight the teleconnection pattern over the Pacific basin; anomalies over North America associated with the MJO may not yet have fully developed to allow a direct comparison to Figure 4.4.

4.4.2 LBM basic state and MJO heating experiments

Three sets of experiments are carried out for each good MJO model in addition to a reference run using reanalysis. First, both the GCM basic state and the GCM Q_1' are used to assess the ability of the LBM to reproduce the Pacific MJO teleconnection patterns shown in Figure 4.4 (hereby referred to as the Q1BS runs). To determine the impact of the GCM basic states for producing model bias in the teleconnection patterns, the LBM is then run using the reanalysis Q_1' with the basic state of each GCM (hereby referenced as the BS runs). The influence of the GCM's MJO heating is then examined by using the GCM Q_1' in conjunction with the reanalysis basic state (referred to as the Q1 runs).

The geopotential height response for the reference run, which utilizes the reanalysis Q_1' with the reanalysis basic state, is shown in Figure 4.8. The reference run reasonably captures the general location of the Pacific anomalies relative to reanalysis (Figure 4.4) with a pattern correlation of 0.72 for the region 15°N – 80°N, 120°E – 120°W. Also shown are the LBM experiments for MRI-CGCM3 (Figure 4.9), CNRM-CM5 (Figure 4.10), and MIROC5 (Figure 4.11). For brevity, the LBM runs associated with the other good MJO models are discussed as appropriate but not shown. The statistics from these other simulations will be compiled in Figure 4.13, however.

4.4.3 LBM runs with model BS and Q_1

The geopotential height response of the Q1BS runs is shown in the third panel of Figures 4.9 – 4.11 (black contours) for the three GCMs previously mentioned. Also shown in color contours is the difference between the average Q1BS geopotential height response and the average from the reference run (Figure 4.8). To determine how well the LBM captures the Pacific teleconnection pattern associated with the early phases of the MJO, and therefore justifying the use of the LBM, pattern correlations for the geopotential height anomalies are calculated for 15°N – 80°N, 120°E – 120°W between the Q1BS runs for all good MJO models (e.g. third panel of Figures 4.9 – 4.11, black contours) and their corresponding composites from Figure 4.4. The average pattern correlation is 0.79, with individual pattern correlations ranging from 0.66 to 0.91. These pattern correlations exclude North America, which is not yet fully developed in many of the LBM experiments shown.

The Q1BS runs demonstrate that the LBM is able to capture some of the teleconnection pattern biases in Figure 4.4. For example, the MRI-CGCM3 Q1BS run shows a clear eastward shift of the anticyclonic anomaly over the Pacific relative to ERA-Interim, as highlighted by the color contours (Figure 4.9; third panel). There also appears to be a portion of the response in the Q1BS runs for the MIROC5 run (Figure 4.11) that is more zonally oriented, indicated by a southward extension of the negative geopotential height anomaly over western North America (see color shading) relative to the reanalysis reference run (Figure 4.8). A possible cause of this southward extension will be discussed in Section 4.4.4, but was also suggested by Figure 4.3. In addition, clear differences exist in the amplitude of the responses. This is particularly true for the CNRM-CM5 Q1BS run (Figure 4.10, third panel), which has a very similar pattern to the reference run, but has geopotential height anomaly differences of up to 45 m (color contours). This amplitude difference may be an artifact of using the same LBM parameters such as damping coefficients for all LBM runs, and will be discussed in more detail at the end of this section (Section 4.4.5).

4.4.4 Basic state and Q1 runs

In agreement with the basic state discussion (Section 4.3.2), the GCMs containing an eastward-extended Pacific subtropical jet result in an eastward shift of the teleconnection patterns (e.g. Figure 4.9, top panel) relative to the reanalysis reference run (Figure 4.8). The MRI-CGCM3 BS run, which has the greatest jet extension of the model basic states, demonstrates the largest eastward shift in the anticyclonic Pacific anomaly out of all of the LBM BS runs. An eastward shift is also evident in the GFDL-CM3 BS run (not shown) as well as, to a lesser extent, the MIROC5 BS run (Figure 4.11). The extended Pacific jet has downstream effects on the teleconnection pattern. For example, the negative geopotential height anomaly over Alaska and the Pacific Northwest in the reference run (Figure 4.8) develops further eastward in MRI-CGCM3 (Figure 4.9; top panel). Anomalies over Northeast North America and the Atlantic also contain errors associated with this shift at later times (not shown).

Some evidence exists for a more zonally oriented pathway in the BS runs of the models with an extended jet, in agreement with the discussion in Section 4.3.2. For example, the negative geopotential height anomaly center over North America in the MRI-CGCM3 BS run (Figure 4.9, top) is shifted south relative to the same anomaly in the reference reanalysis run (Figure 4.8). The behavior is also seen in the other runs with an extended jet (e.g. MIROC5 [Figure 4.11], and GFDL-CM3 [not shown]). This suggests that errors in a GCM's basic state can shift the direction of Rossby wave propagation as previously discussed in reference to Figure 4.3.

The importance of the GCM MJO heating perturbations to the quality of the teleconnection patterns is investigated by forcing the LBM with each GCM's Q_1' but using the reanalysis basic state (Figures 4.9 – 4.11, second panels). Although the structure of Q_1' varies greatly from one GCM to the other (Figures 4.9 – 4.11, bottom panels), the circulation anomalies from the Q1 runs appear qualitatively similar to the reference run (Figure 4.8), with the most apparent difference being in the amplitude of the response. For example, the NorESM2-M Q_1' field (not shown), which has comparable amplitude to the reanalysis Q_1' (Figure 4.8), is zonally elongated with an Indian Ocean heating that is split about the Equator (e.g. Figure 4.4 precipitation field). Despite the large differences from the reanalysis Q_1', forcing the LBM with this heating produces a teleconnection pattern similar to reanalysis with the key difference being the amplitude of the response (not shown). As discussed in Sardeshmukh and Hoskins (1988) and references therein, the model response to tropical heating near the subtropical jet is relatively insensitive to the longitudinal location of the heating. Referring back to the RWS associated with each GCM (Figure 4.7), it can be seen that despite the differences in Indo-Pacific Q_1' structure and location, the RWS still maximizes in the subtropical jet where it can efficiently generate Rossby waves.

Some of the errors in the GCM teleconnection patterns (Figure 4.4) may be due to the Q_1' east of the Dateline (e.g. Figures 4.9 – 4.11, bottom), which is associated with a RWS that occurs near the exit region of the subtropical jet (e.g. Figure 4.7). The influence of this heat source was examined through a sensitivity test using the basic state and Q_1' of MRI-CGCM3, except that Q_1' is set to zero east of 170°W, thereby eliminating the heat source east of the Dateline. The average 8 – 18 day geopotential height anomaly response (Figure 4.12; top panel) shows an overall weakening in amplitude, with the exception of the anomalous anticyclone north of the West Indian Ocean, which is slightly strengthened. Furthermore, the negative geopotential height anomaly over North America is shifted north relative to the Q1BS run shown in Figure 4.9. This northward position better aligns with the negative geopotential height anomaly in the reference run (Figure 4.8). This anomaly, however, is still shifted east relative to the reference run due to the MRI-CGCM3 basic state. These results suggest that MJO heating east of the Dateline influences the amplitude and pathway of MJO Rossby waves. Similar results were obtained with MIROC5 (Figure 4.12; bottom panel) and CNRM-CM5 (not shown) when setting Q_1' to zero east of 170°W and east of the Dateline, respectively. In the MIROC5 modified experiment (Figure 4.12; bottom panel), the zonally-oriented pathway present in the Q1BS run (Figure 4.11, third panel) was largely reduced. This suggests that in addition to the errors introduced by the basic state, the Q_1' east of the Dateline may contribute to the zonally-oriented teleconnections previously mentioned for the LBM experiments and the teleconnection pattern composites (Figures 4.4 and 4.5). We note, however, that more work is needed to understand the impact of the zonally-oriented teleconnections.

A caveat is that the LBM does not allow interactions with the background flow nor non-linear feedbacks; rather, it calculates the direct response to the MJO heating. Although this is an idealized assumption, the LBM can recreate many features of the composite teleconnection patterns of interest here, suggesting that the teleconnection patterns are primarily forced by MJO heating and not a result of internal extratropical variability.

4.4.5 LBM teleconnection pattern skill

In order to better quantify the improvement or degradation associated with the model MJO heating anomalies and/or basic state to the teleconnection patterns in the LBM across all models, pattern correlations are calculated between the response of the LBM experiments and the ERA-Interim reference run for the Pacific region (120°E – 120°W; Figure 4.13). The BS runs (open circles) have a lower pattern correlation than the Q1 runs (squares) in the majority of models, with the largest differences for MRI-CGCM3. This suggests that in good MJO GCMs, large errors in the basic state may potentially degrade the teleconnection patterns more than errors in the Q_1' structure. An exception is NorESM1-M, which has a relatively good basic state (e.g. Figure 4.2), so the impact of the Q_1' structure is more prominent. Similar LBM experiments were performed using a propagating heat source beginning in MJO phase 5, where the 8 – 18 day average approximately represents the middle of MJO phase 6 and all of MJO phase 7. Most of these LBM runs exhibit very similar characteristics as those discussed for the MJO phase 2 – 3 LBM experiments, and hence these results are not shown here.

4.4.6 LBM response amplitude

As previously mentioned, a very noticeable difference between many of the GCM runs and the reference run is the amplitude of the circulation anomalies. One possibility for these variations in amplitude is differences in basic state tropical static stability, which modulates the strength of divergence associated with an MJO Q_1 anomaly (e.g. Maloney and Xie 2013). Environmental static stability can be represented by the time mean vertical gradient of dry static energy ($\partial\bar{s}/\partial$p). On characteristic timescales of the MJO, the dominant thermodynamic energy balance in the tropics that results from conditions of weak temperature gradients is (Wolding et al. 2016):

$$Q_1' = \omega' \frac{\partial \bar{s}}{\partial \mathrm{p}} \tag{4.5}$$

where ω' is the vertical velocity perturbation associated with the MJO convection. The DJF mean 200 – 500-hPa vertically averaged static stability is calculated for each good MJO GCM over the MJO region (60°E – 180°, 20°S – 20°N). The areal average for each model is provided in Table 4.2. All models, particularly CNRM-CM5 and MIROC5, underestimate the maximum amplitude of the environmental static stability. In the BS runs, where Q_1' remains the same for all models, a decrease in dry static stability amplitude would be balanced by a relative increase in ω' based on (4.5). Stronger ω' associated with MJO heating would scale with stronger upper-level divergence (e.g. Maloney and Xie 2013), and thereby higher amplitude stationary Rossby wave amplitudes such as that shown by the CNRM-CM5 BS run (Figure 4.10, top panel). In the Q1 runs, where the dry static stability is determined by reanalysis, an increase in Q_1' amplitude can also lead to higher amplitude anomalies relative to reanalysis. This can be seen in the CNRM-CM5 Q1 run (Figure 4.10, second panel), which simulates a near doubling of the vertically averaged Q_1' amplitude in the West Indian Ocean (Figure 4.10, bottom) relative to reanalysis. While an increase in Rossby wave amplitude is evident in the LBM runs, which assumes the same damping for all GCMs, Figures 4.4 and 4.5 do not show similar amplitude differences. Errors in tropical static stability or Indo-Pacific Q_1' amplitude appear to have minimal influence on the amplitude of MJO Rossby waves, suggesting the GCMs themselves likely offset these errors with stronger damping of waves.

4.5 Summary and Discussion

The MJO teleconnection patterns in 10 CMIP5 models are examined and compared. Composite analysis and the use of simple skill metrics demonstrated that some models with a relatively good MJO produce poor MJO teleconnections due to errors in the model basic state. The good MJO models with the lowest ability to recreate the MJO teleconnection patterns are those with a zonally extended Pacific subtropical jet (e.g. MRI-CGCM3 and GFDL-CM3), which also show an eastward shift in the teleconnection patterns. Utilizing a LBM, the eastward shift in the teleconnection patterns was found to be primarily due to errors in the model basic state rather than MJO structure. Furthermore, MRI-CGCM3, GFDL-CM3, as well as MIROC5, which has a lesser jet extension than MRI-CGCM3 and GFDL-CM3, suggest a zonally oriented Rossby waveguide in the mean state (Figure 4.3). Rossby waves in these models may propagate along a zonal pathway (e.g. MIROC5, Figure 4.4). These basic state errors can lead to teleconnection pattern errors downstream, suggesting that the model representation of the basic state, and especially the subtropical jet, must be considered when examining extratropical atmospheric phenomena that are strongly influenced by MJO activity.

In addition to the model basic state, MJO heating biases, even in models with a relatively good MJO, can lead to errors in the teleconnection patterns. LBM sensitivity experiments removing the GCM Q_1' east of 170°W resulted in a northward shift of the cyclonic anomaly over North America, indicating that Q_1' east of the Dateline can impact the extratropical MJO teleconnections. However, characteristics of Indo-Pacific heating in good MJO models appear to have relatively little impact on the location of teleconnection patterns, in agreement with the arguments of Hoskins and Ambrizzi (1993) and others.

Some models tend to better reproduce the MJO teleconnection amplitude and pathway associated during some MJO phases relative to other phases. As previously discussed, BCC-CSM1.1 and NorESM1-M have weaker teleconnection patterns associated with MJO phase 3 (Figure 4.4) than with phase 7 (Figure 4.5). Furthermore, some GCMs better reproduce the teleconnection patterns associated with certain MJO phases relative to others (see Table 4.3). This suggests that a model may be able to reproduce the extratropical impacts associated with, for example, MJO phase 3 (e.g. suppressed east Pacific and Atlantic blocking; Henderson et al. 2016, or a positive NAO pattern; Lin et al. 2009), but it may not be able to reproduce the opposite response and opposite impacts associated with MJO phase 7. This can lead to biases on longer timescales associated with those extratropical phenomena.

The results presented here demonstrate that both the model MJO and the basic state must be accurately represented in order to reproduce the MJO teleconnection patterns. However, as discussed in the introduction, improvements in MJO representation are often associated with a degradation of the basic state. This issue was highlighted in Yoo et al. (2015), who found that improving the model's convection scheme resulted in improved MJO simulation and MJO teleconnections in CAM5, without degrading the model basic state. Moving forward, more research such as that presented in Yoo et al. (2015) is needed to improve model MJO representation without degrading the associated MJO teleconnection patterns through basic state changes. Improvements in model MJO teleconnection patterns may reduce the biases of other extratropical phenomena impacted by the MJO, such as the NAO, blocking, the PNA pattern, and others, potentially reducing uncertainties in how they will change in future climates. In addition, the focus of this study is MJO teleconnections in ocean-atmosphere coupled GCMs. A similar analysis utilizing AMIP GCM runs or weather forecasting models may provide further insight into the behavior of MJO teleconnections in those types of models.

TABLE 4.1. CMIP5 models evaluated and their corresponding institution and horizontal resolution. Models determined to have a relatively good MJO are in bold.

	Model	Institution	Resolution
1	**BCC-CSM1.1**	Beijing Climate Center, China	2.8° x 2.8°
2	CanESM2	Canadian Centre for Climate Modeling and Analysis	2.8° x 2.8°
3	**CNRM-CM5**	Centre National de Recherches Météologuiques, France	1.4° x 1.4°
4	**GFDL-CM3**	NOAA Geophysical Fluid Dynamics Laboratory, USA	2° x 2.5°
5	GFDL-ESM2G	NOAA Geophysical Fluid Dynamics Laboratory, USA	2° x 2.5°
6	GFDL-ESM2M	NOAA Geophysical Fluid Dynamics Laboratory, USA	2° x 2.5°
7	IPSL-CM5A-MR	L'Institut Pierre-Simon Laplace, France	1.25° x 2.5°
8	**MIROC5**	AORI, NIES, JAMSTEC, Japan	1.4° x 1.4°
9	**MRI-CGCM3**	Meteorological Research Institute, Japan	1.1° x 1.1°
10	**NorESM1-M**	Norwegian Climate Centre	1.9° x 2.5°

TABLE 4.2. J15 skill metric correlation coefficients, E/W ratio values, and areal-averaged tropical dry static stability values for observations/reanalysis and the CMIP5 models. Dry static stability values are provided only for the good MJO models.

	J15 Skill Metric				
Dataset	Average	IO box	WP box	E/W ratio	$\partial\bar{s}/\partial p$
GPCP/ERA-I	1.0	1.0	1.0	2.82	-0.45
BCC-CSM1.1	0.79	0.76	0.82	2.35	-0.44
CanESM2	0.70	0.70	0.70	0.94	—
CNRM-CM5	0.92	0.92	0.92	3.99	-0.35
GFDL-CM3	0.86	0.86	0.87	1.89	-0.42
GFDL-ESM2G	0.74	0.80	0.68	1.48	—
GFDL-ESM2M	0.73	0.76	0.70	1.48	—
IPSL-CM5A-MR	0.68	0.67	0.70	1.59	—
MIROC5	0.85	0.82	0.89	1.99	-0.39
MRI-CGCM3	0.86	0.86	0.85	2.60	-0.44
NorESM1-M	0.91	0.89	0.93	2.09	-0.43

TABLE 4.3. Geopotential height anomaly pattern correlation coefficients between the good MJO models and reanalysis for each MJO phase calculated over the Pacific – North American region (15°N - 80°N, 130°E - 60°W). In parenthesis is the number of days in each MJO phase (N).

Model	Phase 1	Phase 2	Phase 3	Phase 4	Phase 5	Phase 6	Phase 7	Phase 8
BCC-CSM1.1	0.53 (292)	0.29 (332)	0.64 (376)	0.74 (414)	0.41 (259)	0.36 (289)	0.73 (418)	0.55 (405)
CNRM-CM5	0.51 (361)	0.56 (438)	0.87 (566)	0.82 (386)	0.62 (359)	0.62 (349)	0.76 (594)	0.71 (360)
GFDL-CM3	0.39 (340)	0.52 (347)	0.62 (492)	0.80 (380)	0.25 (263)	-0.01 (387)	0.39 (412)	0.82 (451)
MIROC5	0.55 (337)	0.72 (440)	0.67 (502)	0.48 (322)	0.45 (359)	0.40 (440)	0.73 (539)	0.89 (400)
MRI-CGCM3	0.73 (284)	0.71 (366)	0.28 (543)	0.55 (385)	0.17 (304)	0.10 (342)	0.22 (573)	0.71 (511)
NorESM1-M	0.14 (343)	0.62 (429)	0.66 (389)	0.48 (304)	-0.12 (321)	0.43 (447)	0.69 (419)	0.88 (365)

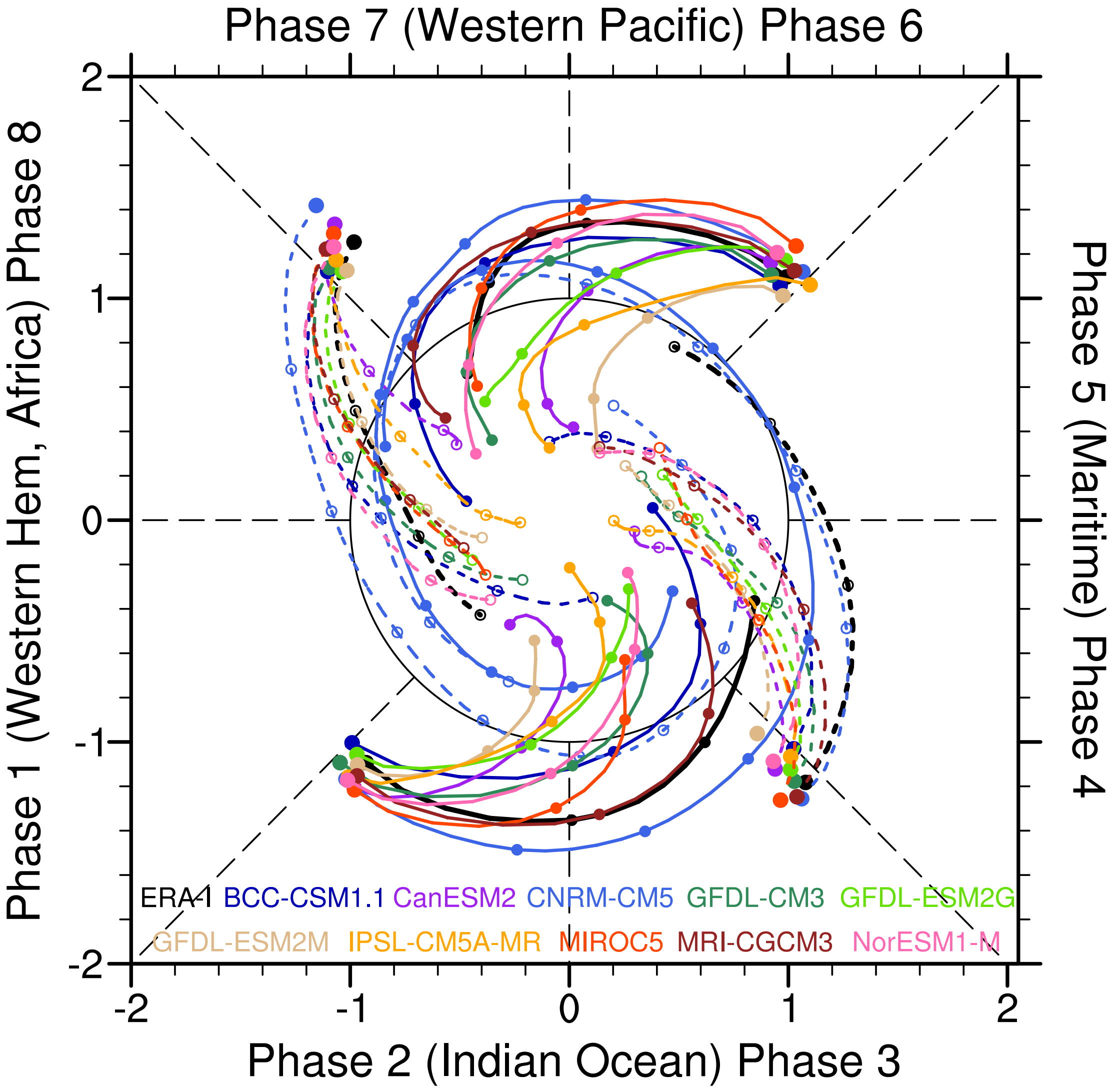

FIG. 4.1. RMM index amplitude trajectories in phase-space for reanalysis (black line) and the CMIP5 models (colored lines, see legend). Trajectories initiate when each RMM index indicates a strong amplitude MJO event (i.e. outside of the unit circle) in phases 1 – 2 (bottom left quadrant), phase 3 – 4 (bottom right), phase 5 – 6 (top right), and phase 7 – 8 (top left). Each trajectory is shown for 16 days, except for CNRM-CM5, which is shown for 51 days. Circles mark every five days. The composite RMM indices are smoothed with a 5-point running mean prior to plotting as done by Rashid et al. (2011).

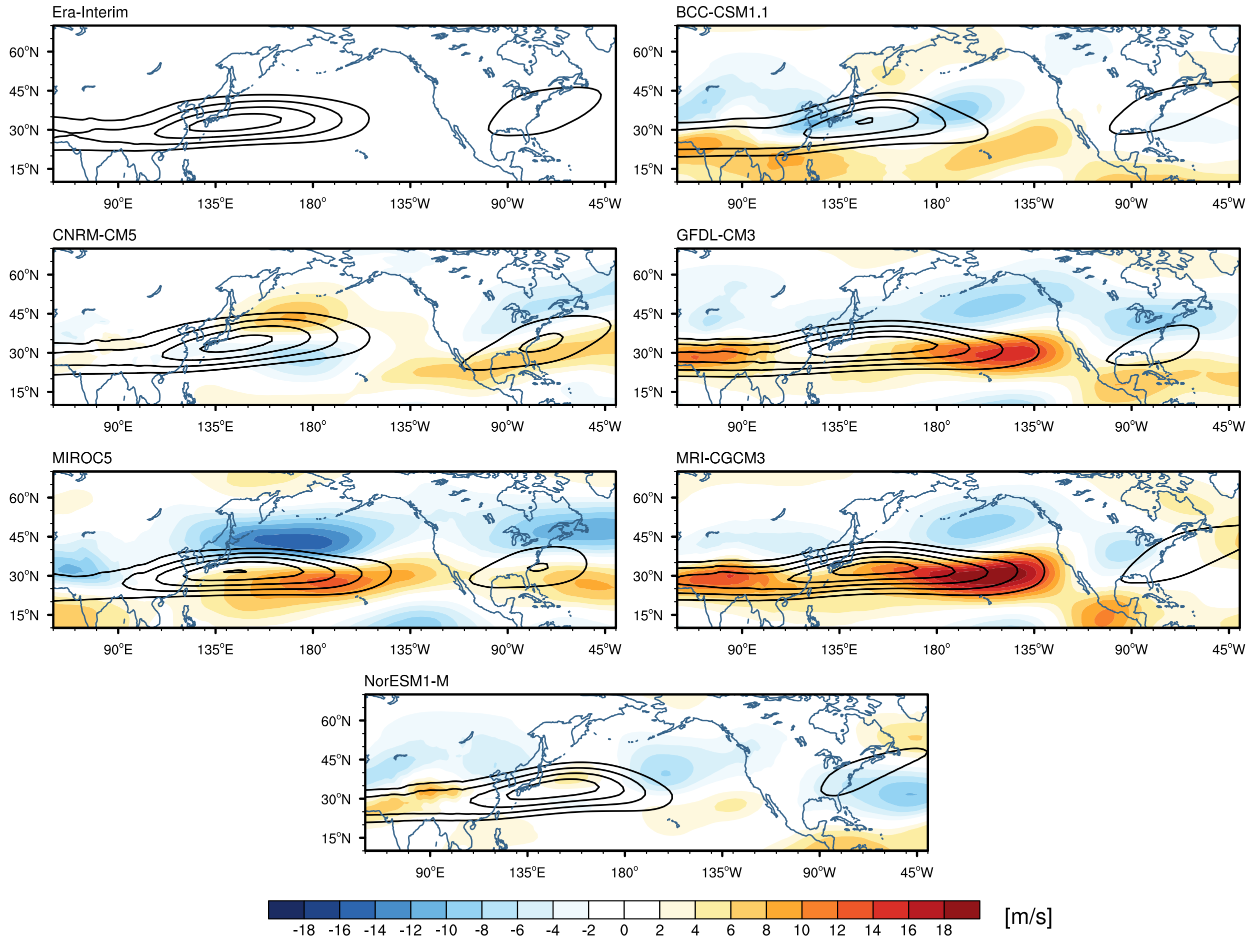

FIG. 4.2. Mean 250-hPa zonal wind (contours) for reanalysis (top left) and the good MJO models during DJF. Contours are every 10 m/s beginning at 35 m/s. Color shading represents the deviation of the model mean zonal wind from that of reanalysis.

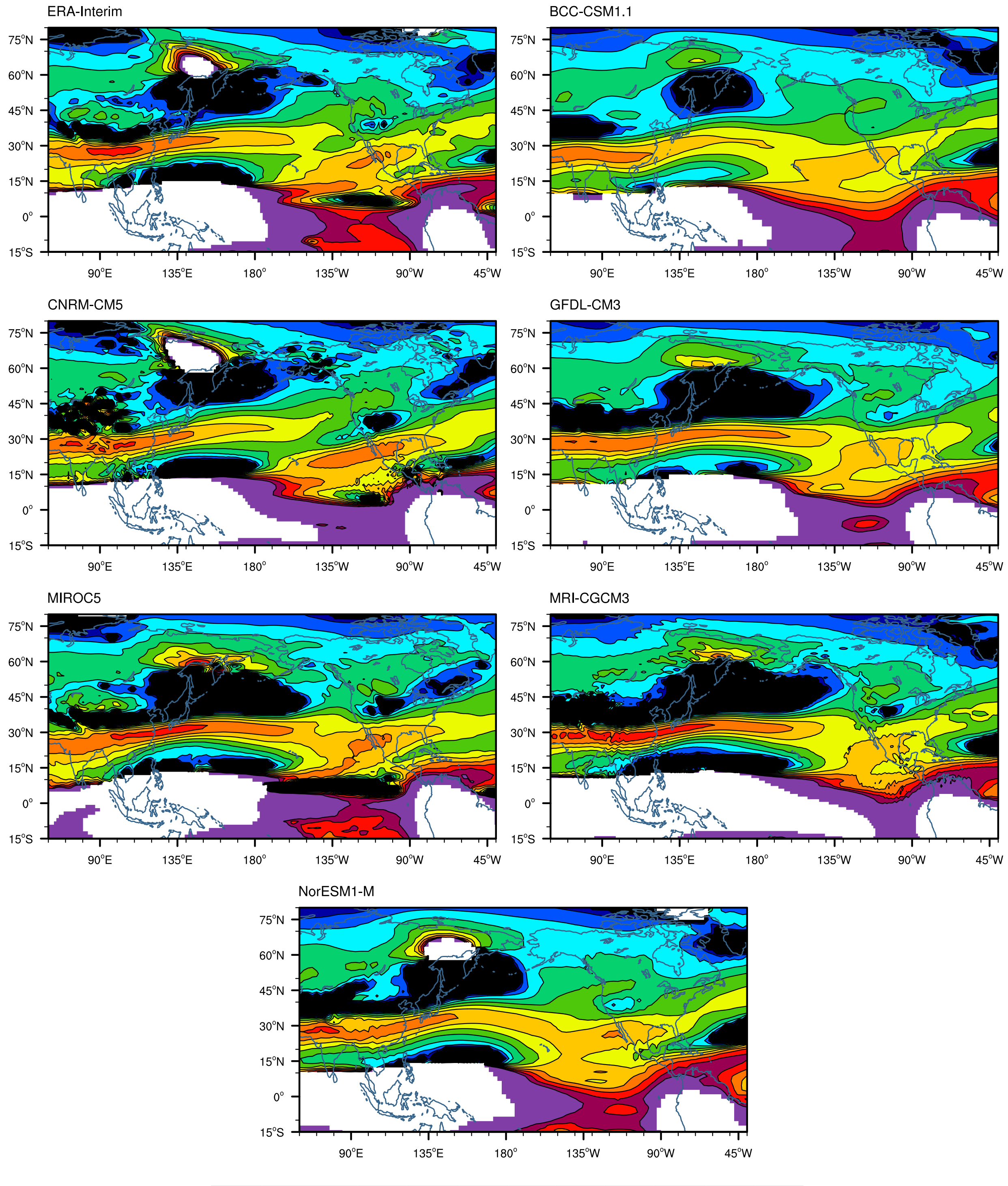

FIG. 4.3. Stationary zonal wavenumber (K_s) derived from the 250-hPa Mercator zonal wind during DJF. Areas of easterly winds ($\bar{u}_M < 0$) are in white, and regions where $\beta_M < 0$ are in black.

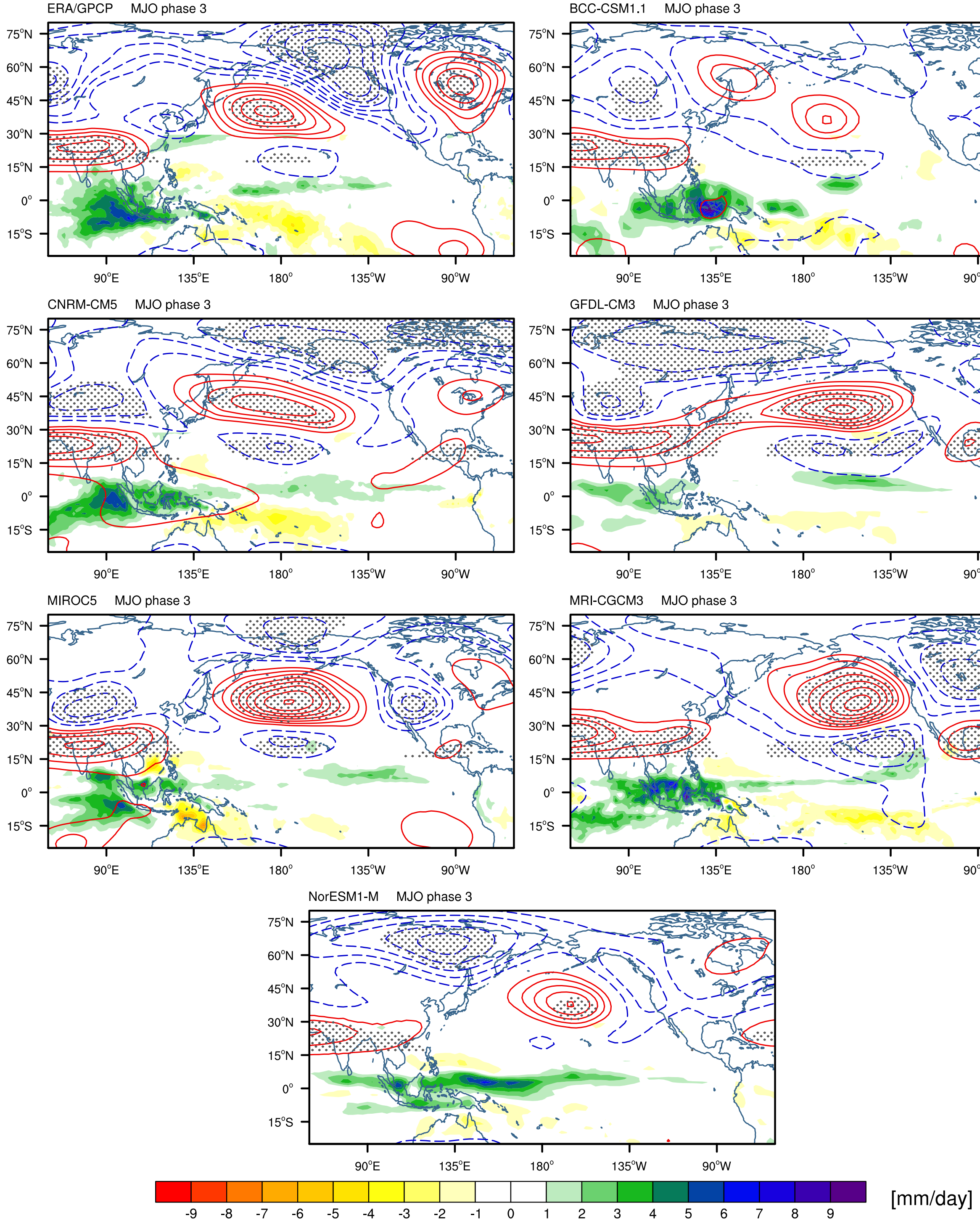

FIG. 4.4. MJO phase pentad composites of anomalous 250-hPa geopotential height (right column), where a pentad denotes a 5-lag mean, or the field average of lags 0-4 following an MJO phase. Positive geopotential height anomalies are in red solid contours, and negative anomalies are in blue dashed contours. Contours are every 10 m, and the zero contour is omitted. Anomalies found to be 95% significantly different from zero are dotted. The color shading shows the anomalous tropical precipitation composite during each MJO phase.

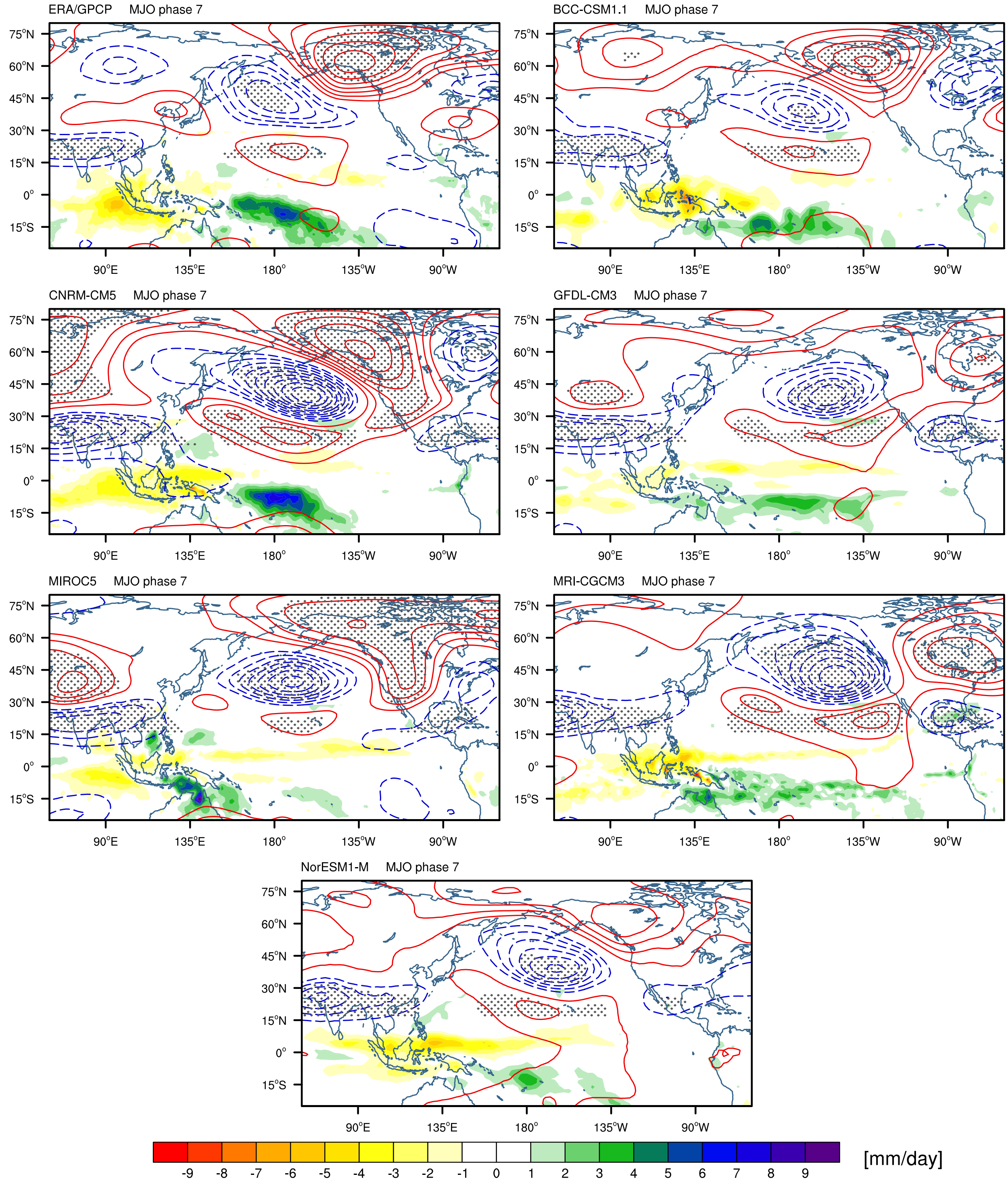

FIG. 4.5. Same as Figure 4.4, but for MJO phase 7.

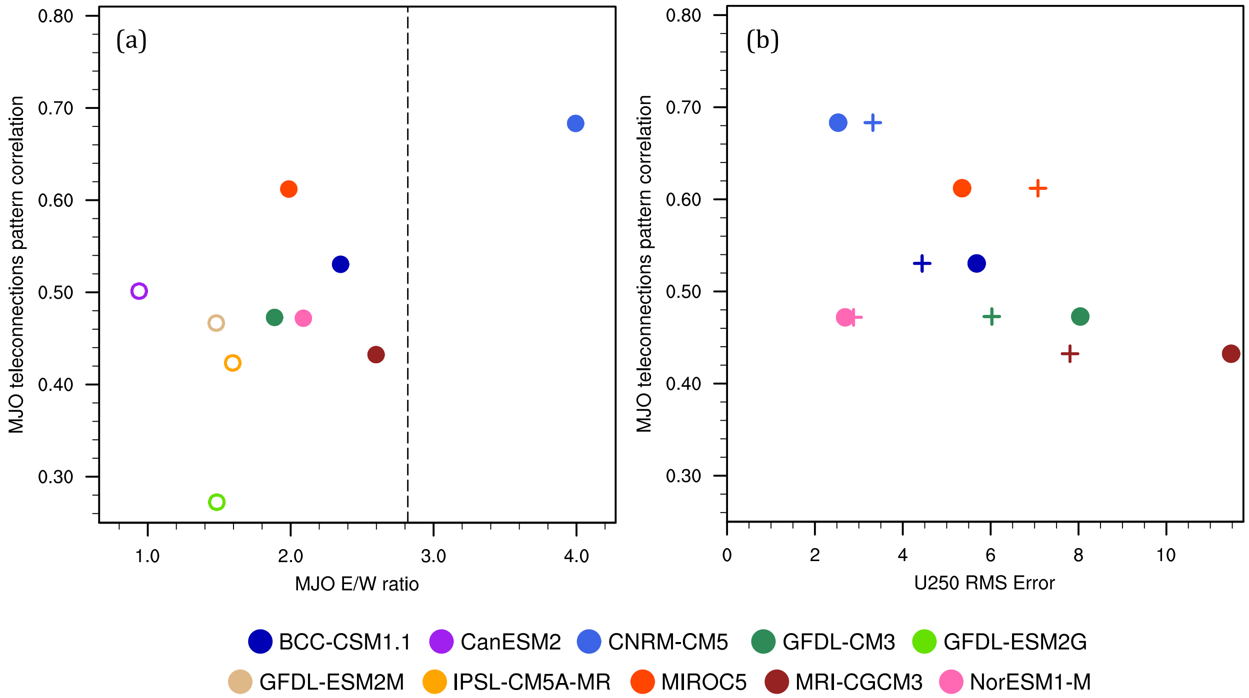

FIG. 4.6. Teleconnection pattern correlation averaged for all MJO phases (y-axes) relative to the (a) MJO E/W ratio and (b) the 250-hPa mean zonal wind RMS error. In panel (a), the dashed line indicates the observed E/W ratio, and the open circles represent the poor MJO models. In panel (b), the plus signs show the model zonal wind RMS error over the full Pacific basin, while the filled circles indicate the longitudinal RMS error in the region of the subtropical jet. See text for more detailed explanations.

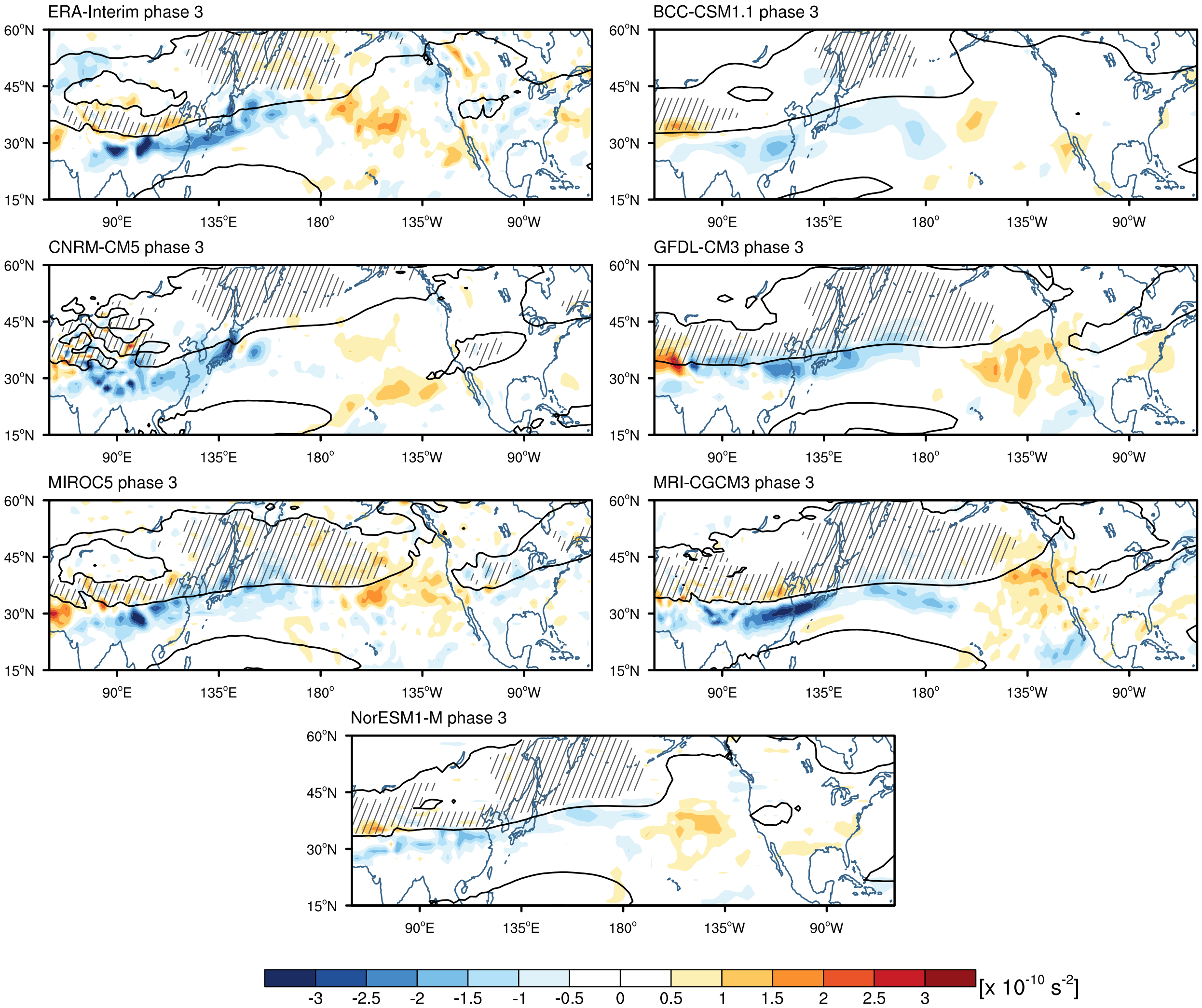

FIG. 4.7. Pentad anomalous Rossby wave source (RWS; color shading) composited relative to MJO phase 3 for reanalysis (top left) and the good MJO models. For reference, the $K_s = 3$ contour line from Figure 4.3 is overlaid, and the $\beta_M < 0$ regions north of 25°N are hatched.

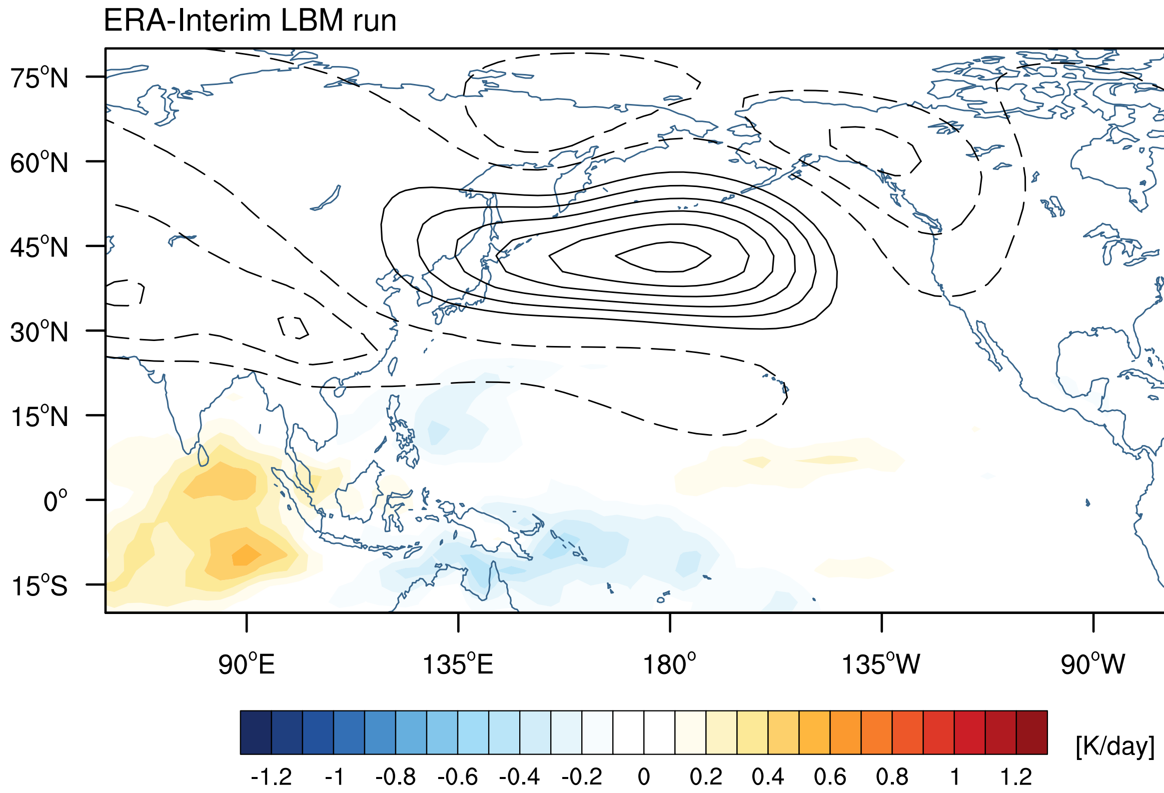

FIG. 4.8. Anomalous 250-hPa geopotential height response (contours) to the reanalysis Q_1' against the reanalysis basic state. Shown is the average 8 – 18 day response to a propagating heat source initiated during MJO phase 1 and coinciding with MJO phases 2 – 3. See text for further details regarding the propagating heat source used. Contours are every 5 m and the zero contour is omitted. The color shading shows the 1000-hPa to 200-hPa 8 – 18 day averaged reanalysis Q_1'.

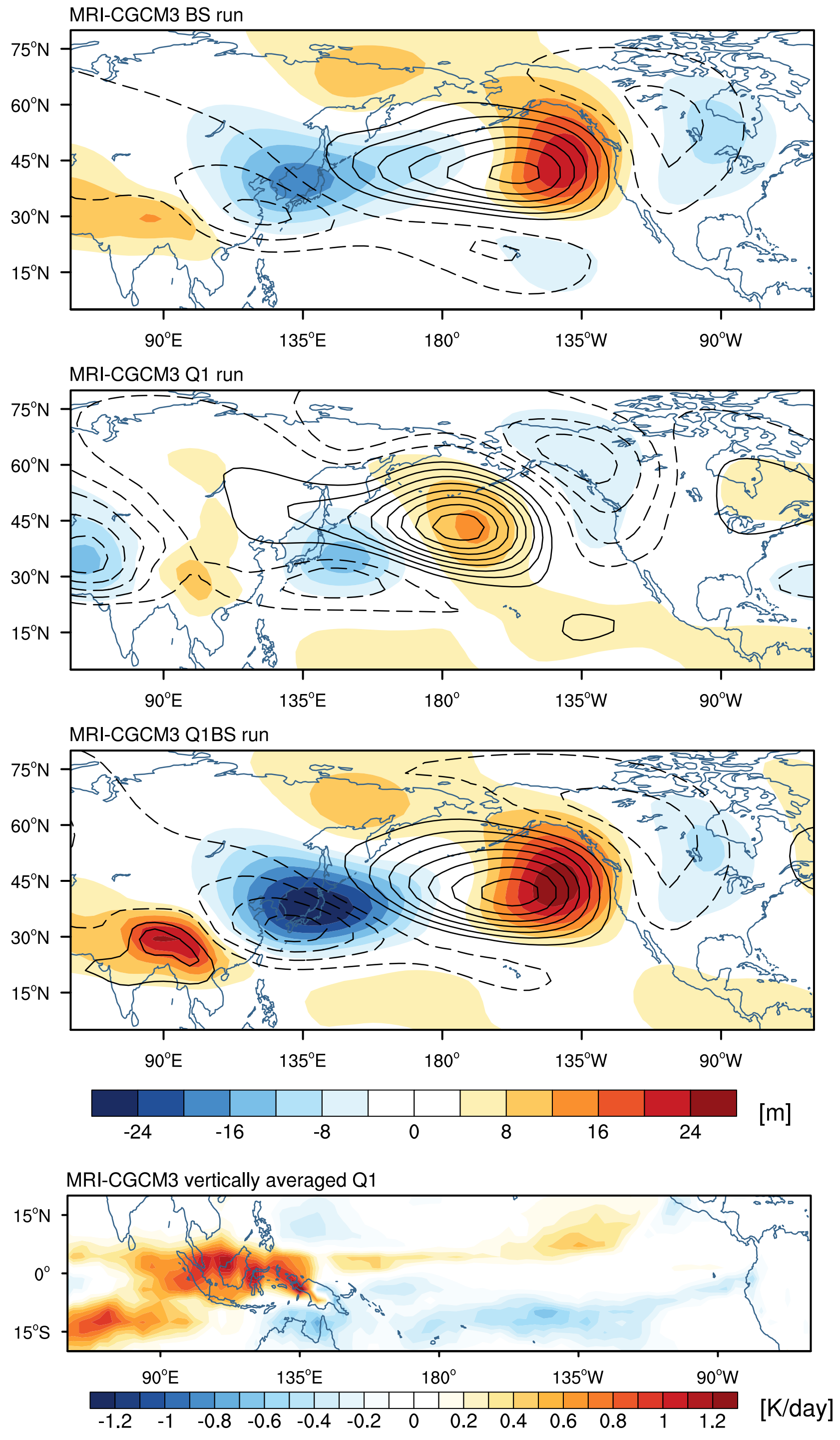
MRI-CGCM3 BS run

MRI-CGCM3 Q1 run

MRI-CGCM3 Q1BS run

MRI-CGCM3 vertically averaged Q1

FIG. 4.9. Anomalous 250-hPa geopotential height 8 – 18 day average LBM response (contours) to reanalysis Q_1' against the MRI-CGCM3 basic state (first panel; referred to as the MRI-CGCM3 BS run), MRI-CGCM3 Q_1' against the reanalysis basic state (second panel; MRI-CGCM3 Q1 run), and MRI-CGCM3 Q_1' against the MRI-CGCM3 basic state (third panel; MRI-CGCM3 Q1BS run). Contours are every 5 m and the zero contour is omitted. Color shading is the difference between each MRI-CGCM3 LBM run and the reference run shown in Figure 4.8. The bottom panel shows the 8 – 18 day average MRI-CGCM3 Q_1'.

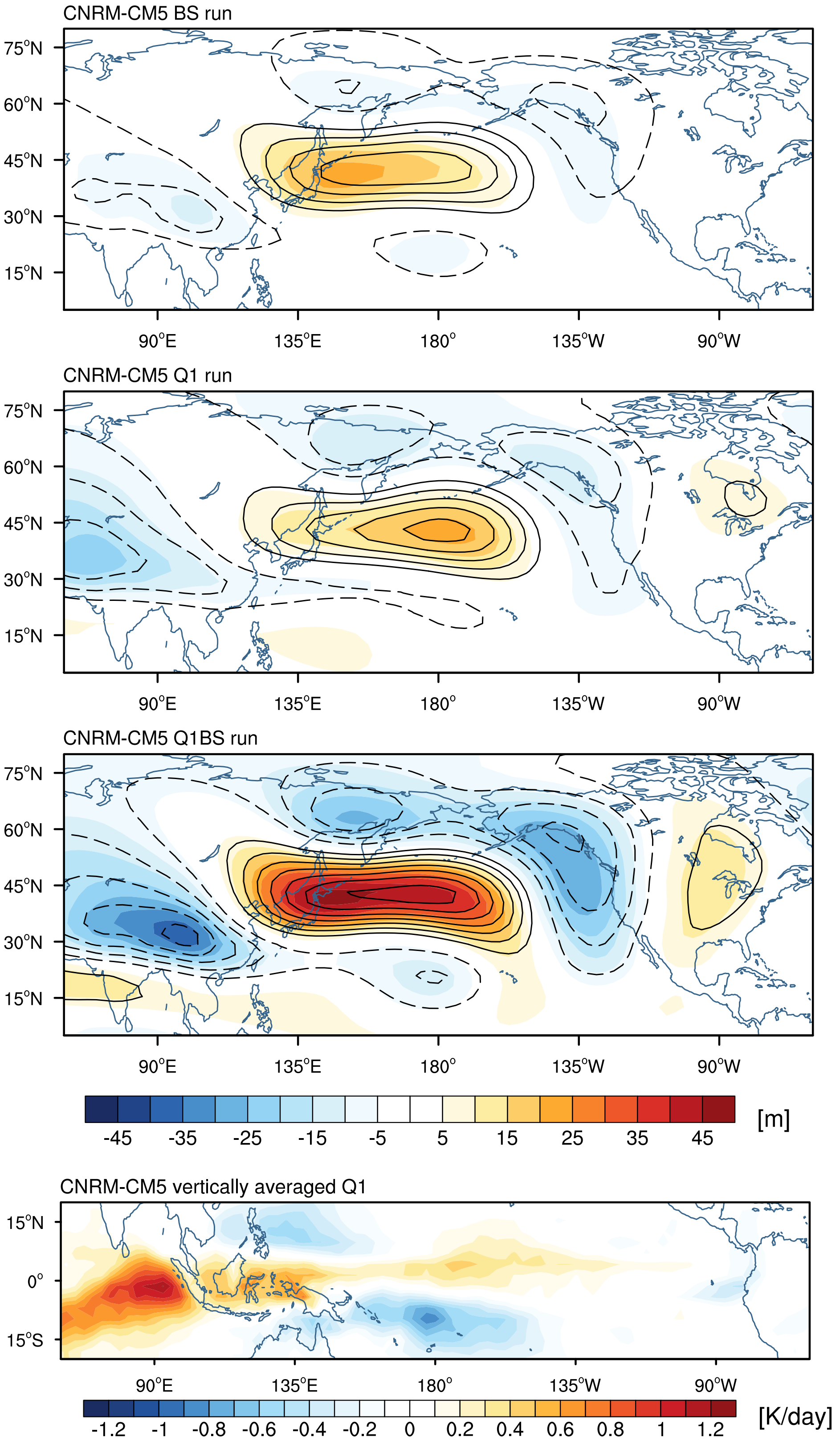

FIG. 4.10. Same as Figure 4.9, but for CNRM-CM5. Due to a stronger LBM response, the geopotential height anomaly contour interval is increased to 10 m.

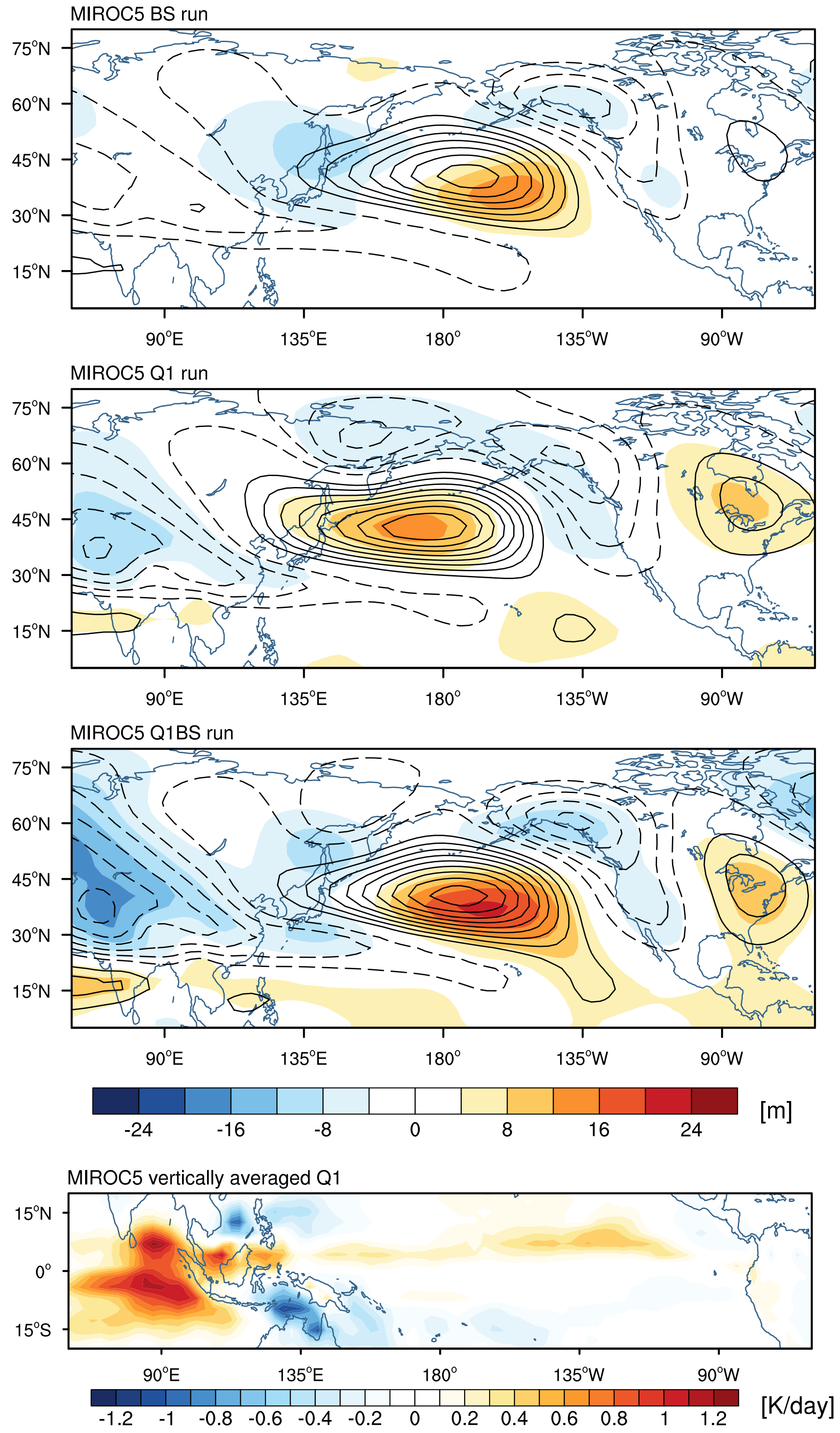
MIROC5 BS run

MIROC5 Q1 run

MIROC5 Q1BS run

MIROC5 vertically averaged Q1

FIG. 4.11. Same as Figure 4.9, but for MIROC5.

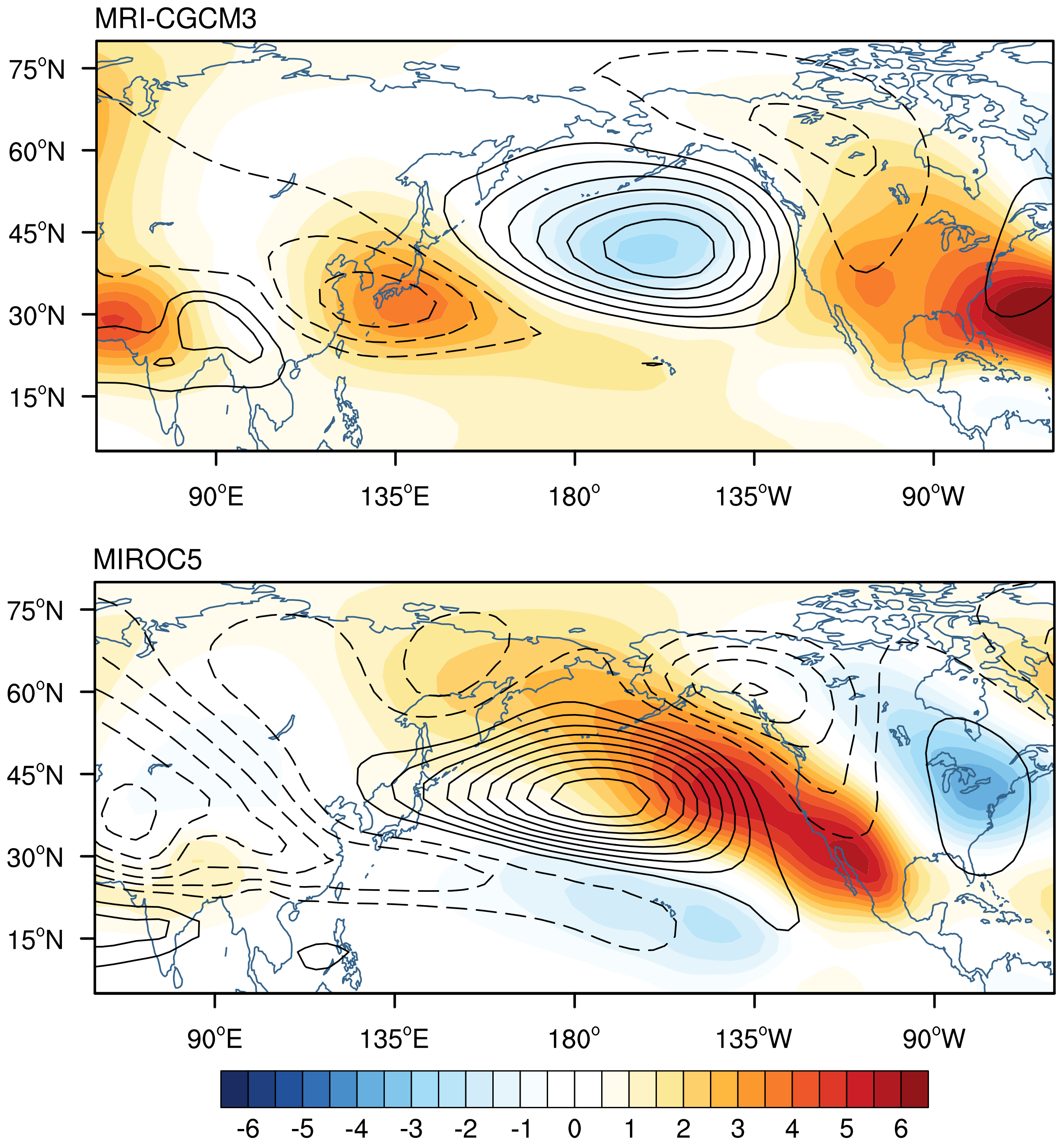

FIG. 4.12. Anomalous 250-hPa geopotential height 8 – 18 day average LBM response (contours) to a modified MRI-CGCM3 Q_1' against the MRI-CGCM3 basic state (top panel) and a modified MIROC5 Q_1' against the MIROC5 basic state (bottom panel). LBM runs are modified by setting Q_1' to zero east of 170°W. Contours are every 5 m and the zero contour is omitted. Color shading is the difference between each corresponding GCM Q1BS run and the modified Q_1' run.

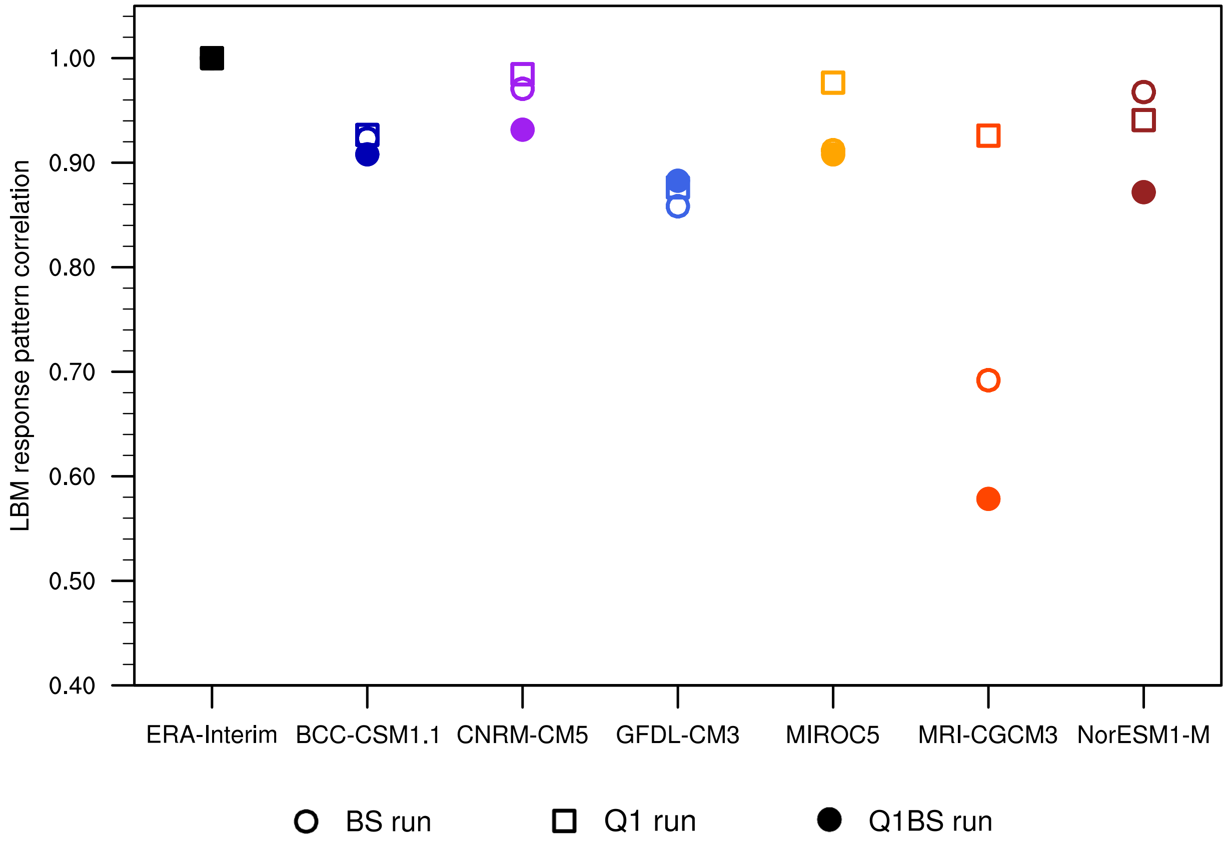

FIG. 4.13. Teleconnection pattern correlation between the LBM reference reanalysis run and each GCM LBM experiment for the 8 – 18 day average response initialized by MJO phase 1 heating. The averages approximately correspond to MJO phases 2 – 3. Correlation coefficients are provided for the BS runs (open circles), the Q1 runs (open squares) and the Q1BS runs (filled circles).

CHAPTER 5: CONCLUSIONS

5.1 Summary

This dissertation expands the current understanding of how MJO teleconnections influence Northern Hemisphere winter blocking. Furthermore, the study provides further insight into how MJO teleconnections are altered during ENSO events and how the MJO influences blocking during ENSO conditions. These findings are beneficial for the mid-range forecasting of atmospheric blocking, as well as other extratropical phenomena influenced by the MJO during ENSO events. Given the importance of the basic state and MJO heating for MJO-induced Rossby wave teleconnections, this study also furthers the understanding of how GCM basic state and MJO heating biases lead to errors in MJO teleconnections. Understanding the impact of these biases is useful to climate scientists and modelers that use GCMs who are interested in phenomena that are significantly influenced by the MJO.

In Chapter 2, a two-dimensional blocking index is employed to examine the influence of the MJO on Northern Hemisphere winter blocking in the Pacific, Atlantic, and European regions. The main findings of Chapter 2 include:

1) The MJO significantly influences Pacific blocking during all MJO phases, particularly in the high-latitudes where the meridional gradient of geopotential height is relatively weak.
2) MJO phase 3 is followed by a significant decrease in East Pacific and Atlantic blocking. Following MJO phase 7, characterized by the opposite-signed

heating as phase 3, the East Pacific and Atlantic regions observe a near doubling in blocking frequency relative to the corresponding winter mean.

3) MJO phase 4 is followed by a significant suppression of European blocking, whereas a significant increase in European blocking follows MJO phase 6. This blocking increase is hypothesized to be a result of a) a pre-existing anomalous anticyclone in the Atlantic, and b) a preceding negative PNA pattern that is triggered and influenced by the MJO.

Chapter 3 expands on the results of Chapter 2 by examining the MJO influence on winter blocking during ENSO events. Chapter 3 first examines changes to the MJO teleconnection patterns due to the ENSO-altered basic states and ENSO-induced changes in MJO convection. The study then examines how the altered MJO teleconnection patterns influence high-latitude blocking in the Pacific and Atlantic regions. The key findings of Chapter 3 are summarized below:

1) MJO Rossby wave Pacific anomalies tend to be shifted or extend further eastward during El Niño relative to La Niña. This is likely due to the eastward extension of the subtropical jet during El Niño.
2) The impact of MJO Rossby waves on high-latitude blocking depends on ENSO phase. During El Niño, significant changes in Pacific high-latitude blocking occur mostly in the latter half of the MJO cycle (MJO phases 6 – 8). During La Niña, the MJO significant influence on Pacific blocking is primarily during the first half of the MJO cycle (MJO phases 1 – 5).
3) The MJO phase 3 and El Niño Pacific teleconnection patterns act destructively, with an insignificant influence on Pacific high-latitude blocking.

Conversely, the La Niña Pacific teleconnection pattern acts constructively with the MJO phase 3 pattern, and Pacific high-latitude blocking is significantly suppressed.

4) The MJO phase 7 and El Niño Pacific teleconnection patterns act constructively. During El Niño, MJO phase 7 is followed by a persistent and significant increase in blocking throughout the North Pacific. In contrast, the MJO phase 7 and La Niña Pacific teleconnection patterns result in a pattern that is not favorable for Pacific blocking.

5) During La Niña, a significant decrease in Atlantic blocking follows MJO phase 3. During El Niño, MJO phase 7 is followed by a significant and persistent increase in Atlantic blocking, with a blocking frequency approximately tripled relative to the climatological winter mean. Results with an NLBM suggest that MJO Rossby waves provide the initial dipole anomaly over the Atlantic that is associated with the blocking increase. **E**-vector analysis suggests that the anomalous blocking pattern may be able to persist due to transient eddy activity.

6) A significant increase in Atlantic blocking does not follow MJO phase 7 during neutral ENSO years, and is not as robust during cold ENSO years as during warm ENSO years. This suggests that the MJO phase 7 significant doubling in Atlantic frequency observed in Chapter 2 is likely due to the near-tripling observed during El Niño years.

Chapter 3 demonstrates that changes to the MJO teleconnection patterns can alter the influence of MJO convection on extratropical weather and climate, such as atmospheric blocking. While Chapter 3 focuses on the natural variability of MJO teleconnections due to ENSO changes in the basic state and MJO heating, Chapter 4 examines how errors in the basic state and MJO influence MJO teleconnections in GCMs. Model errors in MJO teleconnection patterns may in turn introduce biases to extratropical weather and climate that is influenced by the MJO, such as blocking. Chapter 4 utilizes data from 10 CMIP5 GCMs and employs a LBM to determine the independent influence of the GCM basic state and GCM MJO on MJO Pacific teleconnection biases. The primary findings of Chapter 4 are summarized below:

1) GCMs with a relatively good MJO can have equally poor skill at simulating the MJO teleconnection patterns as GCMs with a poor MJO due to the model basic state in good MJO models. This suggests that both the MJO and the basic state must be properly simulated in order to accurately capture MJO teleconnection patterns.
2) Significant MJO teleconnection biases were observed in GCMs with an eastward-extended Pacific subtropical jet. The MJO teleconnection patterns of these GCMs were shifted east relative to reanalysis due to the model basic state.
3) Errors in the horizontal structure of Indo-Pacific MJO convection in GCMSs were found to have lesser impacts on the MJO teleconnection patterns relative to basic state errors. This is in agreement with previous studies that demonstrate that the Rossby wave source (RWS) in the Pacific subtropical jet is relatively insensitive to the location of Indo-Pacific tropical heating.

4) Errors in MJO convection east of the Dateline appear to have an influence on the simulated MJO teleconnection patterns, including changes to teleconnection amplitude and pathway.

5.2 Caveats

An important caveat to this study is that various ways exist to define blocking. In Chapters 2 and 3 we define blocking based on a 2D index that specifically looks for a reversal in 500-hPa geopotential height. However, different answers are possible if a different methodology is used. An example discussed in Chapter 2 is the blocking index used in Moore et al. (2010), which allows blocks to propagate. As a result, Moore et al. (2010) demonstrates an increase in Pacific blocking during some MJO phases where we observe a decrease. Another example is provided by Cassou (2008), also discussed in Chapter 2, which defined each day as part of a Euro-Atlantic regime that includes European blocking. This methodology results in higher amplitude changes in blocking relative to MJO phase than the index employed here. Some studies also employ different criteria to define a blocking event, such as requiring that only 4 days be consecutively blocked (e.g. Pelly and Hoskins 2003) whereas we use a 5 day requirement, or requiring a consecutive 12° (e.g. Tibaldi and Molteni 1990) or 20° (e.g. Dong et. al. 2008) longitude to be blocked compared to our 15° longitude. In addition, there are a variety of blocking indices that use other fields, such as PV or zonal wind. The issue of the wide variety of blocking indices is addressed in Barnes et al. (2012), who demonstrated that similar results are obtainable when using different field gradients if the same methodology is followed. A different methodology such as changing the criteria that defines a blocking event may provide different results than those described in this dissertation.

In Chapter 3, a limitation to the results is the relatively smaller number of samples available for each MJO phase during an ENSO event. While sample size is addressed in significance testing as well as the use of an NLBM, the amplitude of the composite responses relative the MJO and ENSO phase, particularly for MJO phase 3 during cold ENSO events, may change as more data becomes available in the future. The impact of a limited sample size on the relative amplitude of MJO composites during ENSO phases is addressed in Roundy et al. (2010).

The use of the NLBM in Chapter 3 presents its own caveats. As discussed in the chapter, the NLBM is sensitive to the initial MJO phase of the propagating heat source. It is unclear how much of this sensitivity is physical (e.g. Figure 3.15) or a shortcoming of the NLBM. In addition, the propagating heat source employed in the NLBM (Chapter 3) as well as the LBM (Chapter 4) includes approximations that are idealized. It is assumed that each MJO phase last 6 days and maintains strong amplitude throughout its cycle. In reality, the duration of each MJO phase varies. Furthermore, MJO events tend to be more episodic in nature, decaying during its cycle or becoming stronger at a later point in its cycle. The episodic nature of MJO events is taken into account to some extent by forcing the NLBM with heating beginning at specific MJO phases based on Figure 3.15. However, the propagating heat source approximations may introduce discrepancies between the MJO phase composites and the LBM/NLBM responses.

The limited number of CMIP5 GCMs available at the time of the Chapter 4 investigations is also a caveat to this dissertation. This study does not examine basic state and MJO biases that are not prominent in the GCMs used here. Additional GCMs may reveal biases not discussed here that may be important for MJO teleconnections. Furthermore, the limited number of GCMs presents a constraint to the skill metrics employed in Chapter 4. It is possible that the relationships between MJO teleconnection skill and MJO or zonal wind skill metrics could change if more GCMs are examined.

5.3 Future Work

The work presented in this dissertation suggests many avenues for future work. The work presented here focuses on the influence of the MJO on the extratropics; however, MJO impacts on the extratropical atmosphere may in turn influence the MJO and future MJO teleconnections (e.g. Lin et al. 2009). Atmospheric blocking alters the flow and can persist beyond the lifetime of an MJO phase or MJO event; it is therefore possible that the presence of a persistent block can impact the pathways of MJO teleconnections and future MJO events.

Based on the results of Chapter 2, more work is needed to understand how MJO heating impacts European blocking. It is unclear why the negative PNA pattern develops during some MJO events and not in others, and what the role is of the PNA pattern on European blocking. Furthermore, it is unclear if both the PNA pattern and the pre-existing Atlantic anticyclone are necessary for the significant increase in European blocking that follows MJO phase 6.

In addition, unresolved questions exist based on the work in Chapter 3. The results presented suggest that the NAO patterns associated with the MJO (e.g. Lin et al. 2009; Cassou 2008) may depend on ENSO phase. This is in agreement with Roundy (2010), who noticed that the MJO had a stronger relationship with the NAO during cold ENSO conditions. More work is needed to understand why the MJO-NAO relationship appears stronger during cold ENSO than warm ENSO. This may aid in the understanding of the MJO phase 3 Atlantic blocking signal, which appears weaker during warm ENSO than cold ENSO. Furthermore, in Chapter 3 the influence of the MJO on blocking was limited to high-latitude blocking. Further work is needed to understand the influence of the MJO on mid-latitude blocking during ENSO events (e.g. East Pacific and European blocking), which was not investigated here due to sample size limitations. The sample size available of a given MJO phase for each ENSO phase also complicates comparisons between warm and cold ENSO MJO composites. One possibility is to examine the Chapter 3 relationships using long-term coupled GCM simulations.

Future work based on Chapter 4 includes examining additional GCMs from the CMIP5 and the upcoming CMIP6 archives as well as other types of models, such as weather forecasting models. This may provide further insight into possible MJO teleconnection biases not discussed in Chapter 4, as well as further the understanding between MJO teleconnection skill and the MJO/basic state skill metrics discussed. Furthermore, additional work is needed to understand how MJO teleconnection biases impact extratropical weather and climate on longer timescales. Understanding the impact on long-term biases would be useful to climate scientists and modelers interested in extratropical variability.

REFERENCES

Adler, R., and Coauthors, 2003: The version 2 Global Precipitation Climatology Project (GPCP) Monthly Precipitation Analysis (1979–present). *J. Hydrometeor.*, **4**, 1147–1167.

Ahn, M.-S. and Coauthors, 2017: MJO simulation in CMIP5 climate models: MJO skill metrics and process-oriented diagnostics. *Clim. Dyn.*, submitted.

Alaka, G. J., and E. D. Maloney, 2012: The Influence of the MJO on Upstream Precursors to African Easterly Waves. *J. Climate*, **25**, 3219–3236.

Bao, M., and D. L. Hartmann, 2014: The response to MJO-like forcing in a nonlinear shallow-water model. *Geophys. Res. Lett.*, **41**, doi:10.1002/ 2013GL057683.

Barnes, E. A., J. Slingo, and T. Woollings, 2012: A methodology for the comparison of blocking climatologies across indices, models and climate scenarios. *Climate Dyn.*, **38**, 2467–2481.

Bell, C. J., L. J. Gray, A. J. Charlton-Perez, M. M. Joshi, and A. A. Scaife, 2009: Stratospheric communication of El Niño teleconnections to European winter. *J. Clim.*, **22**, 4083-4096.

Benedict, J. J., S. Lee, and S. B. Feldstein, 2004: Synoptic view of the North Atlantic Oscillation. *J. Atmos. Sci.*, **61**, 121–144.

Berggren R., B. Bolin, and C. G. Rossby, 1949: An aerological study of zonal motion, its perturbations and break-down. *Tellus*, **2**, 14-37.

Buehler, T., C. C. Raible, and T. F. Stocker, 2011: The relationship of winter season North Atlantic blocking frequencies to extreme cold or dry spells in the ERA_40. *Tellus*, **63A**, 212-222.

Cassou, C., 2008: Intraseasonal interaction between the Madden–Julian Oscillation and the North Atlantic Oscillation. *Nature*, **455**, 523-527.

Croci-Maspoli, M., C. Schwierz, and H. C. Davies, 2007: A multifaceted climatology of atmospheric blocking and its recent linear trend. *Clim. Dyn.*, **20**, 633–649.

Davini, P., C. Cagnazzo, R. Neale, and J. Tribbia, 2012: Coupling between Greenland blocking and the North Atlantic Oscillation pattern. *Geophys. Res. Lett.*, **39**, L14701.

Dawson A., Matthew A.J., and D. P. Stevens, 2011: Rossby wave dynamics of the North Pacific extra-tropical response to El Niño: importance of the basic state in coupled GCMs. *Clim. Dyn.*, **37**, 391–405.

Dee, D. P. and Coauthors, 2011: The ERA-Interim reanalysis: configuration and performance of the data assimilation system. *Q. J. R. Meteorol. Soc.*, **137**, 553-597.

Dole, R., and Coauthors, 211: Was there a basis for anticipating the 2010 Russian heat wave? *Geophys. Res. Lett.*, **38**, L06702, doi:10.1029/2010GL046582.

Donald, A., H. Meinke, B. Power, A. de H. N. Maia, M. C. Wheeler, N. White, R. C. Stone, and J. Ribbe, 2006: Near-global impact of the Madden-Julian Oscillation on rainfall, *Geophys. Res. Lett.*, **33**, L09704, doi:10.1029/2005GL025155.

Dong L., Vogelsang T.J., Colucci S.J., 2008: Interdecadal trend and ENSO-related interannual variability in Southern Hemisphere blocking, *J. Climate*, **21**, 3068 – 3077.

Feldstein, S. B., 2003: The dynamics of NAO teleconnection pattern growth and decay. *Q.J.R. Meteorol. Soc.*, **129**, 901–924.

Franzke, C., S. Lee, and S. B. Feldstein, 2004: Is the North Atlantic Oscillation a breaking wave? *J. Atmos. Sci.*, **61**, 145– 160.

Franzke, C., S. B. Feldstein, and S. Lee, 2011: Synoptic analysis of the Pacific-North American teleconnection pattern. *Q.J.R. Meteorol. Soc.*, **137**, 329 – 346.

Garfinkel, C. I., S. B. Feldstein, D. W. Waugh, C. Yoo, and S. Lee, 2012: Observed connection between stratospheric sudden warmings and the Madden-Julian Oscillation. *Geophys. Res. Lett.*, **39**, L18807.

Garfinkel, C. I, J. J. Benedict, and E. D. Maloney, 2014: Impact of the MJO on the boreal winter extratropical circulation. *Geophys. Res. Lett.*, **41**, 6055-6062.

Gill, A. E., 1980: Some simple solutions for heat-induced tropical circulation, *Q. J. R. Meteorol. Soc.*, **106**, 447–462.

Green, J. S. A., 1977: The weather during July 1976: Some dynamical considerations of the drought. *Weather*, **32**, 120–126.

Hamill T. M., and G. N. Kiladis, 2014: Skill of the MJO and Northern Hemisphere blocking in GEFS and medium-range reforecasts. *Mon. Wea. Rev.*, **142**, 868-885.

Henderson, S. A., E. D. Maloney, and E. A. Barnes, 2016: The Influence of the Madden-Julian Oscillation on Northern Hemisphere Winter Blocking. *J. Climate*, **29**, 4597–4616.

Henderson, S. A., E. D. Maloney, S. –W. Son, 2017: Madden-Julian Oscillation Pacific teleconnections: The impact of the basic state and MJO representation in General Circulation Models, *J. Climate*, in press.

Hendon, H. H., C. Zhang, and J. D. Glick, 1999: Interannual variation of the Madden-Julian oscillation during austral summer. *J. Climate*, **12**, 2538-2550.

Hendon, H. H., B. Liebmann, M. Newman, J. D. Glick, and J. E. Schemm, 2000: Medium-range forecast errors associated with active episodes of the Madden–Julian oscillation. *Mon. Weather Rev.*, **128**, 69–86.

Higgins, R. W., and K. C. Mo, 1997: Persistent North Pacific circulation anomalies and the tropical intraseasonal oscillation. *J. Climate*, **10**, 223-244.

Hinton, T. J., B. J. Hoskins, and G. M. Martin, 2009: The influence of tropical sea-surface temperatures on North Pacific atmospheric blocking. *Clim. Dyn.*, **33**, 549-563.

Hoell, A., M. Barlow, M. C. Wheeler, and C. Funk, 2014: Disruptions of El Niño–Southern Oscillation teleconnections by the Madden–Julian oscillation. *Geophys. Res. Lett.*, **41**, 998–1004.

Hoskins, B. J., and D. J. Karoly, 1981: The steady linear response of a spherical atmosphere to thermal and orographic forcing. *J. Atmos. Sci.*, **38**, 1179–1196.

Hoskins, B. J. and P. D. Sardeshmukh, 1987: A diagnostic study of the dynamics of the Northern Hemisphere winter of 1985-86. *Q.J.R. Meteorol. Soc.*, **113**, 759–778.

Hoskins, B. J., and T. Ambrizzi, 1993: Rossby Wave Propagation on a Realistic Longitudinally Varying Flow. *J. Atmos. Sci.*, **50**, 1661–1671.

Hsu, H.-H., 1996: Global view of the intraseasonal oscillation during northern winter. *J. Climate*, **9**, 2386–2406.

Hung, M.-P., J.-L. Lin, W. Wang, D. Kim, T. Shinoda, and S. J. Weaver, 2013: MJO and convectively coupled equatorial waves simulated by CMIP5 climate models. *J. Climate*, **26**, 6185–6214.

Ineson, S. and A. A. Scaife, 2009: The role of the stratosphere in the European climate response to El Niño. *Nat. Geosci.*, **2**, 32-36.

Jones, C., D. E. Waliser, K. M. Lau, and W. Stern, 2004: Global occurrences of extreme precipitation events and the Madden-Julian Oscillation: Observations and predictability, *J. Climate*, **17**, 4575–4589.

Jiang, X., and Coauthors, 2015: Vertical structure and physical processes of the Madden-Julian oscillation: Exploring key model physics in climate simulations, *J. Geophys. Res. Atmos.*, **120**, 4718–4748.

Jin, F., and B. J. Hoskins, 1995: The Direct Response to Tropical Heating in a Baroclinic Atmosphere. *J. Atmos. Sci.*, **52**, 307–319.

Jones, C., D. E. Waliser, K. M. Lau, and W. Stern, 2004: Global occurrences of extreme precipitation events and the Madden–Julian oscillation: Observations and predictability. *J. Climate*, **17**, 4575–4589.

Karoly, D. 1983: Rossby wave propagation in a barotropic atmosphere. *Dyn. Atmos. Oceans*, **7**, 111-125.

Kessler, W. S., 2001: EOF Representations of the Madden–Julian Oscillation and Its Connection with ENSO. *J. Climate*, **14**, 3055–3061.

Kiladis, G. N., and K. M. Weickmann, 1992: Circulation anomalies associated with tropical convection during northern winter. *Mon. Weather Rev.*, **120**, 1900-1923.

Kim, D., and Coauthors, 2009: Application of MJO simulation diagnostics to climate models. *J. Climate*, **22**, 6413–6436.

Kim, D., A. H. Sobel, E. D. Maloney, D. M. W. Frierson, and I.-S. Kang, 2011: A systematic relationship between intraseasonal variability and mean state bias in AGCM simulations. *J. Climate*, **24**, 5506–5520.

Kim, D., and Coauthors, 2014: Process-Oriented MJO Simulation Diagnostic: Moisture Sensitivity of Simulated Convection. *J. Climate*, **27**, 5379–5395.

Kosaka, Y., J. S. Chowdary, S. Xie, Y. Min, and J. Y. Lee, 2012: Limitations of seasonal predictability for summer climate over East Asia and the northwestern Pacific. *J. Climate*, **25**, 7574–7589.

Lau, W. K.-M., and D. E. Waliser, 2012: Intraseasonal Variability in the Atmosphere-Ocean Climate System, 2nd ed., 613 pp., Springer, Heidelberg, Germany.

Lee, H. -T. and NOAA CDR Program (2011): NOAA Climate Data Record (CDR) of Daily Outgoing Longwave Radiation (OLR), Version 1.2. 1979-2010. NOAA National Climatic Data Center. doi:10.7289/V5SJ1HH2. Accessed April 8, 2015.

Liebmann, B., H. H. Hendon, and J. D. Glick, 1994: The relationship between tropical cyclones of the western Pacific and Indian Oceans and the Madden-Julian oscillation, *J. Meteorol. Soc. Jpn.*, **72**, 401–412.

Lin H., G. Brunet, and J. Derome, 2009: An Observed Connection between the North Atlantic Oscillation and the Madden–Julian Oscillation. *J. Climate*, **22**, 364–380.

Lin, H., G. Brunet, and R. Mo, 2010: Impact of the Madden-Julian Oscillation on wintertime precipitation in Canada. *Mon. Wea. Rev.*, **138**, 3822-3839.

Lorenz, D. J., and D. L. Hartmann, 2006: The effect of the MJO on the North American monsoon, *J. Clim.*, **19**, 333–343.

Madden, R. A., and P. Julian, 1971: Detection of a 40-50 day oscillation in the zonal wind in the Tropical Pacific. *J. Atmos. Sci.*, **28**, 702-708.

Madden, R. A., and P. Julian, 1972: Description of a global-scale circulation cells in the tropics with a 40-50 day period. *J. Atmos. Sci.*, **29**, 1109-1123.

Maloney, E. D., and D. L. Hartmann, 2000: Modulation of eastern North Pacific hurricanes by the Madden-Julian oscillation, *J. Clim.*, **13**, 1451–1460.

Maloney, E. D., and S.-P. Xie, 2013: Sensitivity of tropical intraseasonal variability to the pattern of climate warming. *J. Adv. Model. Earth Syst.*, **5**, 32–47.

Marchand, R., N. Beagley, S. E. Thompson, T. P. Ackerman, and D. M. Schultz, 2006: A Bootstrap Technique for Testing the Relationship between Local-Scale Radar Observations of Cloud Occurrence and Large-Scale Atmospheric Fields. *J. Atmos. Sci.*, **63**, 2813–2830.

Marshall, A. G., D. Hudson, H. H. Hendon, M. J. Pook, O. Alves, and M. C. Wheeler, 2014: Simulation and prediction of blocking in the Australian region and its influence on intra-seasonal rainfall in POAMA-2. *Clim. Dyn.*, **42**, 3271-3288.

Masato, G., B. J. Hoskins, and T. J. Woollings, 2012: Wave-breaking characteristics of mid-latitude blocking. *Quart. J. Roy. Meteor. Soc.*, **138**, 1285-1296.

Masato, G., B. J. Hoskins, and T. J. Woollings, 2013a: Winter and Summer Northern Hemisphere Blocking in CMIP5 Models. *J. Climate*, **26**, 7044–7059.

Masato, G., B. J. Hoskins, and T. J. Woollings, 2013b: Wave-breaking characteristics of Northern Hemisphere winter blocking: A two-dimensional approach. *J. Clim.*, **26**, 4535-4549.

Matthews, A. J., B. J. Hoskins, and M. Masutani, 2004: The global response to tropical heating in the Madden-Julian oscillation during the northern winter. *Q. J. R. Meteorol. Soc.*, **130**, 1991-2011.

Mo, K., and R. W. Higgins, 1998: Tropical convection and precipitation regimes in the western United States, *J. Climate*, **10**, 3028–3046.

Moon, J. Y., B. Wang, and K. J. Ha, 2011: ENSO regulation of MJO teleconnection. *Climate Dyn.*, **37**,1133–1149.

Moore, R. W., O. Martius, and T. Spengler, 2010: The modulation of the subtropical and extratropical atmosphere in the Pacific Basin in response to the Madden Julian Oscillation. *Mon. Wea. Rev.*, **138**, 2761-2779.

Mori, M. and M. Watanabe, 2008: The growth and triggering mechanisms of the PNA: A MJO-PNA coherence. *J. Meteor. Soc. Japan*, **86**, 213-236.

Nakamura T, Hara M, Oshika M, Tachibana Y, 2015: Impact of the winter North Atlantic Oscillation (NAO) on the Western Pacific (WP) pattern in the following winter through Arctic sea ice and ENSO. Part II: multi-model evaluation of the NAO–ENSO linkage. *Clim. Dyn.*, **45**, 3547–3562.

Pelly, J. L., and B. J. Hoskins, 2003: A new perspective on blocking. *J. Atmos. Sci.*, **60**, 743-755.

Pohl, B., and A. J. Matthews, 2007: Observed Changes in the Lifetime and Amplitude of the Madden–Julian Oscillation Associated with Interannual ENSO Sea Surface Temperature Anomalies. *J. Climate*, **20**, 2659–2674.

Pook, M. J., J. S. Risbey, P. C. McIntosh, C. C. Ummenhofer, A. G. Marshall, and G. A. Meyers, 2013: The Seasonal Cycle of Blocking and Associated Physical Mechanisms in the Australian Region and Relationship with Rainfall. *Mon. Wea. Rev.*, **141**, 4534–4553.

Rashid, H.A., Hendon, H.H., and M. C. Wheeler, 2011: Prediction of the Madden-Julian oscillation with the POAMA dynamical prediction system. *Clim Dyn*, **36**, 649.

Rasmusson, E. M., and J. M. Wallace, 1983: Meteorological aspects of the El Niño/Southern Oscillation. *Science*, **222**, 1195–1202.

Riddle, E. E., M. B. Stoner, N. C. Johnson, M. L. L'Heureux, D. C. Collins, and S. B. Feldstein, 2013: The impact of the MJO on clusters of wintertime circulation anomalies over the North American region. *Climate Dyn.*, **40**, 1749–1766.

Roundy, P., K. MacRitchie, J. Asuma, and T. Melino, 2010: Modulation of the global atmospheric circulation by combined activity in the Madden–Julian oscillation and the El Niño–Southern Oscillation during boreal winter, *J. Climate*, **23**, 4045–4059.

Roundy, P., 2011: Tropical–extratropical interactions. Intraseasonal Variability in the Atmosphere-Ocean Climate System, 2nd ed. W. K.-M. Lau and D. E. Waliser, Eds., Springer, 497–512.

Salby, M. L., and H. H. Hendon, 1994: Intraseasonal behavior of clouds, temperature and motion in the tropics. *J. Atmos. Sci.*, **51**, 2207-2224.

Sardeshmukh, P. D., and B. J. Hoskins, 1988: The generation of global rotational flow by steady idealized tropical divergence. *J. Atmos. Sci.*, **45**, 1228–1251.

Seo, K.-H., and S.-W. Son, 2012: The Global Atmospheric Circulation Response to Tropical Diabatic Heating Associated with the Madden–Julian Oscillation during Northern Winter. *J. Atmos. Sci.*, **69**, 79–96.

Seo, K.-H., H.-J. Lee, and D. M. W. Frierson, 2016: Unraveling the teleconnection mechanisms that induce wintertime temperature anomalies over the Northern Hemisphere continents in response to the MJO. *J. Atmos. Sci.*, **73**, 3557-3571.

Shabbar, A., J. Huang, and K. Higuchi, 2001: The relationship between the wintertime North Atlantic Oscillation and blocking episodes in the North Atlantic. *Int. J. Clim.*, **21**, 355–369.

Slade, S. A., and E. D. Maloney, 2013: An Intraseasonal Prediction Model of Atlantic and East Pacific Tropical Cyclone Genesis. *Mon. Wea. Rev.*, **141**, 1925–1942.

Takaya, K., and H. Nakamura, 2001: A formulation of a phase-independent wave-activity flux for stationary and migratory quasigostrophic eddies on a zonally varying basic flow, *J. Atmos. Sci.*, **58**, 608-627.

Taylor, K.E., R.J. Stouffer, G.A. Meehl, 2012: An overview of CMIP5 and the experiment design. *Bull. Am. Meteorol. Soc.*, **93**, 485–498.

Tibaldi, S., and F. Molteni, 1990: On the operational predictability of blocking. *Tellus*, **42A**, 343-365.

Ting, M., and P. D. Sardeshmukh, 1993: Factors determining the extratropical response to equatorial diabatic heating anomalies, *J. Atmos. Sci.*, **50**, 907-918.

Trenberth, K. E., 1986: An assessment of the impact of transient eddies on the zonal mean flow during a blocking episode using localized Eliassen–Palm flux diagnostics. *J. Atmos. Sci.*, **43**, 2070–2087.

Trenberth, K. E., G. W. Branstator, D. Karoly, A. Kumar, N.-C. Lau, and C. Ropelewski, 1998: Progress during TOGA in understanding and modeling global teleconnections associated with tropical sea surface temperatures. *J. Geophys. Res.*, **103**, 14291–14324.

Tyrrell, G. C., Karoly, D. J., and J. L. McBride, 1996: Links between tropical convection and variations of the extratropical circulation during TOGA-CORE. *J. Atmos. Sci.*, **53**, 2735–2748.

Vautard, R., 1990: Multiple weather regimes over the North Atlantic: Analysis of precursors and successors. *Mon. Wea. Rev.*, 118, 2056-2081.

Vecchi, G. A., and N. A. Bond, 2004: The Madden–Julian oscillation (MJO) and northern high latitude wintertime surface air temperatures. *Geophys. Res. Lett.*, **31**, L04104, doi:10.1029/2003GL018645.

Waliser, D., and Coauthors, 2009: MJO simulation diagnostics, *J. Clim.*, **22**, 3006–3030.

Wallace, J. M., and D. S. Gutzler, 1981: Teleconnections in the geopotential height field during the Northern Hemisphere winter. *Mon. Wea. Rev.*, **109**, 784–812.

Watanabe, M. and Kimoto, M., 2000: Atmosphere-ocean thermal coupling in the North Atlantic: A positive feedback. *Q.J.R. Meteorol. Soc.*, **126**, 3343–3369.

Weare, B. C., 2013: El Niño teleconnections in CMIP5 models. *Clim. Dyn.*, **41**, 2165-2177.

Wheeler, M. C., and H. H. Hendon, 2004: An all-season real-time multivariate MJO index: Development of an index for monitoring and prediction. *Mon. Wea. Rev.*, **132**, 1917-1932.

Wilks, D. S., 2011: Statistical Methods in the Atmospheric Sciences. Elsevier, 676 pp.

Wolding, B. O., E. D. Maloney, and M. Branson, 2016: Vertically Resolved Weak Temperature Gradient Analysis of the Madden-Julian Oscillation in SP-CESM. *J. Adv. Modeling. Earth. Sys.*, **8**, doi:10.1002/2016MS000724.

Woollings, T., B. Hoskins, M. Blackburn, and P. Berrisford: 2008: A new Rossby wave-breaking interpretation of the North Atlantic Oscillation. *J. Atmos. Sci.*, **65**, 609-626.

Yanai, M., S. Esbensen, and J.-H. Chu, 1973: Determination of bulk properties of tropical cloud clusters from large-scale heat and moisture budgets. J. Atmos. Sci., 30, 611–627.

Yasui, S., and M. Watanabe, 2010: Forcing processes of the summertime circumglobal teleconnection pattern in a dry AGCM. *J. Climate*, **23**, 2093–2114.

Yoo, C., S. Park, D. Kim, J.-H. Yoon, and H.-M. Kim, 2015: Boreal Winter MJO Teleconnection in the Community Atmosphere Model Version 5 with the Unified Convection Parameterization. *J. Climate,* **28**, 8135–8150.

Zhang, C., 2005: Madden-Julian Oscillation. *Rev. Geophys.*, **43**, RG2003, doi:10.1029/2004RG000158.

Zhang, C., M. Dong, S. Gualdi, H. H. Hendon, E. D. Maloney, A. Marshall, K. R. Sperber, and W. Wang, 2006: Simulations of the Madden-Julian Oscillation by Four Pairs of Coupled and Uncoupled Global Models. *Climate Dyn.*, **27**, 573-592.